

**BUILDING SUBSURFACE VELOCITY MODELS USING  
OCEAN-BOTTOM SEISMIC DATA:  
GREEN CANYON, GULF OF MEXICO.**

---

A Thesis

Presented to

the Faculty of the Department of Earth and Atmospheric Sciences

University of Houston

---

In Partial Fulfillment of the  
Requirements for the Degree  
Master of Science

---

By

Ken Obiora Uduanochie

December 2011

**BUILDING SUBSURFACE VELOCITY MODELS USING  
OCEAN-BOTTOM SEISMIC DATA:  
GREEN CANYON, GULF OF MEXICO.**

---

Ken Obiora Uduanochie

APPROVED:

---

Dr. Robert R. Stewart, Chairman

---

Dr. Li Aibing

---

Dr. Edip Baysal  
Paradigm 77024

---

Dean, College of Natural Sciences and Mathematics

## **Acknowledgements**

I would like to express my gratitude to the many people that I have worked with and who in the last couple of years have helped to make this thesis possible. The greatest acknowledgement goes to my supervisor, Robert Stewart. Edip Baysal, and Aibing Lee, also encouraged and guided me through all my work at the University of Houston and greatly enhanced the results presented as part of this thesis.

I give special thanks to Marie Dawn, Gary Martins, Helen Delome, Paul Farmer, Genmeng Chen, and Cathy Weber from Ion GX Technology for their assistance. I also thank Carlos Calderon and Eric Nessler, also from Ion GX Technology, for processing and ProMAX help during the time of my study. I would like to thank Bode Omoboya and Pap Segome, who were always available to help out. I also express my gratitude to Ion GX Technology for providing me with the seismic data used in this thesis, providing some of the software used in this study and for financial support during my studies. For the assistance I got during my study, I would like to thank all of the students, staff, and especially professors for their academic instruction at the University of Houston.

Finally, I thank Cynthia, my wife, Kamsy my son and Zara, my lovely daughter, for their sacrifice of time and love.

**BUILDING SUBSURFACE VELOCITY MODELS USING  
OCEAN-BOTTOM SEISMIC DATA:  
GREEN CANYON, GULF OF MEXICO.**

---

An Abstract of a Thesis  
Presented to  
the Faculty of the Department of Earth and Atmospheric Sciences  
University of Houston

---

In Partial Fulfillment of the  
Requirements for the Degree  
Master of Science

---

By  
Ken Obiora Uduanochie  
December 2011

## Abstract

Creating better seismic images below the relatively shallow salt bodies in the deep-water Green Canyon area of the Gulf of Mexico is the goal of this work. I designed two techniques to determine seismic velocity models using 4C-3D ocean-bottom seismic data from that region.

This work builds velocity models ( $V_p$  and  $V_s$ ) that are geologically reasonable, using ray-tracing and anisotropic velocity model-building techniques. The ray-tracing technique is based on correlating near sea floor images from the pure P-wave (PP) and converted-wave (PS) sections and interpreting depth-equivalent horizons. Along these horizons, 1.5 D ray tracing is performed to estimate the travel times at selected locations, which are inverted manually to estimate the  $V_p$  and  $V_s$  velocities (using only the near traces). The estimated velocities are interpolated across the selected horizons to produce the  $V_p$  and  $V_s$  models. The workflow in this technique is less effective on farther offset data at those selected locations. Results from analysis using the technique described above show estimated shallow  $V_p$  and  $V_s$  are in the range of 1560m/s and 147m/s ( $V_p/V_s$  values of 10) in the shallow areas and ( $V_p/V_s$  values of 4) above the salt body.

The second technique proposed uses an anisotropic velocity model building technique to estimate the effective velocity ratio ( $\gamma_{\text{eff}}$ ) from the intermediate offsets ( $x/z < 1.5$ ) and the anisotropy coefficient ( $\chi_{\text{eff}}$ ) from the far offsets ( $x/z < 2.0$ ). These additional parameters are used to estimate stacking velocities to create common image point gathers from pre-stack time migrations, which are then used in residual move-out analysis to build a robust  $V_p$  and  $V_s$  velocity models through an iterative process.

## **Dedication**

**To My Parents**

**In Memoriam**

## Table of Content

|  |            |
|--|------------|
| <b>Approval page</b> .....   | <b>ii</b>  |
| <b>Acknowledgement</b> .....   | <b>iii</b> |
| <b>Abstract</b> .....  | <b>v</b>   |
| <b>Dedication</b> .....  | <b>vi</b>  |
| <b>Table of Content</b> .....  | <b>vii</b> |
| <b>List of Tables</b> .....  | <b>x</b>   |
| <b>List of Figures</b> .....   | <b>xi</b>  |
| <b>List of Nomenclature, Symbols and Abbreviations</b> .....           | <b>xvi</b> |
| <b>Chapter 1: Introduction to PP and PS Wave</b> .....                 | <b>1</b>   |
| 1.1 The history of seismic data analysis .....                         | 1          |
| 1.2 Reasons for economic viability of PS-wave seismic acquisition..... | 2          |
| 1.3 Fundamentals of PP and PS wave.....                                | 5          |
| 1.4 Seismic data acquisition overview .....                            | 7          |
| 1.5 Geophones.....   | 11         |
| 1.6 Hardware and software .....  | 12         |
| <b>Chapter 2: Area of Study</b> .....                                  | <b>13</b>  |
| 2.1 Location .....   | 13         |
| 2.2 Geologic setting .....   | 14         |
| 2.2.1 Green Canyon, Gulf of Mexico .....                               | 14         |
| 2.3 Seismic data .....   | 18         |
| 2.3.1 Acquisition.....   | 18         |
| 2.3.2 Preprocessing .....  | 19         |
| 2.3.3 Load SEG-Y data.....   | 20         |
| 2.3.4 Data preparation.....  | 21         |
| 2.3.5 The De-bubble filter .....                                       | 22         |
| 2.3.6 Amplitude recovery correction and noise attenuation.....         | 24         |
| 2.3.7 Data windowing .....   | 27         |
| 2.3.8 Design and application of vector fidelity operators .....        | 30         |
| 2.3.9 Rotation of the horizontal components .....                      | 30         |
| 2.3.10 2D SRME – radial and transverse components .....                | 33         |

|   |           |
|---|-----------|
| <b>Chapter 3: The Ray-tracing Technique .....</b>   | <b>38</b> |
| 3.1 Introduction.....   | 38        |
| 3.2 The uses of ray-tracing technique.....  | 39        |
| 3.2.1 Trace generation.....   | 39        |
| 3.2.2 Modeling.....   | 40        |
| 3.2.3 Acquisition planning.....   | 40        |
| 3.2.4 Geophysical challenges.....   | 41        |
| 3.3 Ray-tracing technique workflow.....   | 41        |
| 3.3.1 The reduced water-bottom receiver-line stack.....                                       | 45        |
| 3.3.2 The shallow sea floor registration.....   | 46        |
| 3.3.2 Estimating interval $V_P$ and $V_S$ from dynamic corrections .....                      | 48        |
| 3.4 Assumptions in the ray-based technique.....   | 51        |
| 3.5 Limitations and challenges in using the ray-tracing technique.....                        | 53        |
| 3.6 Results from the ray-tracing technique .....  | 54        |
| 3.7 Synthetic model generation.....   | 56        |
| <b>Chapter 4: The Anisotropic Velocity Model Building Technique.....</b>                      | <b>64</b> |
| 4.1 Introduction.....   | 64        |
| 4.2 The anisotropic velocities and travel times.....  | 64        |
| 4.3 Vertical transverse anisotropy.....   | 67        |
| 4.4 Asymptotic Conversion Point (ACP).....  | 68        |
| 4.4.1 Single layer .....  | 68        |
| 4.4.2 Multiple layers .....   | 71        |
| 4.5 The PSTM velocity model theory.....   | 72        |
| 4.6 Processing flow .....   | 74        |
| 4.6.1 PP and PS stacks .....  | 75        |
| 4.6.2 Estimating the vertical velocity ratio ( $\gamma_0$ ) .....                             | 75        |
| 4.6.3 Estimating the PP-wave normal moveout ( $V_{P2}$ ) at the near offset.....              | 76        |
| 4.6.4 Estimating the PS-wave normal moveout ( $V_{C2}$ ) at the near offset.....              | 77        |
| 4.6.5 Estimating the PS-wave normal moveout ( $\gamma_{\text{eff}}$ ) at the mid offset ..... | 77        |
| 4.6.6 Estimating the PS-wave normal moveout ( $\chi_{\text{eff}}$ ) at the far offset .....   | 78        |
| <b>Chapter 5: Discussion and Conclusion .....</b>   | <b>88</b> |
| 5.1 Discussion .....  | 88        |
| 5.2 Conclusions.....  | 92        |
| <b>References .....</b>   | <b>94</b> |

|                         |            |
|-------------------------|------------|
| <b>Appendix A .....</b> | <b>103</b> |
| <b>Appendix B .....</b> | <b>104</b> |
| <b>Appendix C .....</b> | <b>105</b> |

## List of tables

|   |    |
|---|----|
| Table 1: Thomsen (1986) parameters of the five-layer model for evaluating the accuracy of equation 4.15 ..... | 98 |
| Table 2: The Vs estimated values from Gamma0, PP stacking velocity, PS stacking velocity and ray tracing..... | 98 |

## List of figures

- Figure 1.1: PP and PS sections from the Gulf of Mexico (Chernikoff et al., 2007), An example from the gas chimney in the Cantarell oilfields in the Gulf of Mexico, described by Stewart et al (2008) show a washed-out area (circled) on the P-wave section corresponding to events at the top of the Cretaceous that are more definitive on the PS section. .... 4
- Figure 1.2: (a) The Alba field PP amplitudes map with the reservoir and its surrounding shales having similar acoustic impedances to PP-waves and the reservoir not showing up clearly. (b) The Alba field PS-wave with reservoir showing high acoustic impedance to PS-waves, so the reflection-amplitude map shows a sand-rich channel (green and yellow). This is according to the oilfield review of summer 2004 by Schlumberger. .... 4
- Figure 1.3: Snell's Law;  $\sin \theta_1/v_1 = \sin \theta_2/v_2$ ..... 5
- Figure 1.4: The schematic of the factors that affect the seismic wave energy as it propagates through the earth layers. .... 6
- Figure 1.5: The schematic above shows the seismic recording vessel, the shooting vessel and the deployed receiver-line in the PS survey. Some of the energy from the down-going P-wave is converted upon reflection to S-wave and recorded by receivers at the seabed. These receivers are sensitive to different components of motion..... 10
- Figure 1.6: (a) The VectorSeisOcean(VSO) sensor system, showing (MEMS) accelerometer chips. (b) The four receiver components schematic showing one hydrophone and three orthogonally oriented geophones sensitive to different components of motion. .... 12
- Figure 2.1: The location map of the seismic data used in the study. (a) The map of the United States of America and the red dot is the location of the Green canyon in the Gulf of Mexico. (b)The enlargement shows grid location of the survey. (c)The layout of the source and receivers, the acquisition area is situated over GC blocks 468, 469, 512, and others at an angle of 34 degrees. (d)The fold map, two swaths were acquired and one of them was used for this work. .... 14
- Figure 2.2: The diagram shows the carbonate play buried under the Sigsbee salt sheet and the escarpment on the right that forms the cliff unto the abyssal plain of the Gulf (Anderson et al., 2009)..... 16
- Figure 2.3: The section shows the structure in the foldbelts in the Gulf of Mexico overlain by the Sigsbee salt sheet (Anderson et al., 2009). .... 17

|   |    |
|---|----|
| Figure 2.4: A schematic showing receivers (blue crosses) and sources (green dots) spacing. ....   | 18 |
| Figure 2.5: The entire preprocessing flow showing (a) The PP preprocessing arm of the flow and; (b) The PS preprocessing arm of the flow. ....  | 19 |
| Figure 2.6: The schematic describes resampling process .....  | 20 |
| Figure 2.7: The source signature in display, showing the times at which the wavelet starts (first trough) and right before the bubble starts. ....  | 23 |
| Figure 2.8: Trace with the ringing noise compared to the de-bubbled trace .....   | 23 |
| Figure 2.9: (a) PS stack dataset with the ringing noise before applying the de-bubble filter.(b) PS stack dataset with the ringing noise after applying the de-bubble filter .....  | 23 |
| Figure 2.10: (a) Seismic dataset stack before noise attenuation. (b) Seismic dataset stack after noise attenuation .....  | 26 |
| Figure 2.11: The Frequency spectra from a shot gather from the PP seismic data.....   | 28 |
| Figure 2.12: The Frequency spectra from a shot gather from the PS seismic data.....   | 29 |
| Figure 2.13: The schematic diagram shows the rotation of the horizontal components...   | 31 |
| Figure 2.14: (a) The radial component gathers before rotation. (b) The tranverse component before rotation. (c) The radial component after rotation showing stronger signal strength. (d) The tranverse component after rotation of energy in the tranverse direction showing lesser signal strength .....  | 32 |
| Figure 2.15: (a) Receiver gather for radial data before de-multiple (b) 2D SRME multiple prediction on radial gathers (c) Receiver data after multiple subtraction (d) Multiple prediction adaptively matched .....   | 37 |
| Figure 3.1: Ray tracing through the Horizons from the PP and PS reduced waterbottom receiver stacks created from the Earthwave software. The PP section is above and the PS section is below, created to show the coverage area for shots going into a common receiver PP gather is more than the coverage area for shots going into the PS common receiver gather..... | 39 |
| Figure 3.2: The processing flow for the ray-based technique.....  | 42 |
| Figure 3.3: Common receiver gathers with imported horizons in the dynamic moveout analysis software from the EGL. The emphasis is to find the velocities that flatten the   |    |

near traces on each horizon shown above assuming there is no hyperbolicity in the farther offsets due to the reduced water bottom. The first horizon is the yellow line shown on the gathers and next two horizons are the black ones. Three horizons were used in this study. (a) Shows the PP common receiver gather with the inserted horizons. When each horizon is selected, the appropriate velocity that flattens the events on the horizon is selected. (b) Shows the PS common receiver gather with the inserted horizons that are equivalent to the events on the PP common receiver gather, likewise there is an equivalent velocity that flattens the events on each selected horizon. (c) Shows the various velocities selected for each horizon in the both the PP and the PS data with green line representing the PP velocities and the slower blue line representing the PS velocities..... 43

Figure 3.4: Common receiver limited offset stack, (200-400m). (a) The PP stack section. (b) The PS stack section. These stacks were created using Promax software and a constant water velocity. .... 44

Figure 3.5: Then use water bottom reduced time for near-traces from receiver gathers to account for the differences in source and receiver depths. .... 45

Figure 3.6: Velocity estimates of 1500m/s to 1600/s with increments of 10m/s were applied to flatten the gather. (a) is 1550m/s and (b) 1560m/s (middle panel) which best flattens the gathers was selected. (c) is flattened with 1570m/s ..... 47

Figure 3.7: The reflection 2-way time on the PP gather and PS gather section is gotten from the section above. The two-way time estimates have been used to calculate  $V_s$  value from  $V_p$  gotten from dynamic correction from the section in the Figure3.2. 750ms used in the calculation above is the travel-time of the PS wave, calculated from the difference between the PS reflection time (820ms) shown by the yellow line of the middle panel and the travel-time of the down-going P-wave leg of the travel-time ( $0.5 \times 140$ ms) of the first panel..... 48

Figure 3.8: Dynamic velocity analysis was carried out one horizon at a time. The software allows velocity values to be overlain on the gather display and the yellow line is the interval velocity that flattens the first horizon. This analysis is carried out horizon by horizon as shown above. The velocity at the horizon highlighted in yellow is too fast for the horizon above it, the reason there is a bulge in the horizon above but too slow for horizons below, the reason for the bulge below the horizon highlighted in yellow. .... 50

Figure 3.9: The receiver line used for the velocity analysis in this study..... 51

Figure 3.10: The common receiver gathers section show the applied interval velocities with the  $V_p/V_s$  values for the 3 horizons..... 55

Figure 3.11: The  $V_p$  and  $V_s$  generated interval velocity models along the 2d receiver line profile..... 56

|  |    |
|--|----|
| Figure 3.12: PS receiver line stack generated using a constant velocity .....  | 57 |
| Figure 3.13: Three selected horizons, including the top of salt .....  | 58 |
| Figure 3.14: Velocities and other material properties assigned to three layers .....   | 58 |
| Figure 3.15: $V_p$ (green) and $V_s$ (blue) estimated for the various layers assuming equivalent horizons in the two modes.....  | 60 |
| Figure 3.16: Generated synthetic shot gather from the estimated traveltimes.....   | 61 |
| Figure 3.17: Synthetic stack with -20Db noise level .....  | 61 |
| Figure 3.18: PP stack generated using 1500m/s constant velocity .....  | 62 |
| Figure 4.1: The single layer representation of the PS-wave arrival time (after Thomsen,1999) .....   | 65 |
| Figure 4.2: A source-receiver offset conversion point for a single trace with $\gamma = 2$ with equation 4.8 in depth equivalent (after Tessmer and Behle 1998). .....   | 70 |
| Figure 4.3: A display of a reflection event from an ACP binned gather (Thomsen 1999) .....   | 72 |
| Figure 4.4: The processing flow for the anisotropic velocity model .....   | 74 |
| Figure 4.5: The semblance display for estimating the vertical velocity ratio ( $\gamma_0$ ) from the PP and PS stack sections.....   | 79 |
| Figure 4.6: The semblance display (left side) for estimating the PS-wave normal moveout ( $V_c$ ) from the near offset of the gather. The right side of display shows the effect on the gather.....  | 80 |
| Figure 4.7: Estimating the PS-wave normal moveout ( $\gamma_{eff}$ ) at the mid offset gathers on the far right side of the display. The far left side of the 2 parameter displays is the semblance for the $V_c$ parameter and in the middle is the semblance for the $\gamma_{eff}$ parameter.....                           | 81 |
| Figure 4.8: The far left side of the 2 parameter displays is the semblance for the $V_c$ parameter and in the middle is the semblance for the $\chi_{eff}$ parameter and the far right side is showing the effects of the parameter estimation of PS-wave normal moveout ( $\chi_{eff}$ ) at the far offset of the gather..... | 82 |

Figure 4.9: PS-wave stack generated after estimating  $V_c$  from the short spread gathers. The top of the salt body is fussy and not well illuminated as there is anisotropy in the layers. .... 83

Figure 4.10: PS-wave stack after the estimation of  $V_c$ ,  $\gamma_0$  and  $\gamma_{eff}$  from the mid-offset gathers, applying the parameters and stacking. .... 84

Figure 4.11: The PS-wave stack after estimating  $V_c$ ,  $\gamma_0$ ,  $\gamma_{eff}$  and  $x_{eff}$  from the far offset and two iterations of PSTM residual velocity update. The shallow salt is illuminated better with the anisotropic velocity applied to the data and stacked. .... 85

Figure 4.12: (a) PS-data stack section. with the top of salt shown (b) The PP-wave stack section with the equivalent top of salt shown. The  $V_p/V_s$  from  $T_{ps}$  and  $T_p$  of the top of salt shown in stacks sections (PP and PS) is estimated to be 3..... 87

Figure 5.1: The graph shows the estimated  $V_s$  from surrounding Well logs (courtesy of Fred Hilterman) using Mudrock line equation(Castagna et al., 1985), compared to  $V_s$  estimated from the 1.5D ray tracing,  $\gamma_0$  and  $V_c$  ..... 91

Figure B1: The calculated  $V_p$  for the Green Canyon area from nearby well logs (courtesy of Fred Hilterman) ..... 104

Figure C1: Seismic trace is a product of convolving reflectivity of the earth with the seismic signature, the source wavelet and noise. .... 105

## List of Nomenclature, Symbols and Abbreviations

| Symbol         | Definition                             |
|----------------|--|
| AVO            | Amplitude versus offset                |
| ACP            | Asymptotic conversion point            |
| DMO            | Dip-moveout                            |
| FIR            | Finite impulse response                |
| $H$            | Top layer thickness                    |
| HTI            | Horizontal transverse isotropy         |
| NMO            | Normal-moveout                         |
| OBC            | Ocean bottom cable                     |
| PP             | Compressional or primary wave (P-to-P) |
| PS             | Mode-converted shear wave (P-to-S)     |
| RMS            | Root-mean-square                       |
| SRME           | Surface related multiple elimination   |
| TI             | Transversely isotropic                 |
| VTI            | Vertical transverse isotropy           |
| $V_p$          | Primary (compressional) wave velocity  |
| $V_s$          | Shear-wave velocity                    |
| $K$            | Incompressibility                      |
| $\mu$          | Rigidity                               |
| $\rho$         | Density                                |
| $V_C$          | PS stacking velocity                   |
| $\gamma_0$     | Vertical velocity ratio ( $V_p/V_s$ )  |
| $\gamma_{eff}$ | Effective velocity ( $V_p/V_s$ ) ratio |
| $\chi_{eff}$   | The anisotropy coefficient             |
| $\eta_{eff}$   | The $P$ -wave anisotropic parameter    |
| $\zeta_{eff}$  | The $S$ -wave anisotropic parameter    |

## **Chapter 1: Introduction to PP and PS Wave**

### **1.1 The history of seismic data analysis**

Since the early years of the 20<sup>th</sup> century, when the basic models of the Earth's deep interior were made from observations of earthquake-generated seismic waves transmitted through the earth (Dziewonski et al., 1981), the use of surface methods (2D and 3D seismic surveys) to explore the subsurface of the earth has evolved rapidly. The ability to acquire and process 2D seismic data was developed in detail in the 1950s and followed by 3D seismic surveys in the 1980s (Liner et al., 1999; and Davies et al., 2004). Since these methods were developed and used for the purpose of exploration seismology, the compressional or PP-wave seismic reflection technique with the down-going pressure wave leg and the up-going pressure wave leg has become accepted by the petroleum industry. And according to Stewart et al., (2003) the use of PP-wave seismic data in exploration seismology will most likely remain a dominant tool for a long time. The physical properties of the rocks in the earth are now effectively and accurately estimated using the PP-wave seismic reflection technique. Also the extent of mineral and natural reservoirs in the earth and the geological structures that contain them can now be predicted, inferred and their position estimated with some accuracy (Hudson, 1992). As a result, there have been benefits for geoscientists, the academic institutions, various industries, and governments of the world.

Many successful companies like CGGVeritas and ION Geophysical, have used the PP-wave seismic reflection technique successfully. The development, design, and

interpretation of seismic surveys using the down-going leg of the pressure wave and the up-going shear leg (PS-wave) has been about 20 years in the making and has become commercially viable in recent years (Stewart et al., 2002).

## **1.2 Reasons for economic viability of PS-wave seismic acquisition**

Depleting conventional oil reservoirs in the world have created a strong demand for unconventional oil reserves. Ivanhoe (1997) stated that we are running out of oil and expressed concern about the global oil consumption and how fewer huge discoveries were being made. But recent advancements in technology have created the more opportunities and production from “unconventional oil”. Converted-wave exploration technology is also advancing.

PS-wave seismic acquisition has become more economically realizable and useful for a number of reasons in recent years. Some of the reasons are:

- PS surveys are contributing to seismic imaging in difficult targets: shale diapirs, beneath gas clouds or gas bearing sediments (Figure 1.1), beneath salt bodies, and in the desert and loose terrain.
- Joint PP and PS seismic data analysis is generating attributes for lithology discrimination and fluid prediction (Figure1.2).
- $V_p/V_s$  values could be generated from investigating anisotropy, using the appropriate techniques and this could improve PS seismic data processing and interpretation.

- PS seismic data are used in building robust velocity models in anisotropic media for improved imaging of reservoir structures, better interpretation, fracture detection, reservoir model building, and reservoir management.
- There is fracture modelling potential with increasing resolution using PS data with a smaller seismic time window imaging and dipping fracture properties to describe larger scale features.
- Anisotropy from rock models are used to interpret temporal changes in the subsurface through time-lapse seismic analysis.
- The use of PS surveys to study the resource potential of gas hydrates and its hazards to drilling activities.
- PS data acquisition is relatively inexpensive compared to SS wave surveys, and effective for obtaining shear information (Stewart et al., 2002)

Despite the dominance of the PP-wave seismic reflection method in exploration seismology, in the areas stated above there are opportunities to generate images that can improve or augment images generated from PP seismic data using PS seismic data.

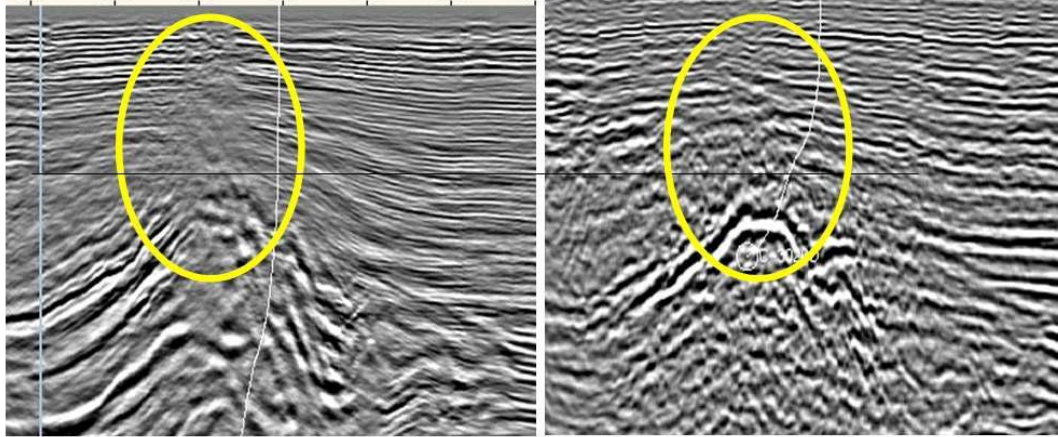


Figure 1.1: PP and PS sections from the Gulf of Mexico (Chernikoff et al., 2007), the gas chimney in the Cantarell oilfields in the Gulf of Mexico show a washed-out area (circled) on the P-wave section corresponding to events at the top of the Cretaceous that are more definitive on the PS section (Stewart, 2008).

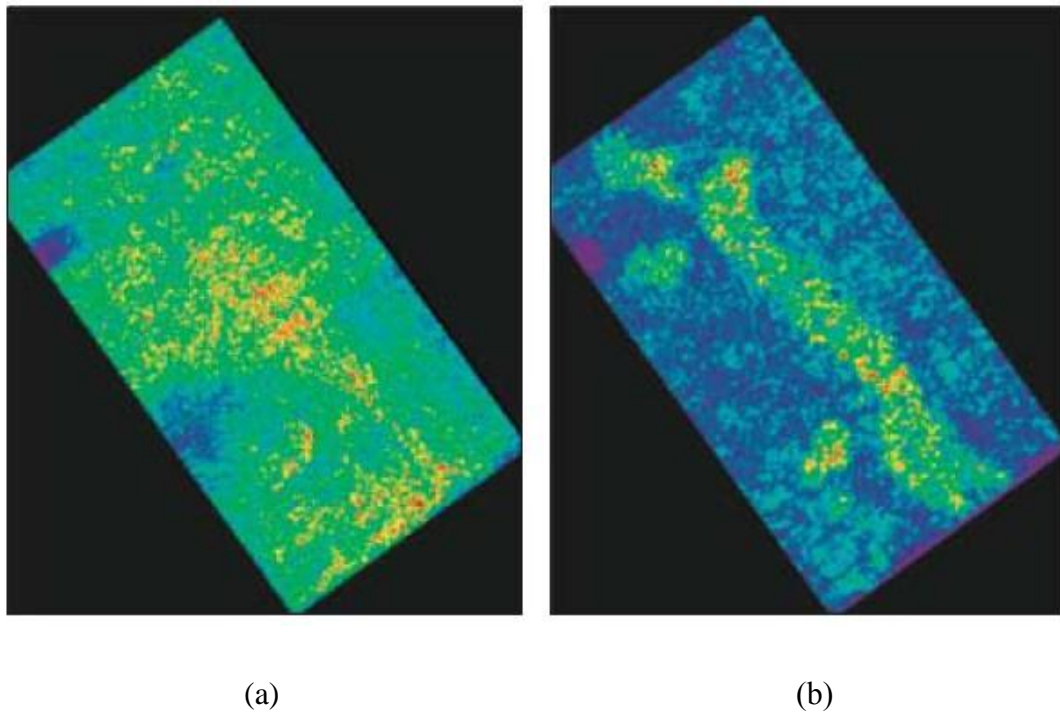
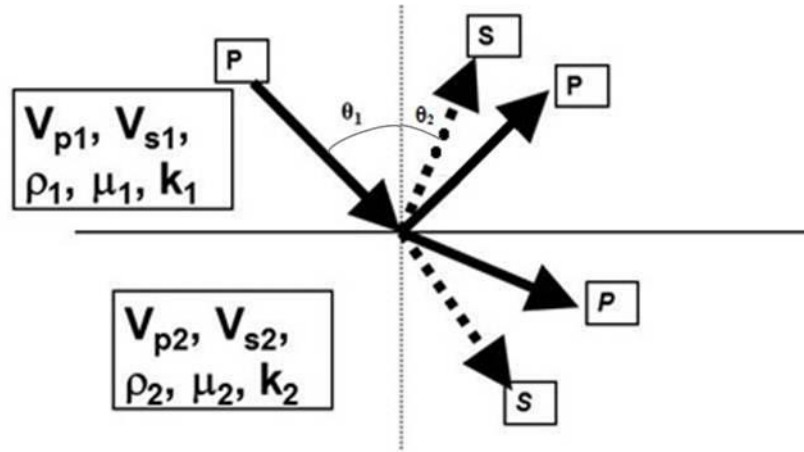


Figure 1.2: (a) The Alba field PP amplitudes map with the reservoir and its surrounding shales having similar acoustic impedances to PP-waves and the reservoir not showing up clearly. (b) The Alba field PS-wave with reservoir showing high acoustic impedance to PS-waves, so the reflection-amplitude map shows a sand-rich channel (green and yellow) according to MacLeod et al., (1999).

### 1.3 Fundamentals of PP and PS wave

As shown in the Figure 1.3, Snell's law as derived from Fermat's principle (the principles of optics), as the travel-time through the media is minimized.



**Figure 1.3: Snell's Law;  $\sin \theta_1/v_1 = \sin \theta_2/v_2$**

Where  $v_1$  and  $v_2$  are the velocities in the two media represented.  $V_p$  and  $V_s$  can be deduced as shown in the equation below:

$$V_p = \sqrt{\frac{K + \frac{4}{3}\mu}{\rho}} \quad \text{and} \quad V_s = \sqrt{\frac{\mu}{\rho}},$$

where  $K$ ,  $\mu$ , and  $\rho$  are incompressibility, rigidity, and density respectively. These parameters are the bedrock for the seismic acquisition criteria for PS wave.  $V_p$  is related to the matrix velocity and the fluid velocity in the pores of the rock material, but  $V_s$  is only related to the matrix velocity of the rock material and is not affected by the fluid velocity. Only part of the PP wave energy is converted to PS wave; some of it transmits

through the various layers, while some of that energy is scattered or absorbed by the earth (Figure 1.4).

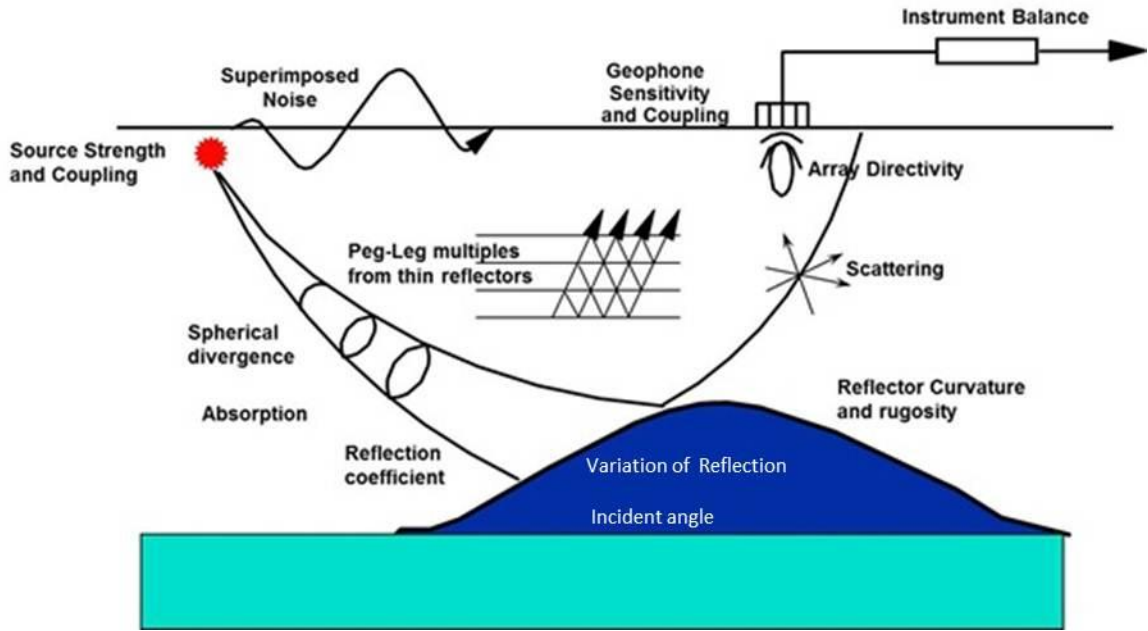


Figure 1.4: The schematic of the factors that affect the seismic wave energy as it propagates through the earth layers.

This study describes an inverse problem scenario where physical properties like the travel times are used to generate a final imaged model; seeks to build anisotropic (VTI) velocity models from the physical properties contained in that earth model using ocean bottom cable seismic data from the Gulf of Mexico. These physical properties are inferred from PP-wave and PS-wave seismic reflections, and then used to produce a final model from all estimates and observations. This study also seeks to constrain the way these properties are estimated to avoid errors in the way the data are collected, analyzed, and interpreted. Lastly, it seeks to build on a solid foundation theoretical expertise in seismic anisotropy for PS-wave velocity analysis using field data and compare the

effectiveness of two moveout analysis methods used to estimate PS-wave parameters in a vertical transverse isotropy (VTI anisotropy) medium as suspected in the seismic data used.

#### **1.4 Seismic data acquisition overview**

It is important to consider the objectives of PS-wave seismic acquisition when planning a survey. The seismic acquisition process searches for vibrational echoes. In this process energy sources and receivers or sensors are placed apart from each other. The energy sources send wave-fronts that propagate to a reflection surface. These wave-fronts are often represented as ray-paths and different types of receivers or sensors record different types of information. The kind of seismic energy sent to the ground can be broken down into “body” waves; P-wave and S-wave. The P-wave is the most common in the industry. P-wave propagates in the direction that the sound travels and S-wave, particle motion is perpendicular to the direction of sound propagation. PS-wave refers to the down going P-wave leg and up going S-wave leg of the event. The source, receiver, recorder and positioning make up the components of seismic acquisition.

A sound source produces acoustic energy that could be impulsive; an example is a dynamite and can be placed a few feet down the earth. A dynamite source burns at 6,000m/s (fast) and has a blasting cap for safety or timing (White, 1999). Another type of energy source is Vibroseis, which has a vibrator with tons of steel with a piston connected by hydraulics to a plate, and can deliver about 62,000 pounds of energy. Others are accelerated weight drop (hammer and anvil) and air-guns; which have a

compressor and work in water. The difference is in the types of signals produced by these energy sources, the politics or logistics of usage in different regions of the world, the geometry of placement of the source-receiver array, and the acquisition planning.

The receiver is a transducer to measure motion (vibration) to record signal from source by converting it into an electric signal; it is made of magnetic material and coiled wire with a sensor. There is a geophone, a type of receiver which could be three components (a vertical component and two horizontal components) used in land surveys and also in ocean bottom acquisition where it is used alongside pressure sensors. Hydrophones are pressure sensors that are used in marine environment and could be used in transition zones. The pressure sensors are pulled behind a seismic vessel in cable arrays for streamer surveys.

This study focuses on the PS survey using the ocean bottom cable (OBC) acquisition, which commences with an initial sonar survey to examine the seafloor to determine the seabed-cable locations for the receiver-lines (Figure 1.5). Then a seismic recording vessel with positioning capability deploys the cable as it moves along the selected receiver-line positions using position information from the seabed cable to ascertain correct positioning. The vessel also attaches a buoy to the end of the receiver line, before proceeding to deploy the second cable. There are two receiver lines used to acquire the data in the study area, which are connected to the vessel for recording seismic data after deployment. There is a different source vessel using an array of air-guns for shooting along predetermined shot lines. This creates a swath of data recorded by the seismic recording vessel for each receiver-line. Then the vessel recovers the receiver-

lines for deploying the next swath. Some of the energy from the down-going incident P-wave ray with angle  $\theta_1$  is believed to have some of it convert to PS-wave with an angle  $\theta_2$  on reflecting. At an offset of  $x$  from the location of the source, the two angles ( $\theta_1$  and  $\theta_2$ ) are represented according to snell's law as shown below:

$$\sin \theta_1/v_1 = \sin \theta_2/v_2 = \delta t/\delta x$$

If the  $x_c$  is the offset to image point depth and  $t_c$  is the PS-wave arrival time, the  $x_c$  would depend to a large extent on  $\gamma$  ( $V_p/V_s$  value) (Tessmer and Behle, 1998), as described in Chapter 4 of this study. The value of  $\gamma$  depends on the vertical homogeneity or isotropy or both. These physical properties are important criteria for PS-wave analysis and are also important when a PS survey is planned. Inhomogeneity and anisotropy has more effect in PS-wave seismic data analysis than in P-wave analysis (Thomsen 1999). Also, he goes ahead to explain that  $\gamma$  being greater than one means the S leg comes up more steeply than the P leg goes down. This criterion is important for PS-wave acquisition because the transversely polarized receiver is better suited for detecting PS-wave than a vertical polarized receiver.

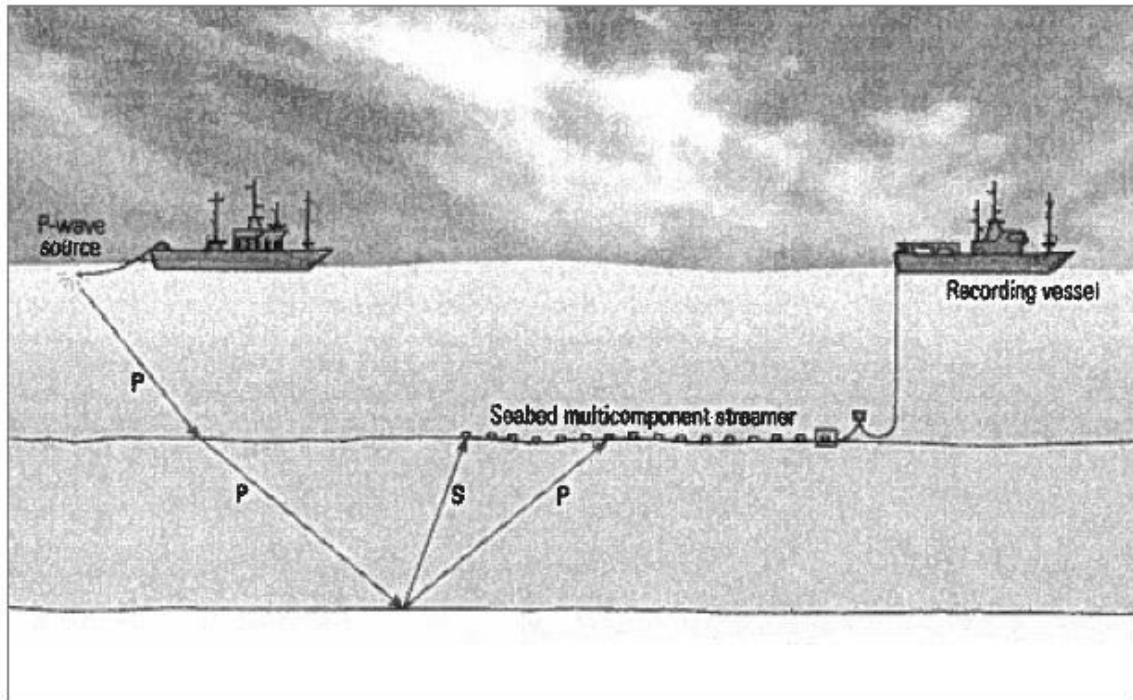
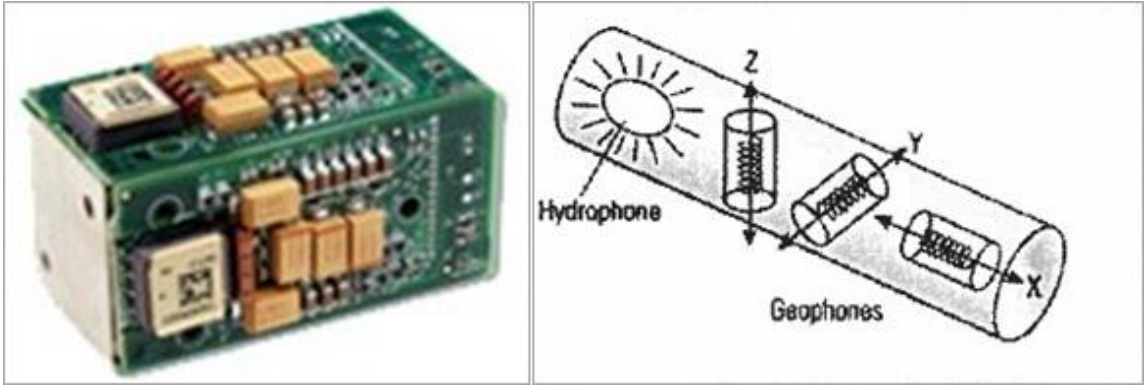


Figure1.5: The schematic above shows the seismic recording vessel, the shooting vessel and the deployed receiver-line in the PS survey. Some of the energy from the down-going P-wave is converted upon reflection to S-wave and recorded by receivers at the seabed. These receivers are sensitive to different components of motion (after Barkved et al., 2004).

Other factors to consider are the depth of the target, its location, its geometry, dip estimates, migration aperture, and the geology of the area when planning for a seismic acquisition survey, as these would determine the type of acquisition survey, the technique and the tools required to achieve the objective of the survey.

## 1.5 Geophones

The quality of seismic data could depend on the geophone used to acquire it. It is important to know the natural frequency, bandwidth, resistivity, sensitivity, and damping of the geophone used (Figure 1.6) because all these have to be specified correctly. The analog geophone has its limitations as it requires a digital converter. A PS survey designed based on an array of geophones and when summed is not so good due to smearing it could generate (Sah, 2008). The single sensor is the new technology which is promoted in the industry at the moment. A confirmation of this statement is given by Podolak (2003) when referring to sharper images that are a result of using the single VectorSeis sensor. The spring and the mass determine the natural frequency of any geophone system. The data used in this study were acquired using the ocean-bottom four-component VectorSeisOcean(VSO) system, a digital single-point sensor that contains three identical and highly sensitive micro-electro-mechanical systems (MEMS) accelerometer chips (Figure1.6). The VestorSeis being single-point sensors is believed to not have the directional bias and signal smear due to geophone grouping into arrays.



(a)

(b)

Figure 1.6: (a) The VectorSeisOcean (VSO) sensor system, showing (MEMS) accelerometer chips. (b) The four receiver components schematic showing one hydrophone and three orthogonally oriented geophones sensitive to different components of motion.

## 1.6 Hardware and software

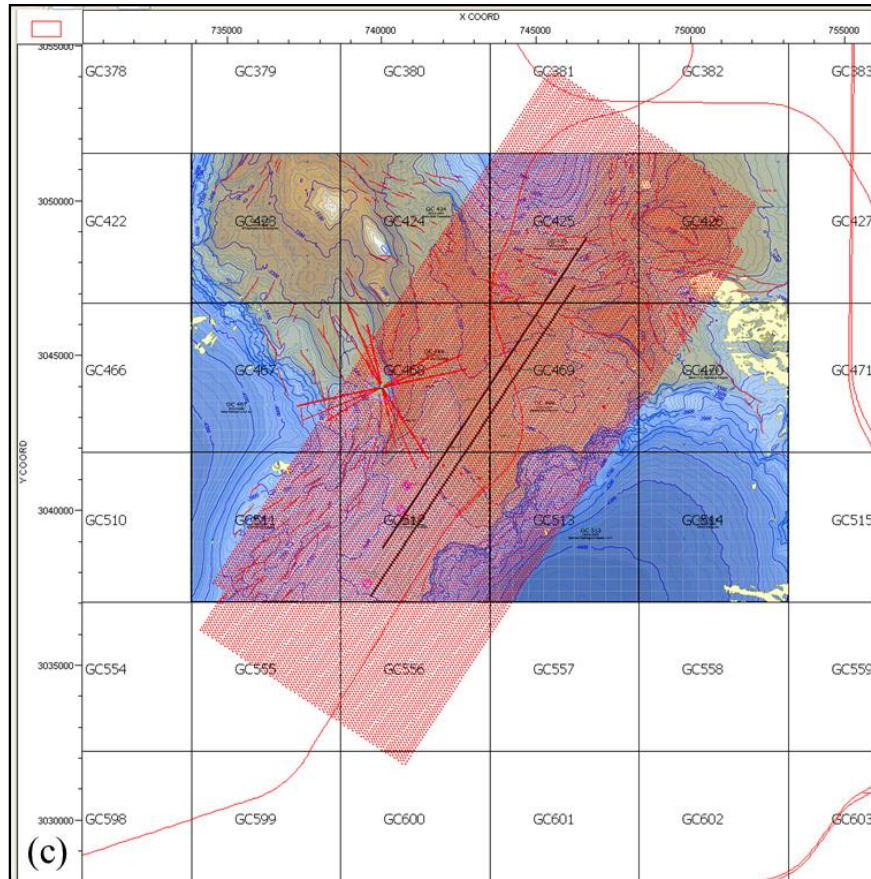
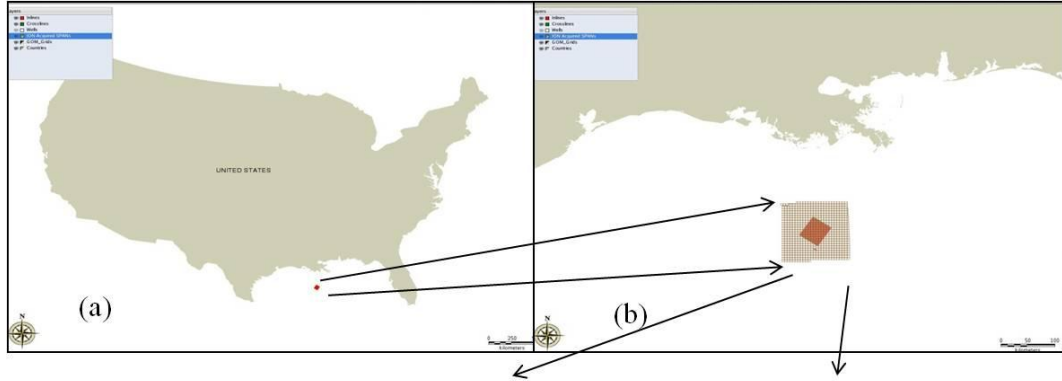
The work in this thesis was generated on the following hardware and software:

- The Sun Microsystems networks owned by the Department of Earth and Atmospheric Sciences at the University of Houston and operated by the Allied Geophysical Laboratory of the Department of Earth and Atmospheric Sciences.
- The GXT11 model building tool from the GXT geophysical company.
- The Promax systems owned and operated also by the GXT geophysical company.
- A velocity model building tool from the Economic Geophysical Laboratory, University Texas, Austin.

# Chapter 2: Area of Study

## 2.1 Location

The area in this study is in the deep water Green Canyon area of the Gulf of Mexico as shown in Figure 2.1.



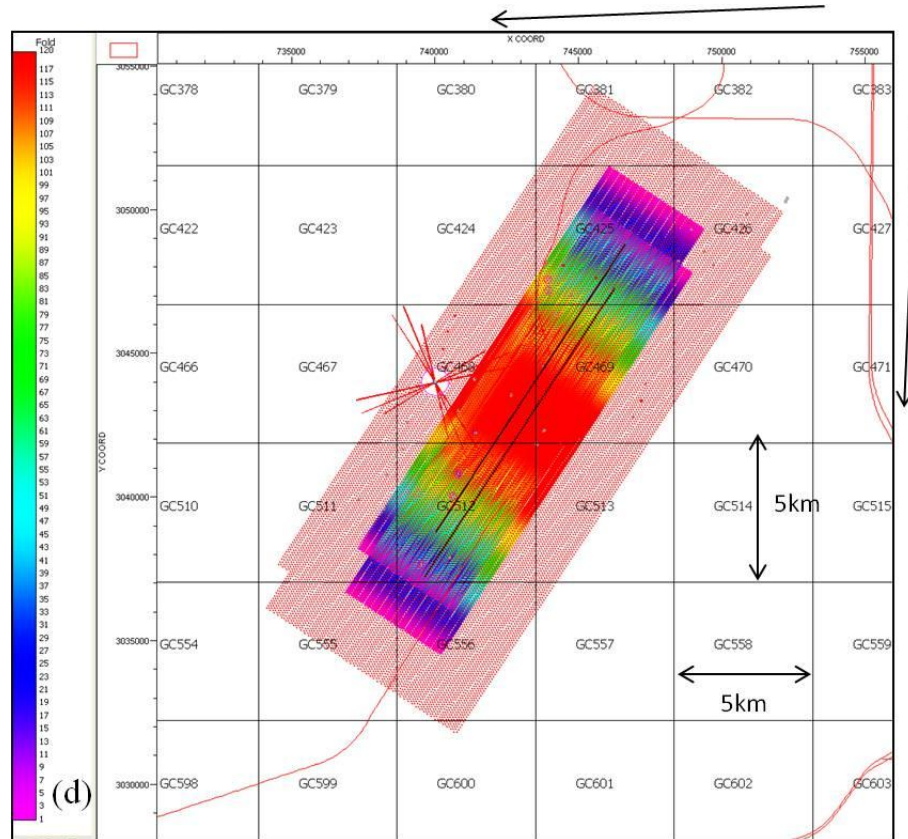


Figure 2.1: The location map of the seismic data used in the study. (a) The map of the United States of America and the red dot is the location of the Green Canyon in the Gulf of Mexico. (b) The enlargement shows grid location of the survey. (c) The layout of the source and receivers, the acquisition area is situated over GC blocks 468, 469, 512, and others at an angle of 34 degrees and each block is about 5km x 5km. (d) The fold map, two swaths were acquired and one of them was used for this study.

## 2.2 Geologic setting

### 2.2.1 Green Canyon, Gulf of Mexico

In the southern Green Canyon area in the continental slope of the Gulf of Mexico is the Sigsbee escarpment. There are fold belts and salt-related structures from deep basin

of the Gulf of Mexico up and under the Sigsbee salt sheet, which are believed to have hydrocarbon potential.

The importance of salt bodies in controlling the local structure and morphology in the Green Canyon area is indicated by the recent fault movement that changes the fault structure on the Sigsbee escarpment to a graben structure, which Orange et al. (2004) believe coincides with the southward limits of the salt diapir-cored ridge and has prominent slumping and toe thrusts. The Gulf of Mexico passive margin is believed to have formed during the breakup of Pangea (Buffler and Sawyer, 1985; Salvador, 1987, 1991; Feng et al., 1994; Bird et al., 2005). As a result of evaporation of sea water, up to several kilometers of salt were deposited during the Middle to Late Jurassic (Diegel et al., 1995). During the Oligocene to Miocene these sediments (Mesozoic and Cenozoic) accumulated and made the salt become mobile and allochthonous (Diegel et al., 1995). These sediments on a mobile salt substrate have had primary control on the stratigraphy of the Gulf of Mexico since the Miocene (Madoff et al., 2009). Amery, (1969) with a profile across the Sigsbee scarp interpreted a salt layer that extruded a 10km distance over flat laying beds over the south of the scarp. Large volumes of gas hydrates are also known to concentrate in smaller volumes of sediments near the sea floor in the Gulf. Vertical migration along these fault parts concentrate these gas hydrates at edges of charged salt mini-basins, salt ridges, and near the Sigsbee escarpment (Sassen et al., 2001a,b,c)

There is believed to be fold and volume potential under the Sigsbee salt sheet that bounds the Perdido, Walker Ridge, and Mississippi fan foldbelts on three sides (Anderson et al., 2009). Thus, the salt is believed to be the dominant structural element of

the Gulf of Mexico petroleum system (Figure 2.2 and Figure 2.3). The salt which dominates the Sigsbee escarpment is also believed to be driven by the Plio-Pleistocene to Oligocene sediment from the Mississippi, Rio Grande, and other Gulf coast rivers. The Sigsbee salt sheet is at the moment overriding the compressional northwest to southeast trending foldbelts. This is believed to be caused by gravity sliding in the Middle to Upper Oligocene time.

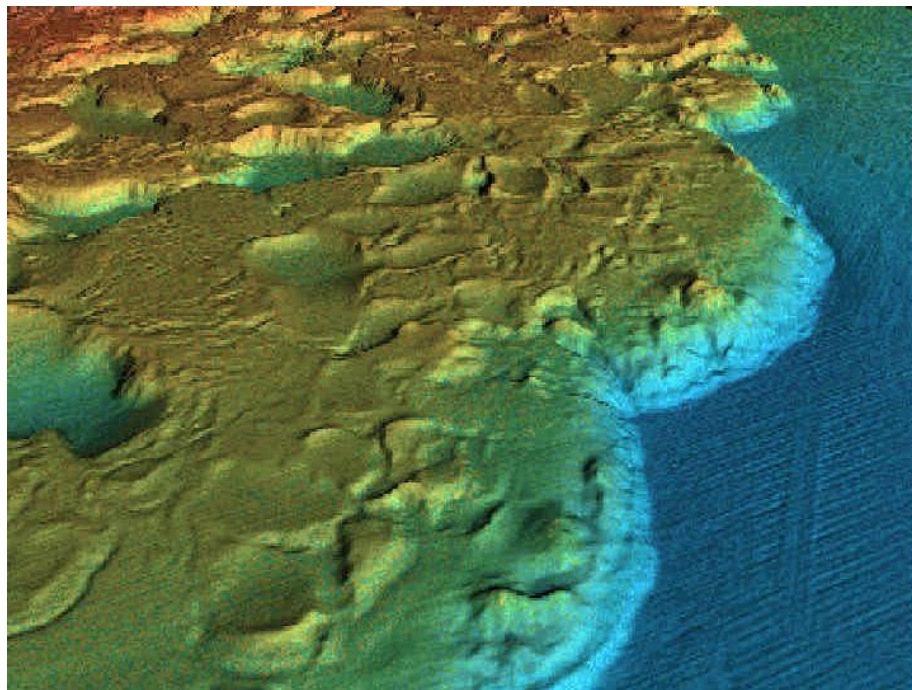


Figure 2.2: The diagram shows the Sigsbee salt sheet and the escarpment on the right that forms the cliff unto the abyssal plain of the Gulf (Anderson et al., 2009).

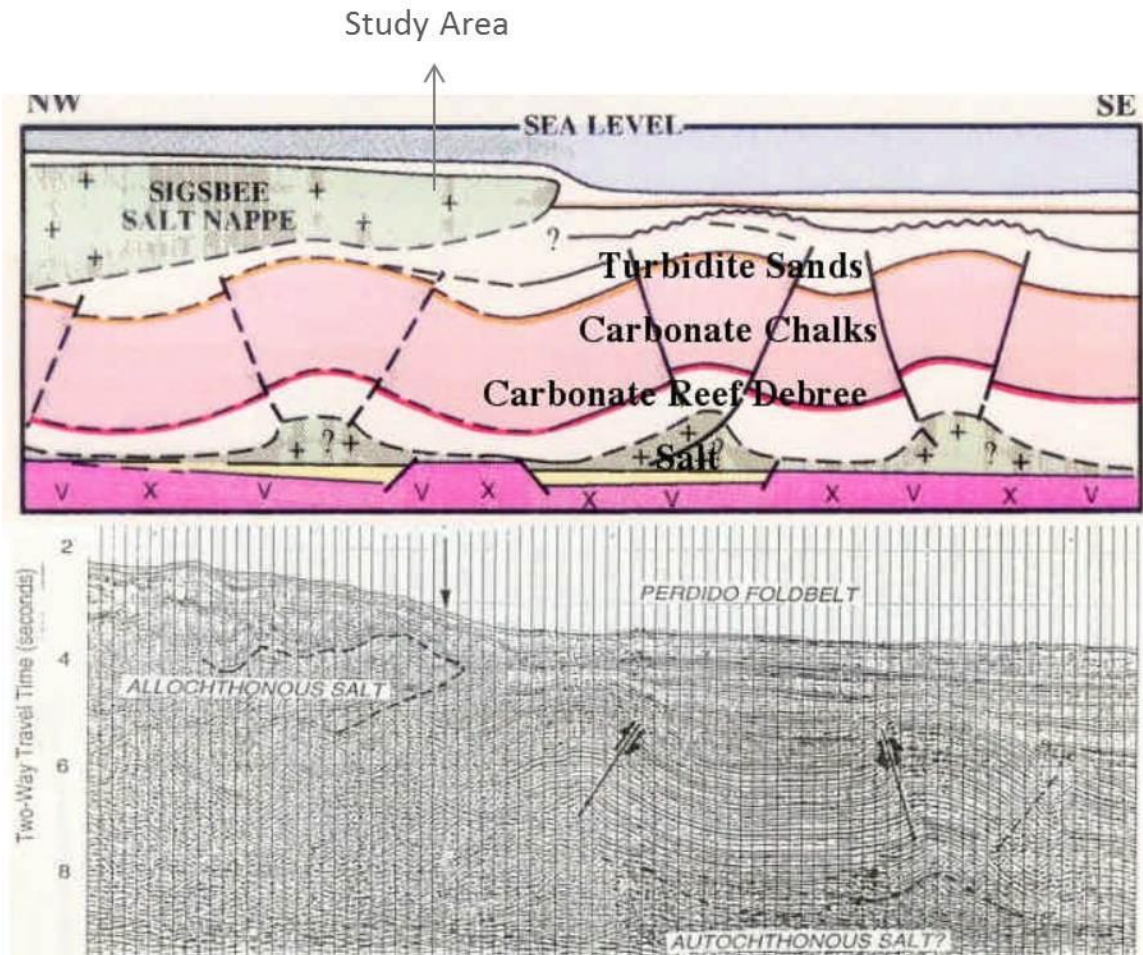


Figure 2.3: The section shows the structure in the foldbelts in the Gulf of Mexico overlain by the Sigsbee salt sheet (Anderson et al., 2009). The arrow indicates the area of study.

Within the embayment and holes through the Sigsbee salt sheet are folds that could be mapped and core data from wells to the south helped confirm this interpretation (Anderson et al., 2009). Many of the folds show evidence of bi-directional reverse faulting, and there is expectation that hydrocarbon could be trapped in these variety of structural and stratigraphic settings. An example is the giant Baha structure located in the Alaminos Canyon with faulted four-way closure. Seismic velocities decline are the main indication of porosity and hydrocarbon in the pay zones believed to be comprised of

turbidites sands, fractured and porous chalks, and fore-reef carbonate within the anticline (Anderson et al., 2009).

## 2.3 Seismic data

### 2.3.1 Acquisition

The data used in this thesis were acquired by ION GX Technology in swath shooting using the ocean-bottom four-component VectorSeisOcean (VSO) system in deep water (1000+ meters) and over relatively shallow salt bodies. Two swaths were acquired on two receiver lines, 11,950m long, with 520m receiver line spacing and receiver interval of 50m.

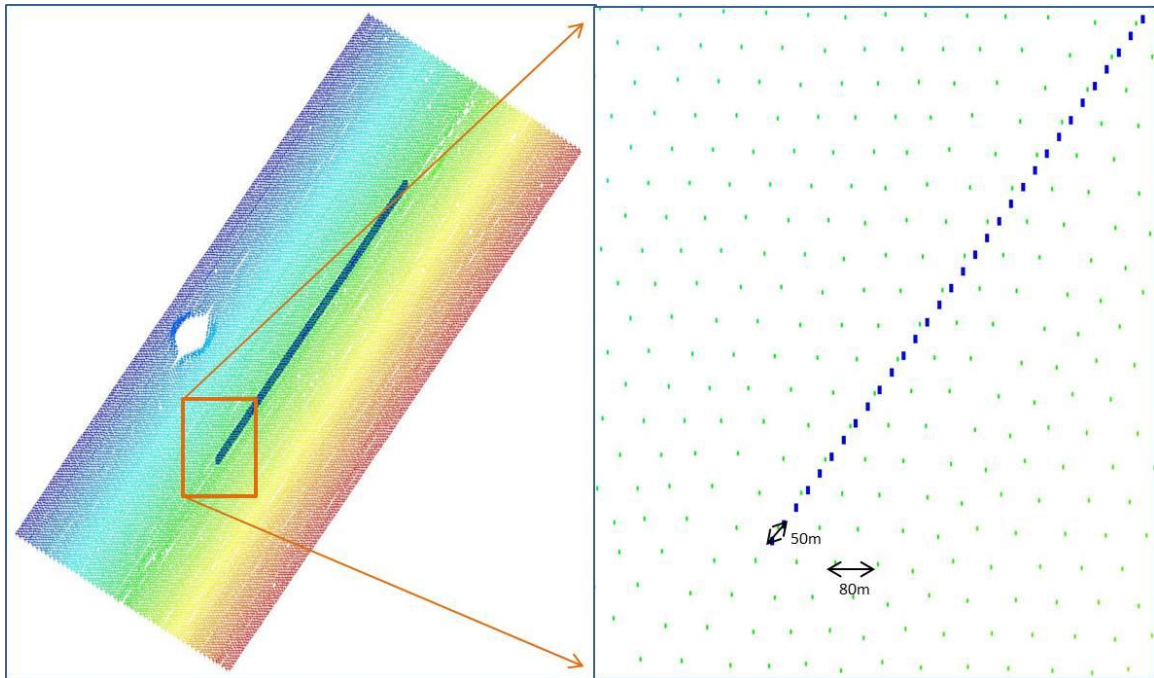


Figure 2.4: A schematic showing receivers (blue dots) and sources (green dots) spacing.

The source line spacing is 80m and the source depths are 8m. There were 50 sail lines per swath (25NW, 25SE of the receiver line). The sail line distance is 1000km per

swath and the total number of shots is 19,950 per swath. There were 20s of data recorded in 2ms sample interval and re-sampled to 4ms.

### 2.3.2 Preprocessing

The following steps describe the processing that was applied to data in the vertical, radial and transverse components:

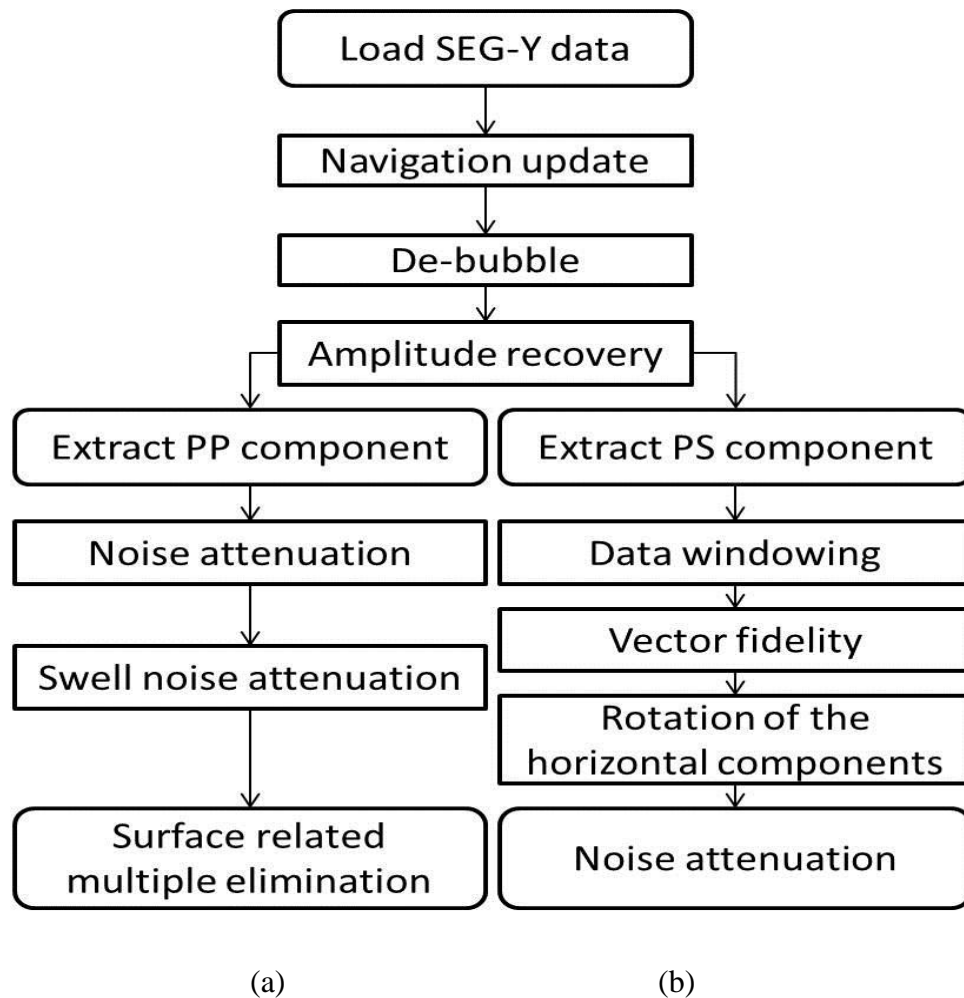


Figure 2.5: The entire preprocessing flow showing (a) The PP preprocessing arm of the flow and; (b) The PS preprocessing arm of the flow.

### 2.3.3 Load SEG-Y data

Seismic data were loaded as SEG-Y data, resampled to 4ms from 2ms and had headers remapped to Promax format. The purpose for resampling from the sampling theorem (Shannon, 1949) is to prevent aliasing in the data. Considering the frequency aspect of sampling, when we resample closely along the waveform, we construct a new wave from the sample and resulting waveform is same as the original. This is done to preserve sufficient information from the input waveform necessary to reconstruct an identical waveform without sampling more than is needed to achieve this. This is also done using a conventional Finite Impulse Response (FIR) convolutional filter which is equivalent to the Butterworth filters used in a general case. This could also be done to have less data.

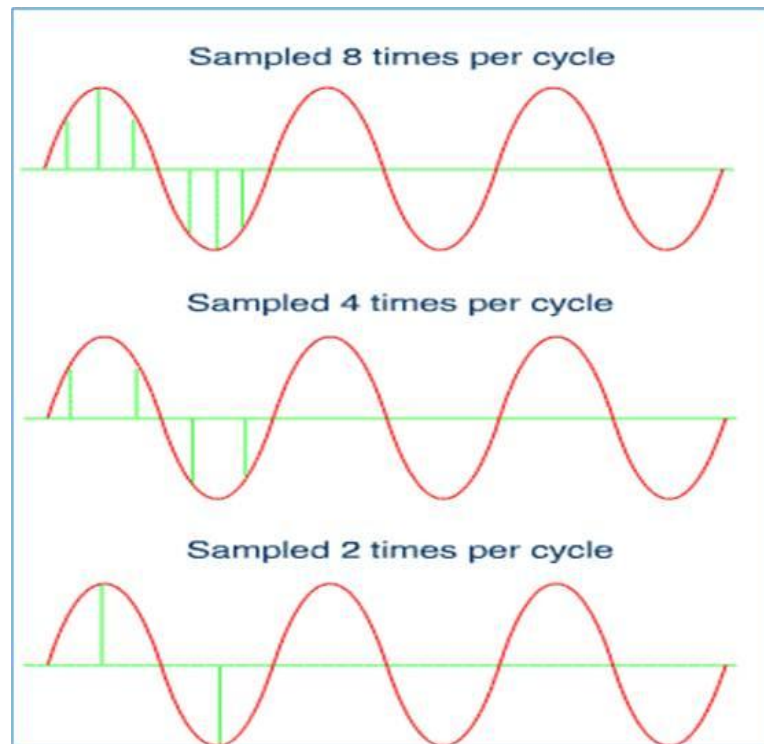


Figure 2.6: The schematic describes resampling process.

Some of the unique headers written out are the Swath number, sail-line number, receiver station/line number, inline number, crossline number and the coordinate location numbers. Care was taken to the headers were remapped from the correct location in the seg-y header files in order to appropriately carry on time processing without errors introduced into the process. Another important parameter to consider for loading seg-y data is the length of trace (18s for this dataset), this would important if one wants to read a shorter record length.

### **2.3.4 Data preparation**

Navigation QC was also done before the P, Z, X, and Y components were extracted into separate files. This is to enable the shot-point ranges match those in the Observers log and check for any missing shots. To achieve this, the navigation file is required to extract information about the coordinates of the source and receiver locations, the water depth, the receiver depth and the time of shot. These are also part of the headers matched in the navigation merge. Also headers like the offset, CDP coordinate locations, CDP numbering and the direct arrival times are updated using the appropriate formulas from basic trigonometry. The traces that are not updated were identified from quality control displays generated and were dropped.

The offset is updated with the formula below:

$$\text{offset} = \sqrt{(\text{sou\_x} - \text{rec\_x})^2 + (\text{sou\_y} - \text{rec\_y})^2},$$

where sou\_x, sou\_y, rec\_x, and rec\_y are the source and receiver coordinate locations.

The common depth point coordinate locations (cdp) are updated as shown below:

For the cdp x and y coordinate locations:

$$\text{cdp x location} = (\text{sou\_x} + \text{rec\_x})/2$$

$$\text{cdp y location} = (\text{sou\_y} + \text{rec\_y})/2.$$

Also, each cdp number is updated to give a unique identifier to each cdp location using the new station (new\_stn), channel (chan), shot increment value (shotincr) and the near channel value (nearchan) as shown below :

$$\text{cdp number} = \text{int}(\text{new\_stn} - ((\text{chan}-1) * \text{shotincr})) \text{ for nearchan}=1.$$

Then the direct arrival times estimated from the water column velocity as shown below:

$$\text{Direct arrival} = \text{offset}(\text{km}) / 1.5 \text{ (where 1.5 km/s is water velocity).}$$

### **2.3.5 The De-bubble filter**

The de-bubble filter was derived from the airgun signature generated from each component zero offset section. This signature was derived from the downgoing wavefield generated and applied to all components. This is required to remove the bubble energy generated by the airgun that appears like the ringing energy in the single trace display (Figure 2.7, Figure 2.8 and Figure 2.9)

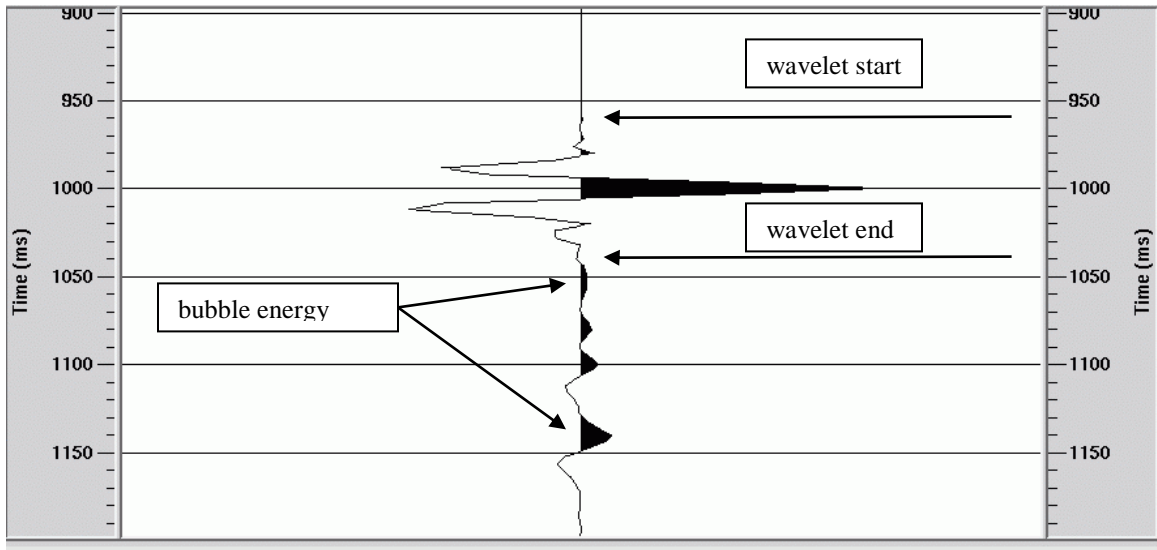


Figure 2.7: The source signature in display, showing the times at which the wavelet starts (first trough) and right before the bubble starts.

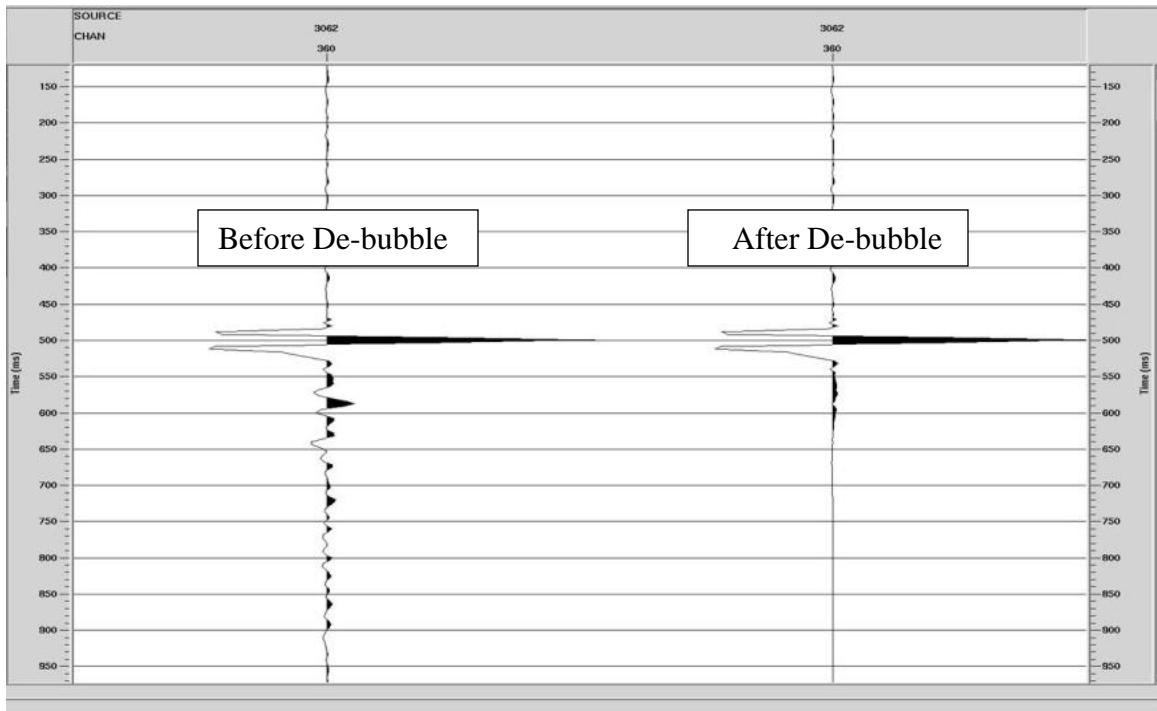
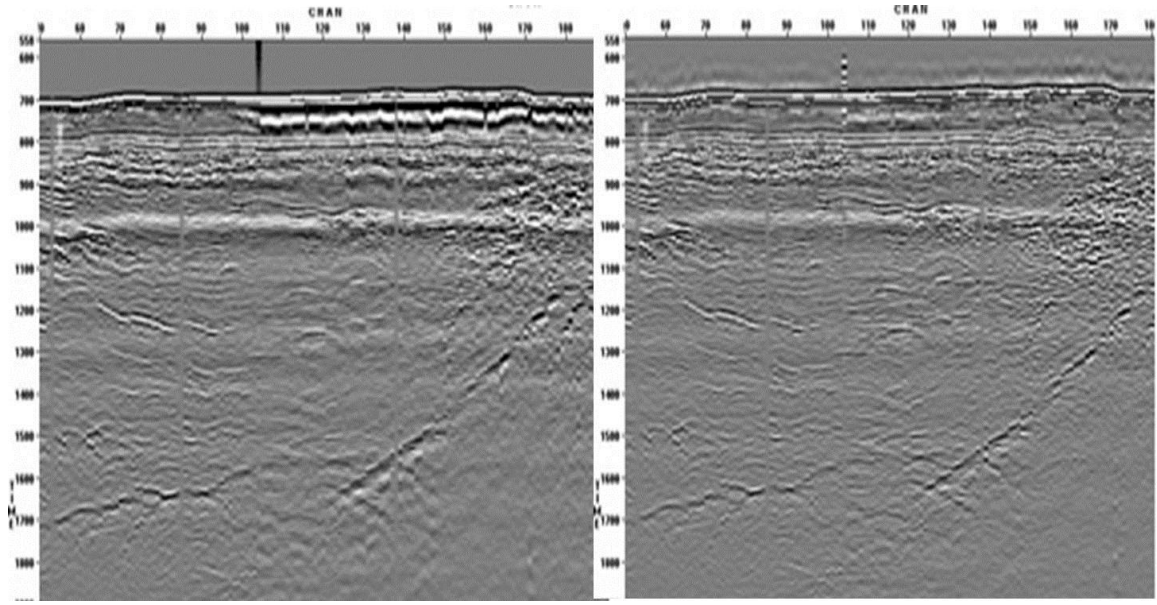


Figure 2.8: Trace with the ringing noise compared to the de-bubbled trace



(a)

(b)

Figure 2.9: (a) PS receiver stack dataset with the ringing noise before applying the de-bubble filter (b) PS receiver stack dataset with the ringing noise after applying the de-bubble filter.

### 2.3.6 Amplitude recovery correction and noise attenuation:

The data were gained using a time gain with a time-power constant of 1.9. Then bad receiver locations were edited and noise attenuation applied to the each component. The noise targeted is the anomalous amplitude, mostly low-frequency noise using the anomalous amplitude scanning technique. If this noise is ignored in the seismic dataset, it would cause noise smears in the dataset when migrated in the later processes. To filter them out, a group of traces (usually 5- 31 traces) is used with the aim to find a threshold at which all the traces with these anomalous amplitudes can be identified and attenuated. This is done by comparing amplitudes of neighboring traces within a sliding window (Elboth et al., 2008). The anomalous amplitudes are selectively zeroed on the trace (killing the trace is an option not often recommended).

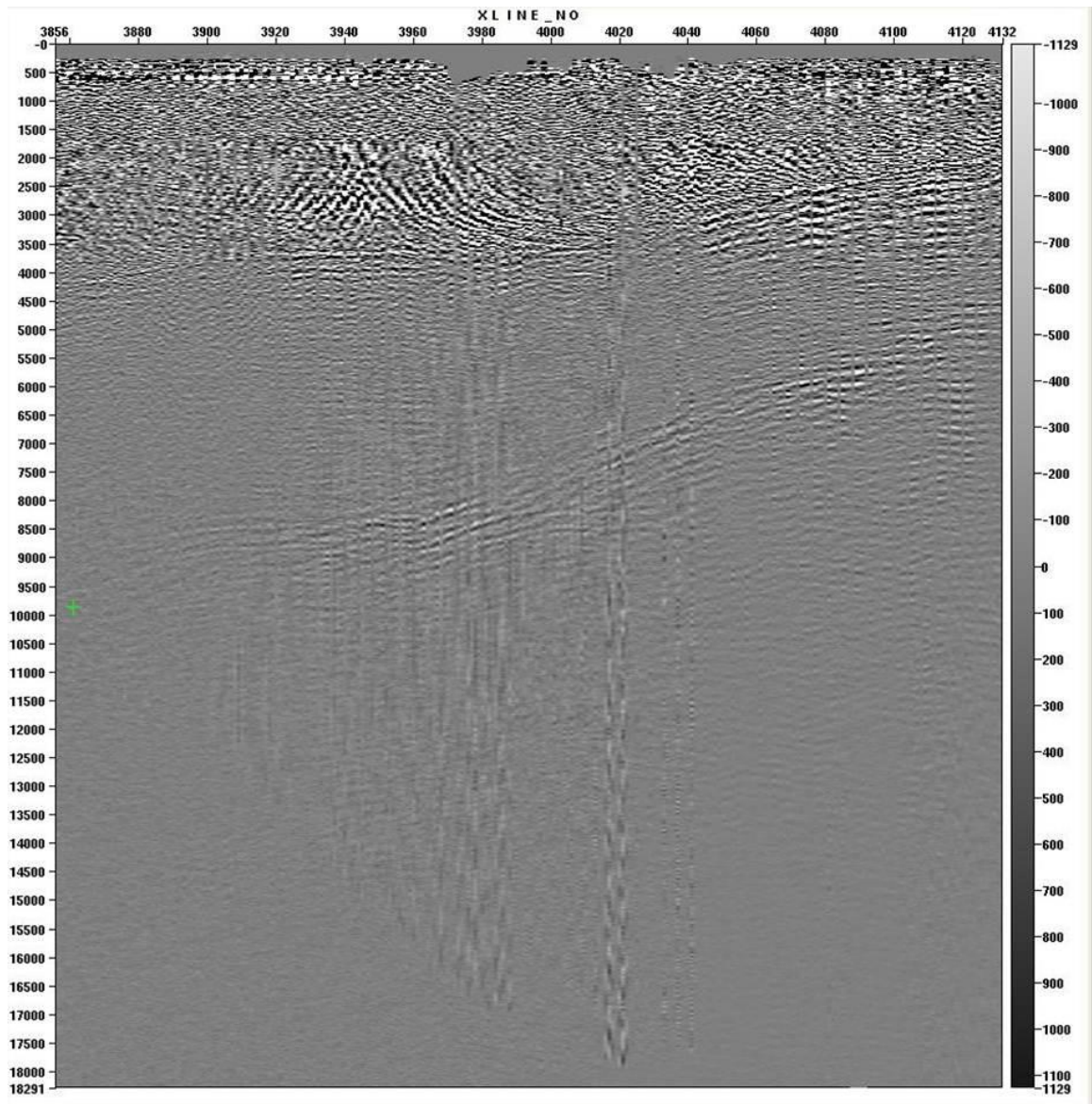


Figure 2.10: (a) PS seismic dataset stack before noise attenuation.

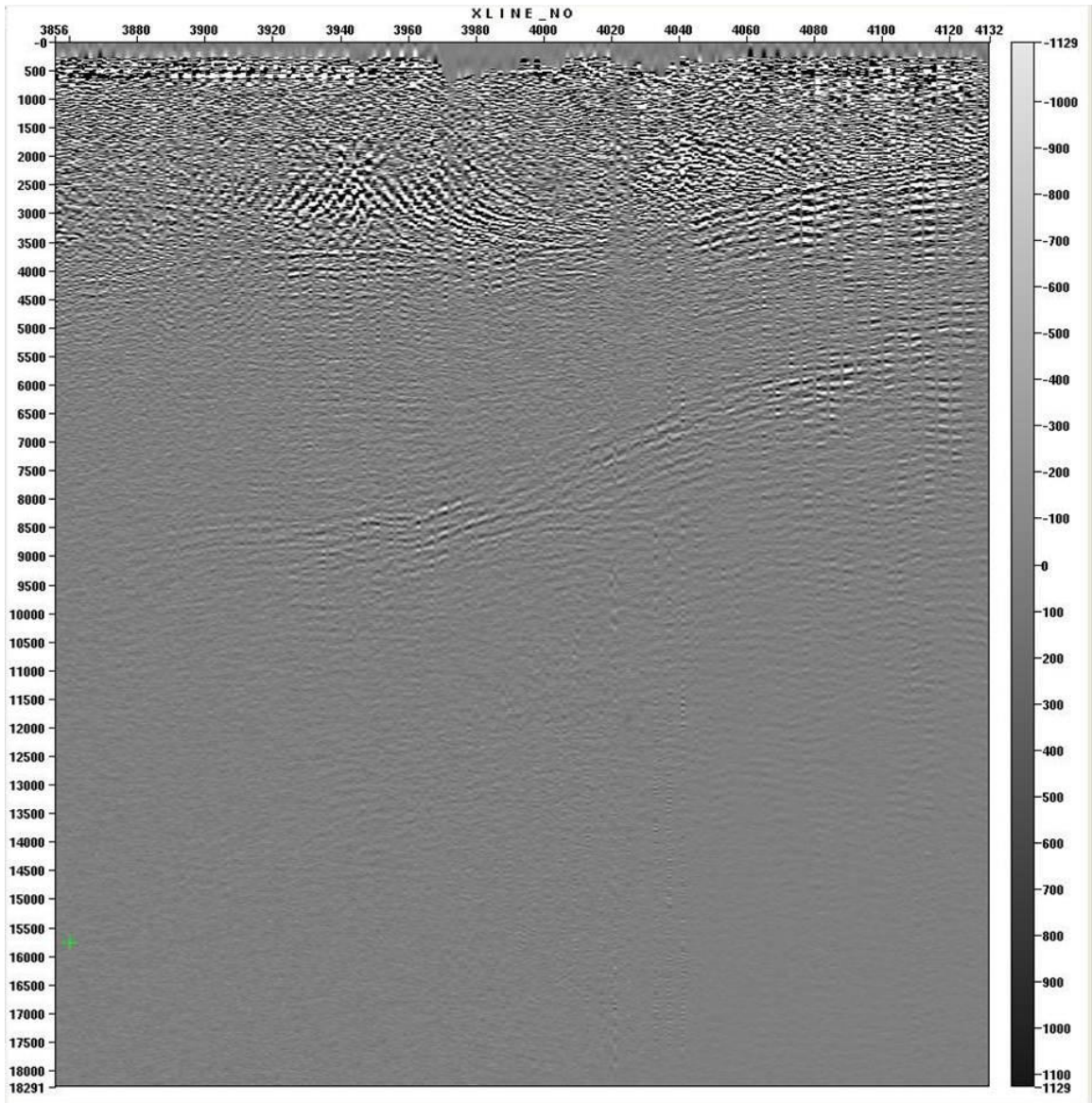


Figure 2.10: (b) PS seismic dataset stack after noise attenuation.

### **2.3.7 Data windowing**

Data windowing is a process done by applying a time shift to horizontally align the direct wave (the calibration event) and is applied to the three components. The reference time of 100 ms was used as datum and velocity used for shifting the data was  $V_{H_2O}=1504$  m/s with maximum offset was 3 km. The calibration event contained 12 samples in time (48 ms in 4 ms data). Figure 2.11 and Figure 2.12 show the frequency spectra for the PP and PS shot gathers respectively.

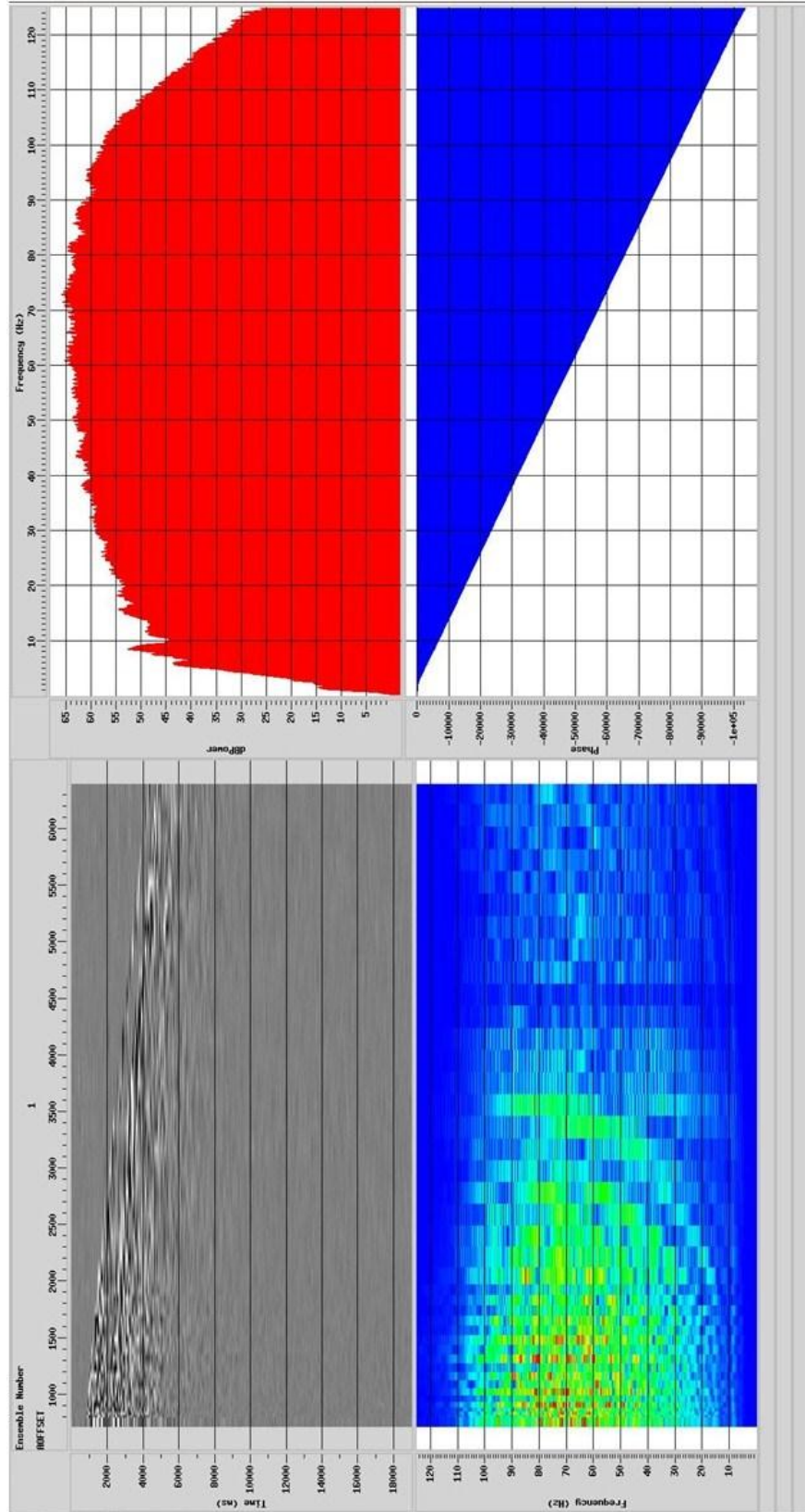


Figure 2.11: The frequency spectrum generated from the PP shot gather.

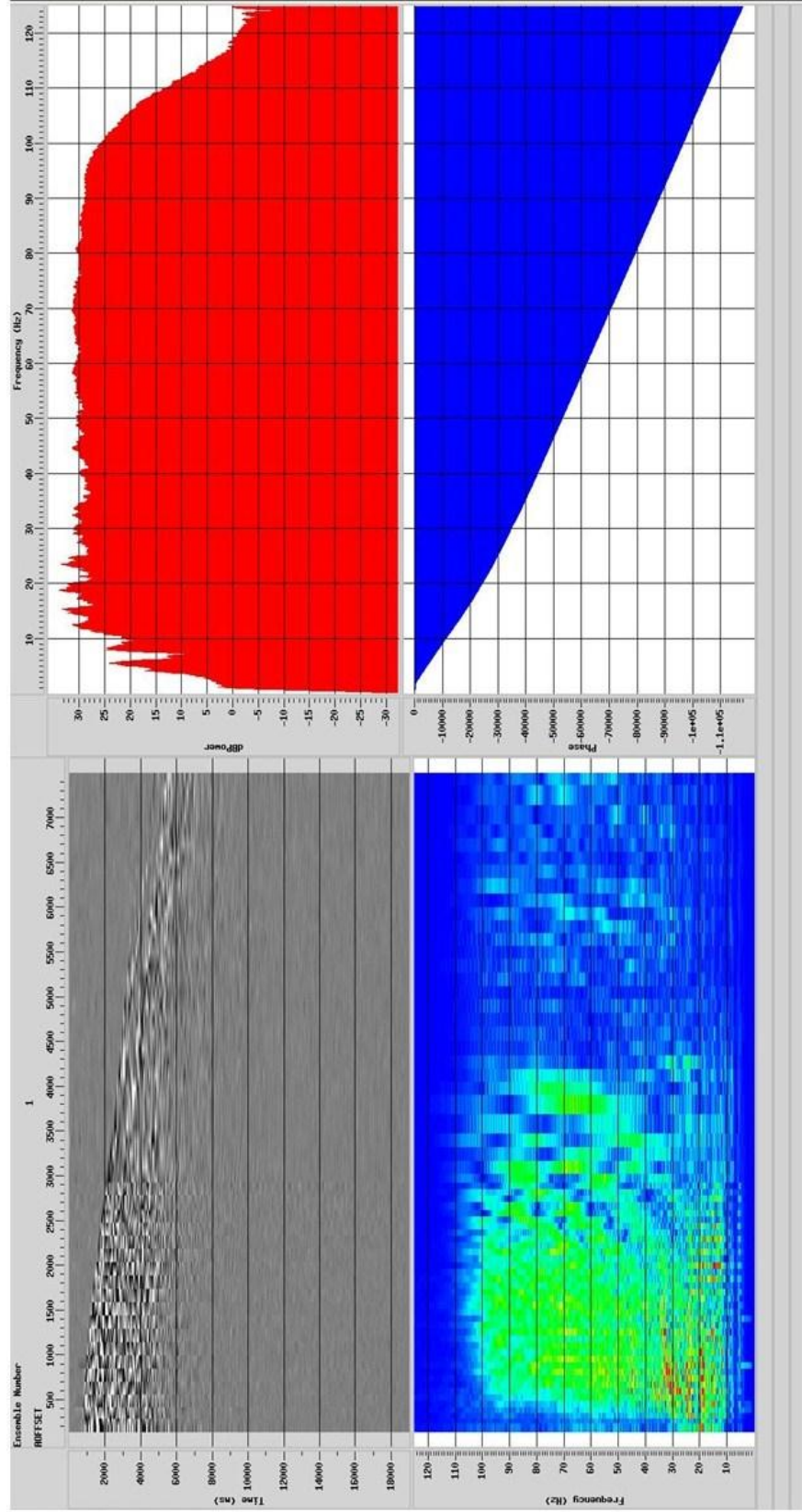


Figure 2.12: The frequency spectrum from the PS shot gather (horizontal component).

### **2.3.8 Design and application of vector fidelity operators**

Vector fidelity was introduced by Tree (1999); for an ocean bottom seismic (OBS) acquisition to have vector fidelity, true motion must be recorded or estimated in the magnitude and three directions of the multicomponent wavefield. Vector fidelity is necessary to process multicomponent seismic as a vector wavefield which includes designing a vector operator. Then application of the estimated vector fidelity operators results in components oriented in the vertical, north-south, and east-west directions. This approach was described in Dellinger et al. (2001) and performs the vector fidelity correction to common receiver sorted data. The method achieves vector fidelity by estimating a linear operator per receiver station and upon application causes the polarizations in the output data to track the expected polarizations of a calibrated event. This is expected to minimize the transverse energy on the data and outputs operators in 2 by 2 or 3 by 3 matrices, depending on what components are used in the input. The 3 by 3 matrix and the three components geophone data, were used for this data. Also, this method is expected to account for receiver rotation and receiver gain mismatches.

### **2.3.9 Rotation of the horizontal components**

The rotation of the horizontal components to obtain the radial component was carried out. This is necessary due to polarization effects due to azimuth variation of the source from the receiver. The typical ocean-bottom cable have 3 detectors (Figure 2.13) perpendicular to each other in the inline (x direction) and in the crossline direction (y

direction). Using a matrix equation, the rotation becomes a linear combination of the two horizontal components to get new inline and crossline with no change to the vertical as expected.

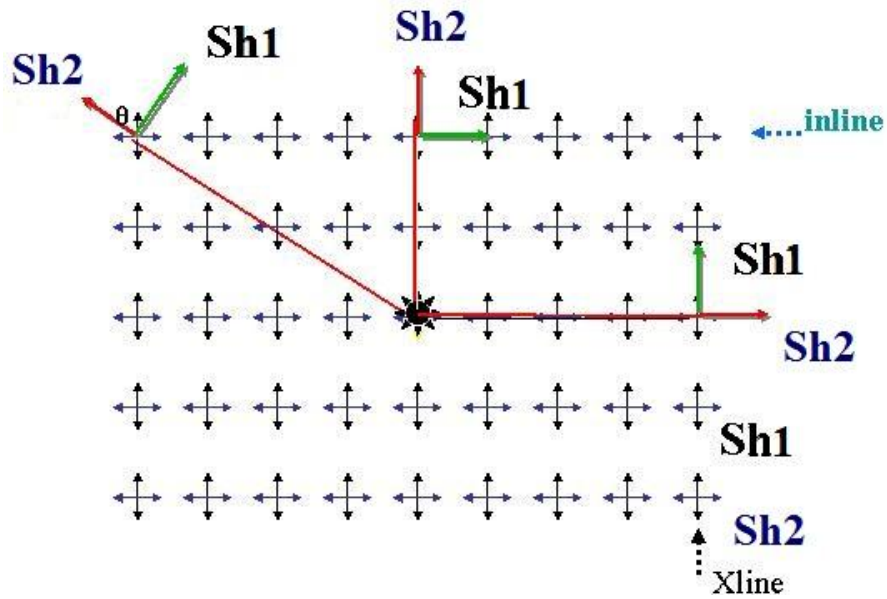


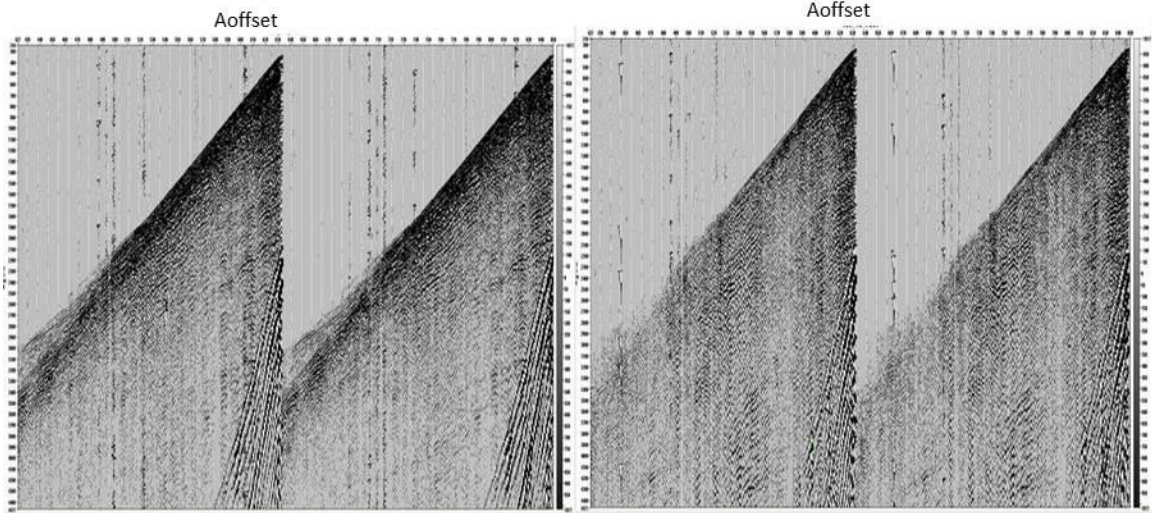
Figure 2.13: The schematic diagram shows the rotation of the horizontal components.

If

$$x'(t) = Rx(t)$$

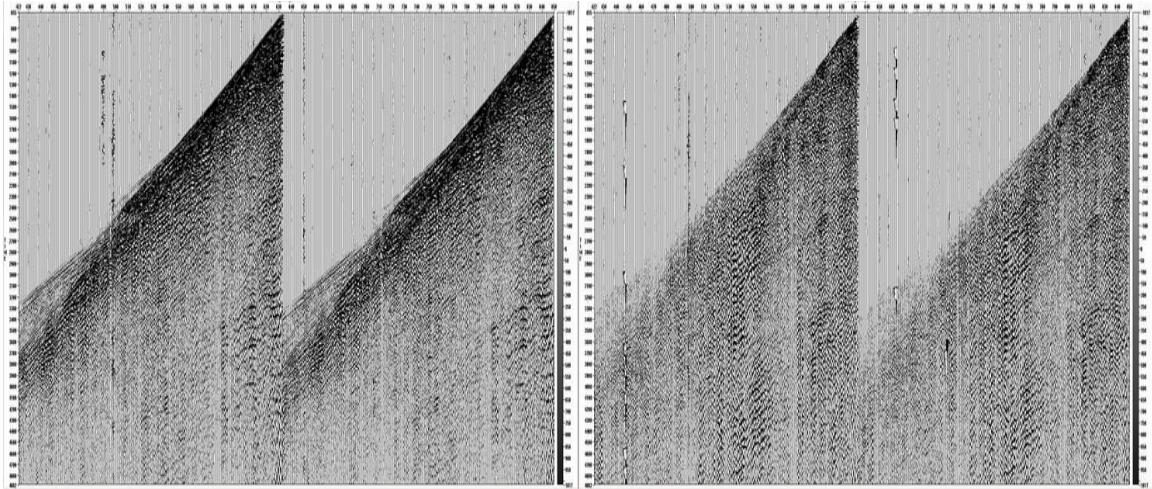
$$\begin{bmatrix} x' \\ y' \\ z' \end{bmatrix} = \begin{bmatrix} \cos\theta & \sin\theta & 0 \\ -\sin\theta & \cos\theta & 0 \\ 0 & 0 & 1 \end{bmatrix} \begin{bmatrix} x \\ y \\ z \end{bmatrix} \quad (2.1)$$

where  $\theta$  is the horizontal angle about the vertical direction for the rotation of the two horizontal components.



(a)

(b)



(c)

(d)

Figure 2.14: Gathers showing: (a) The radial component before rotation. (b) The transverse component before rotation. (c) The radial component after rotation showing stronger signal strength. (d) The transverse component after rotation showing lesser signal strength.

### 2.3.10 2D SRME – radial and transverse components

Removal of water column multiples on PS data uses surface related multiple elimination (SRME). SRME uses source and receiver information to predict and subtract the multiples. The procedure involves padding and extrapolating traces to zero offset, regularizing offset spacing; regularizing shot spacing as required to make equal source and receiver spacing; then predicting the multiples from specification of source and receiver distance; match by adaptive method; then subtracting the multiple and QC of the dataset show in Figure 2.5 dataset before and after multiple elimination.

The water velocity used to calculate the multiple header value is 1500m/s using the offset information the header and the formulae from trigonometry:

$$\text{Multiple} = \sqrt{(\text{waterbottom\_time} * 2)^2 + (\text{offset} / 1.5)^2}$$

where the water-bottom time has been updated in the navigation merge and the offset refers to the absolute offset. These values are calculated, saved in the header, and used the prediction of the multiple from the primary data. This takes out the water bottom reverberations and works better in shallow waters.

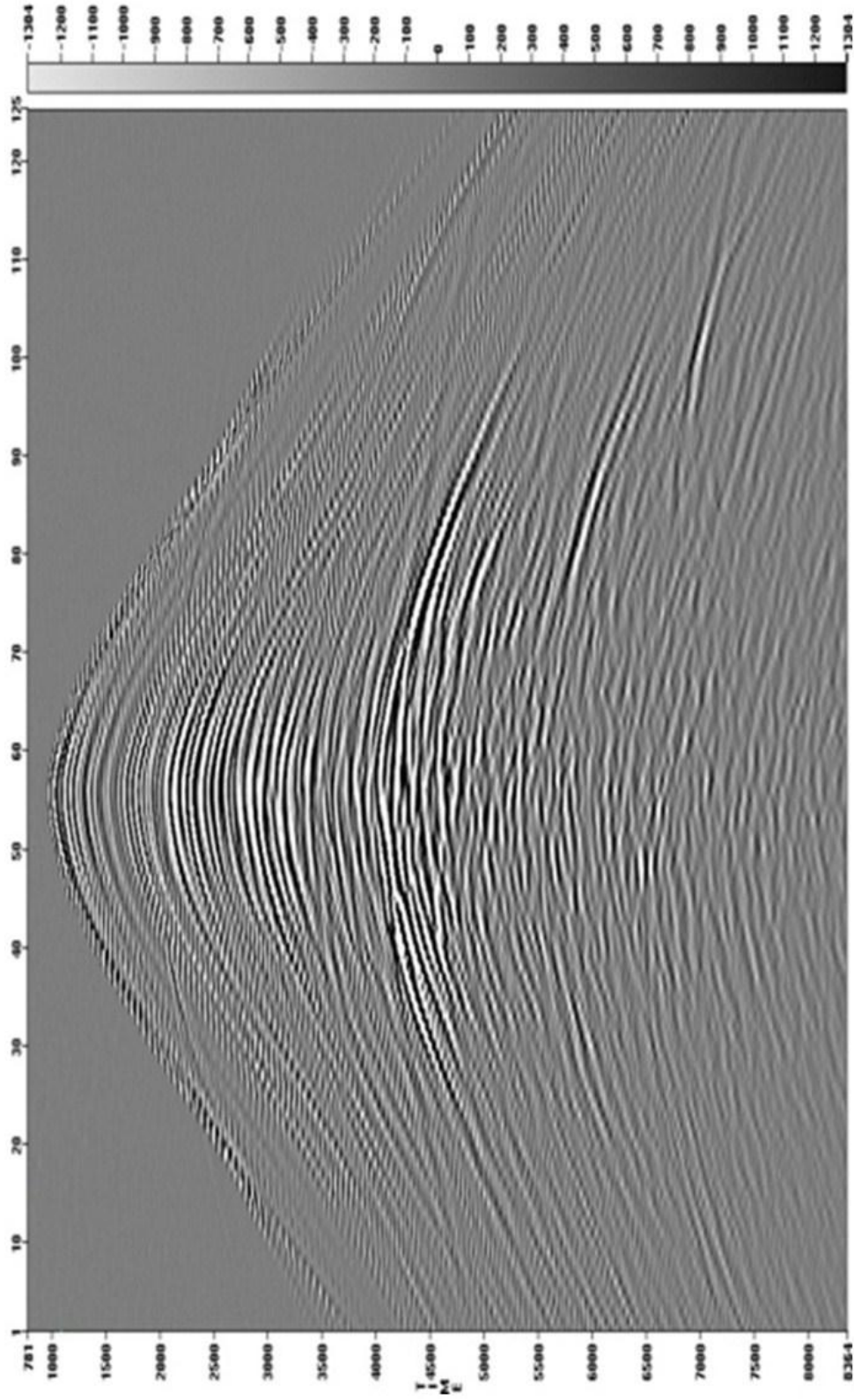


Figure 2.15: (a) Receiver gather for PS data before de-multiple filtering.

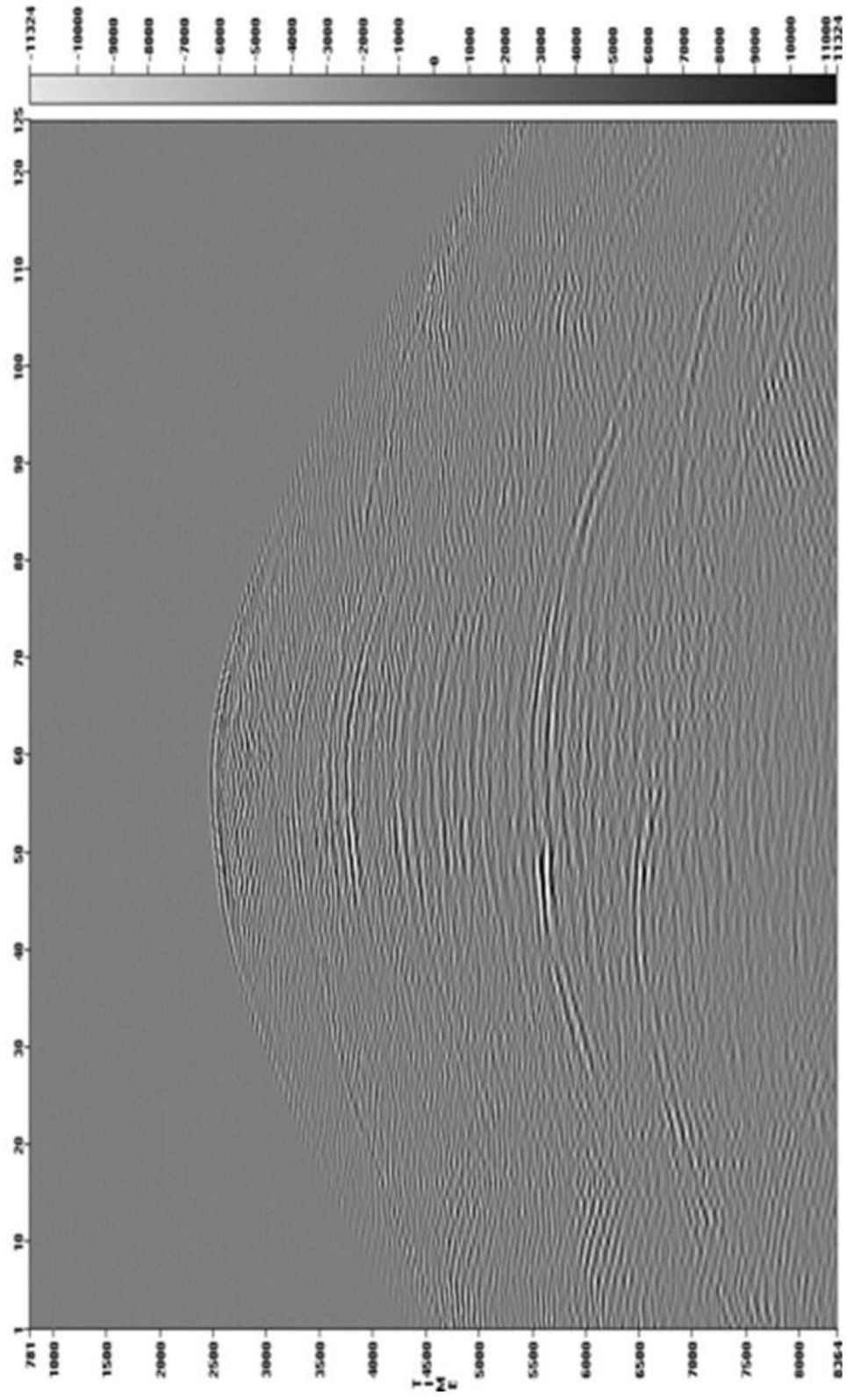


Figure 2.15: (b) 2D SRME multiple prediction on PS data.

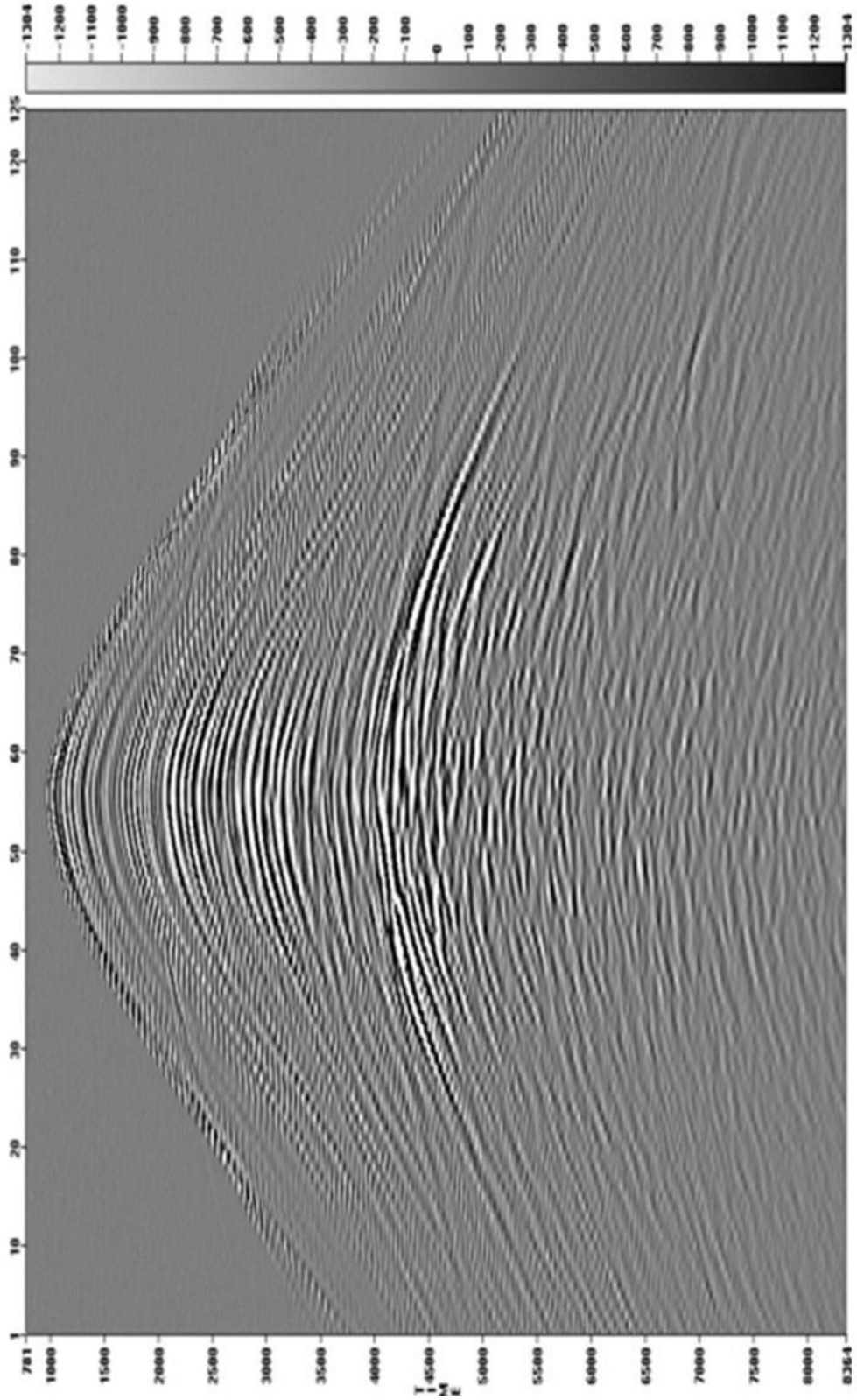


Figure 2.15: (c) Receiver data after subtracting the multiples.

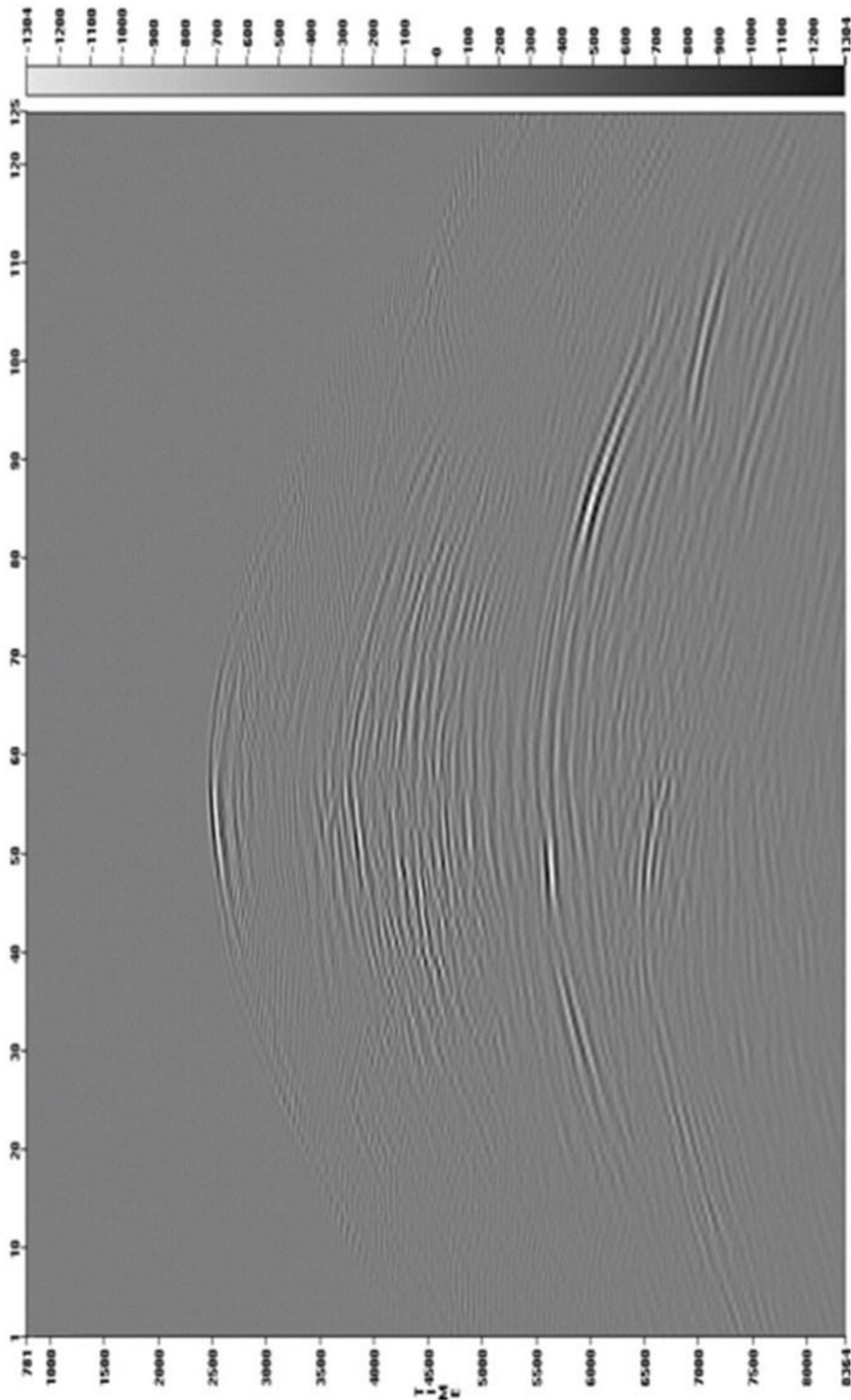


Figure 2.15: (d) The output from the multiple prediction and adaptive matching.

## **Chapter 3: The Ray-tracing Technique**

### **3.1 Introduction**

Ray tracing is often used to build, to test physical models, and to study how seismic energy is propagated through a multilayered medium with differing lithologies bearing pore fluids (Caldwell, 1999). This can be done by simulating the propagation of seismic energy in a physical medium in a two-dimensional format (Figure 3.1). The resulting display has two dimensions showing how the energy is reflected on various surfaces or horizons in the model. The travel-times and ray path is determined by properties of the layer and relative dip of the horizon. Ray tracing obeys Snell's law, the Figure 3.1 below shows the PP and PS rays traced from a single source to many receivers.

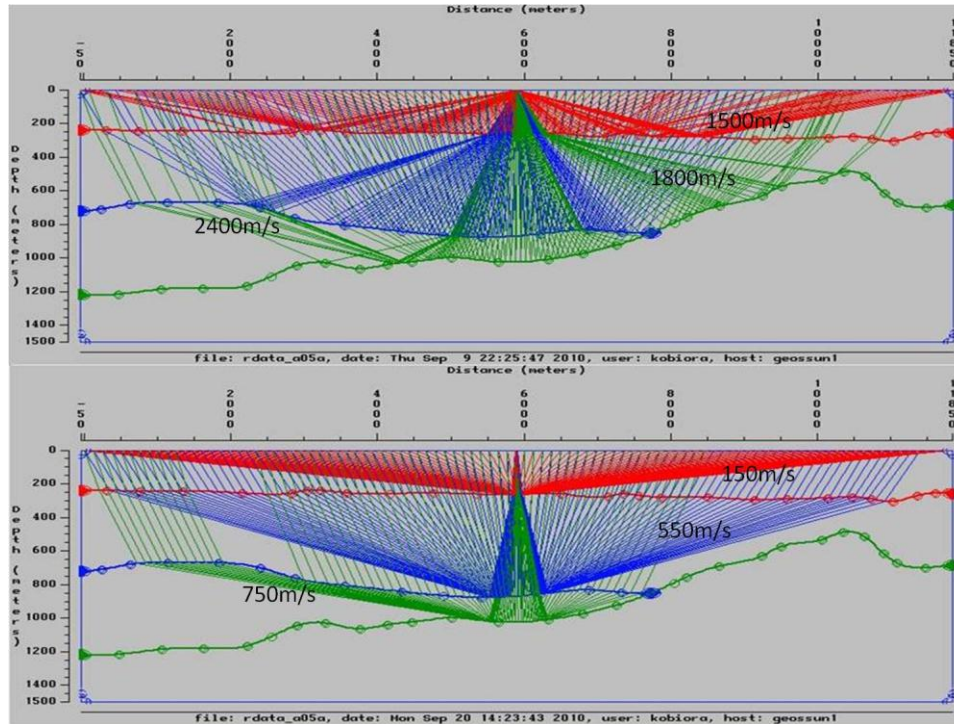


Figure 3.1: Ray tracing through the Horizons from the PP and PS reduced waterbottom receiver stacks created from the Earthwave software. The PP section is above and the PS section is below, created to show the coverage area for shots going into a common receiver PP gather is more than the coverage area for shots going into the PS common receiver gather.

### 3.2 The uses of the ray-tracing technique

Ray tracing is known to be useful in the following areas described below.

#### 3.2.1 Trace generation

When a physical model has been defined, synthetic seismic traces could be generated by defining other parameters like velocity, density, impedance, and geometry of source and receivers. The simulation of this process is used to demonstrate the important part played by the velocity model in seismic acquisition for PS wave surveys.

The velocity estimates for the study area was used in performing the task of synthetic traces generation and discussed in the later part of this chapter.

### **3.2.2 Modeling**

The velocity model building process first starts with a time model with horizons specified and converted to a depth model using estimated rock properties like velocity. Then as an interpretative tool, we could use synthetic seismic sections to compare to the original interpreted seismic section and continue adjustment of the rock properties estimation process until they both fit the criteria satisfactorily. This process is an iterative process that requires careful quality control measures to ensure estimated parameters are true or an appropriate representation of actual area of study for the purpose of generating a better image. The big challenge is finding the technique that would satisfy this purpose and generate the model that gives a better seismic image for any further interpretation work that could be required.

### **3.2.3 Acquisition planning**

The ray-tracing technique can also be used for acquisition planning. As the ray traces show which horizons are imaged, it's especially important for determining source and receiver distances required to image a target. A brief demonstration using the seismic data from the area of study has been carried out in this chapter.

### **3.2.4 Geophysical challenges**

The need to estimate velocity, to define the type of velocity, and relocate reflected seismic energy to its true position in space and time has created the challenge to identify techniques that would estimate these parameters effectively and meet the objective of this PS survey. In this situation, how does one know that the ray-based technique is appropriate? What is the appropriate technique for generating a velocity model that could meet the objective of the PS-wave survey? What would be the criteria for choosing an appropriate algorithm for the purpose? This is the reason for choosing the ray-based technique for this study and then possibly using the estimated velocities as guide into the anisotropy-based technique in a later study. The entire process would involve estimating velocity from moveout information from digital recording and invert to estimate other local parameters.

In PP- or PS-wave propagation through the earth, there could be smooth velocity variation or a rapid velocity variation. How many of the elastic parameters could be accurately derived and how many of them properly account for the effects of anisotropy if any in the survey area? Once again, could ray-tracing provide answers to these challenges?

### **3.3 Ray-tracing technique workflow**

A processing flow (Figure 3.2) was set up for the purpose of this study. The first step was to input common receiver gathers with reduced water bottom time. The picked

horizons from a receiver stack section were imported into the velocity analysis module. Then  $V_p$  and  $V_s$  were estimated from shallow sea floor registration (Figure 3.4).

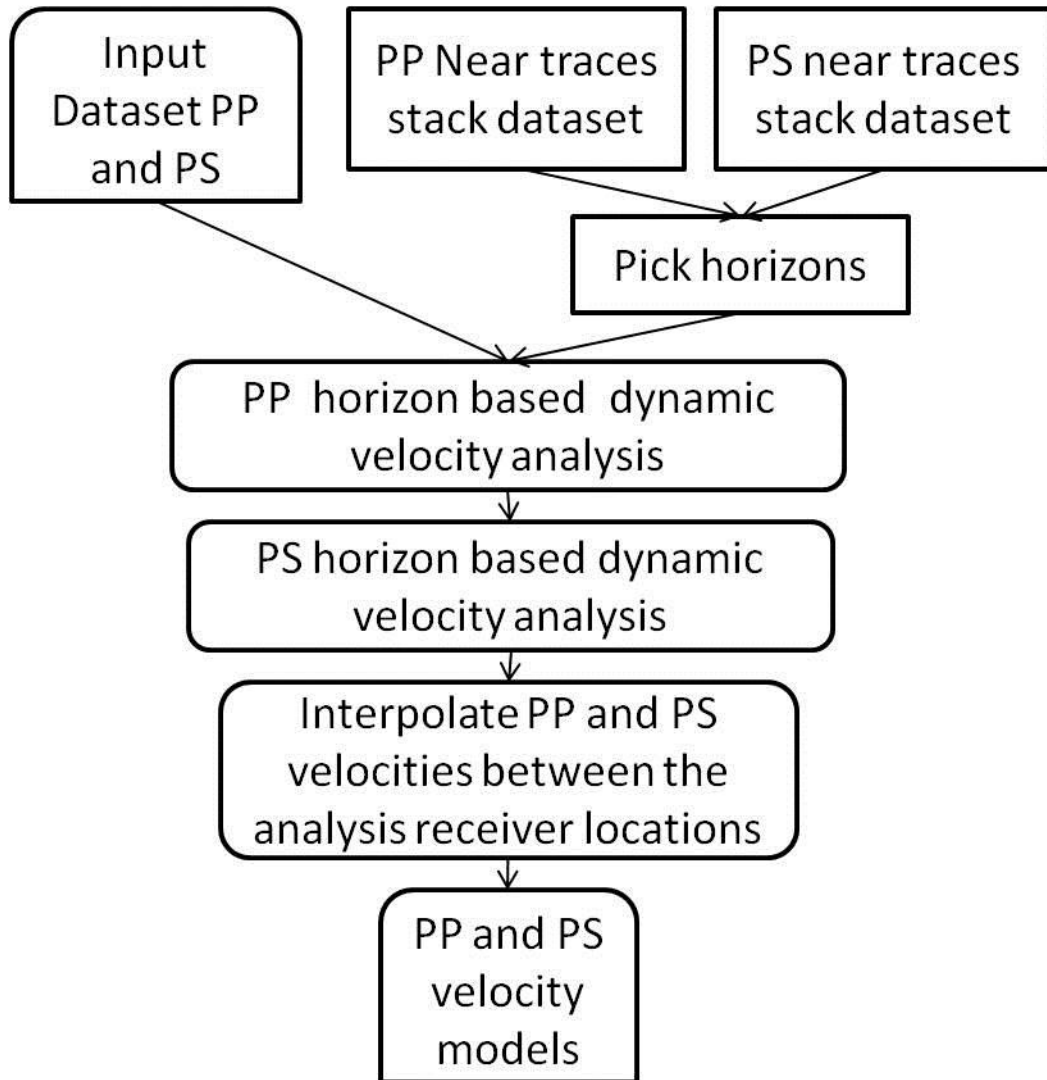
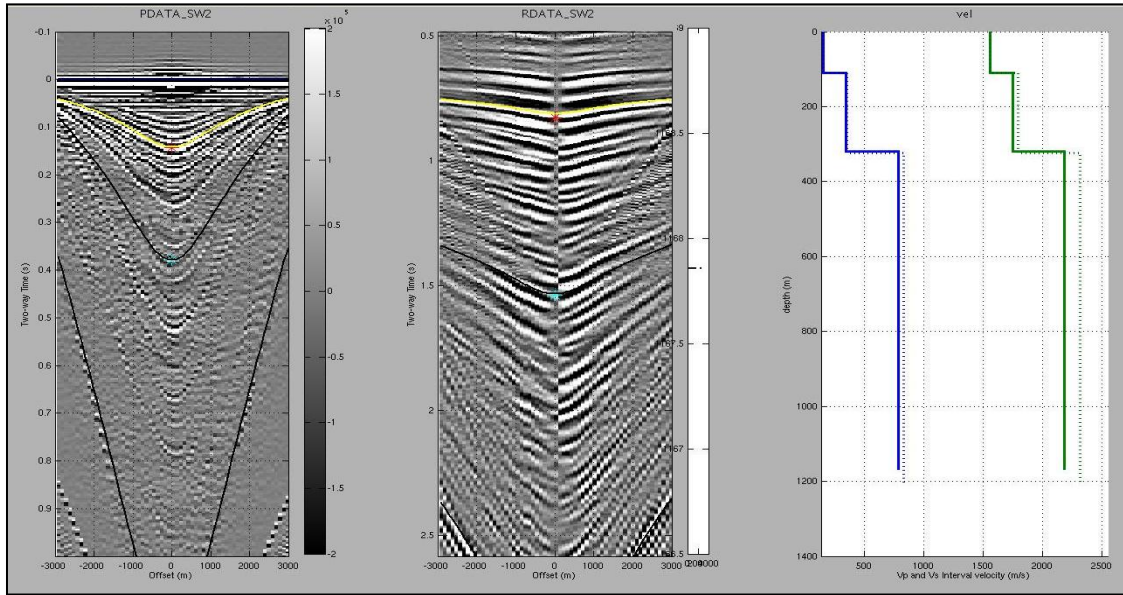


Figure 3.2: The processing flow for the ray-based technique.

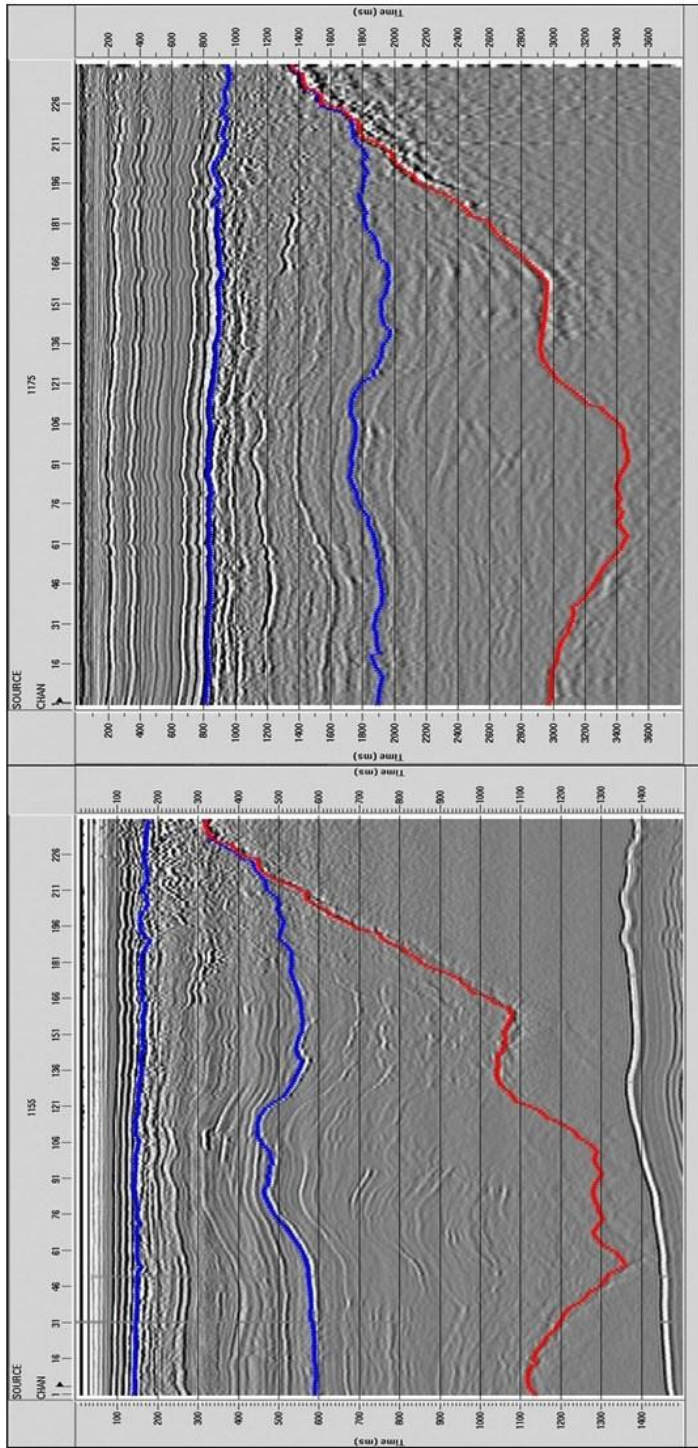


(a)

(b)

(c)

Figure 3.3: Common receiver gathers with imported horizons in the dynamic moveout analysis software from the EGL. The emphasis is to find the velocities that flatten the near traces on each horizon shown above assuming there is no hyperbolicity in the farther offsets due to the reduced water bottom. The first horizon is the yellow line shown on the gathers and next two horizons are the black ones. Three horizons were used in this study. (a) Shows the PP common receiver gather with the inserted horizons. When each horizon is selected, the appropriate velocity that flattens the events on the horizon is selected. (b) Shows the PS common receiver gather with the inserted horizons that are equivalent to the events on the PP common receiver gather, likewise there is an equivalent velocity that flattens the events on each selected horizon. (c) Shows the various velocities selected for each horizon in the both the PP and the PS data with green line representing the PP velocities and the slower blue line representing the PS velocities.



(a)

(b)

Figure 3.4: Common receiver limited offset stack, (200–400m). (a) The PP stack section. (b) The PS stack section. These stacks were created using Promax software and a constant water velocity.

### 3.3.1 The reduced water bottom receiver-line stack

The receiver-line stack was created using to gather traces closest to the receiver-line in order to get relatively flat near-traces. The water column (Figure 3.5) was removed using statics with the receivers and source locations moved to the same horizon.

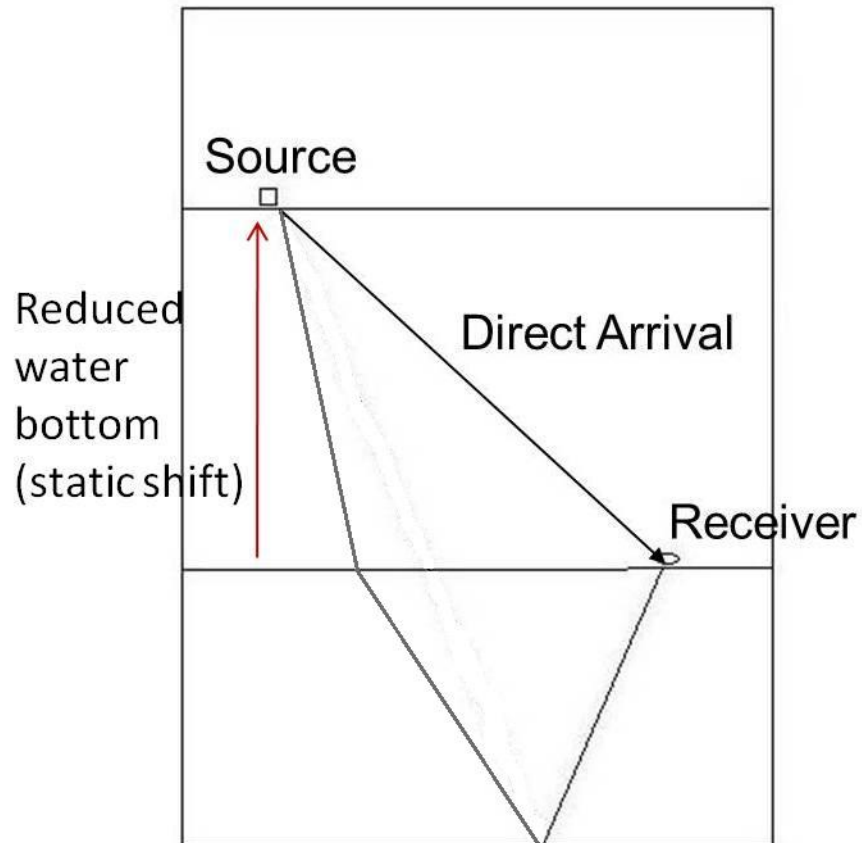


Figure 3.5: The water bottom reduced time for near-traces from receiver gathers account for the differences in source and receiver depths.

This was achievable using the source depth, receiver depth, and offset information available in the headers. Then using the formulae below from basic trigonometry, I

updated the newly created reduced water-bottom header before stacking the PP and PS receiver gathers.

$$\text{Reduced Water-bottom} = \text{Sqrt}(\text{offset}^{**2} + (\text{Receiver depth} - \text{Source depth})^{**2})$$

The horizons were picked on these stacks (Figure 3.4) to represent the same interpreted horizon in both the PP and the PS seismic modes. There are three horizons selected for this study, the third horizon represents the top of the shallow salt body believed to be present in the study area.

### **3.3.2 The shallow sea floor registration**

The shallow sea floor registration in this study was done using the first horizon in the 3 horizons that were picked on this data (Figure 3.4). After Backus et al., (2005), PP shallow velocity estimates of 1500-1600m/s in increments of 10m/s were displayed (Figure 3.5) and the best velocity that provides a flat event was chosen. The velocity was between 1550m/s and 1560m/s, using the estimated depth of 110m for the first horizon as shown in Figure 3.6, the PP wave shallow velocity estimate 1560m/s and assuming an error  $\pm 10\text{m/s}$ .

The PS shallow velocity was estimated from PP depth equivalent observed at 140ms and the PS reflection at 820ms (Figure 3.6).

$$V_s = \text{distance}/\text{time} = 110\text{m}/.750\text{s} = 147\text{m/s}$$

The time 750ms used in the calculation above is the travelttime of the PS wave, calculated from the difference between the PS reflection time (820ms) and the travel-time

of the down-going P-wave leg of the travel-time ( $0.5 \times 140\text{ms}$ ). These sorts of estimations for a given thickness of between horizons were used to manually constrain estimated velocity values within the velocity picking module. The software used for velocity picking was developed from the Exploration Geophysical Laboratory at the University of Texas. The velocities were all manually picked for each location.

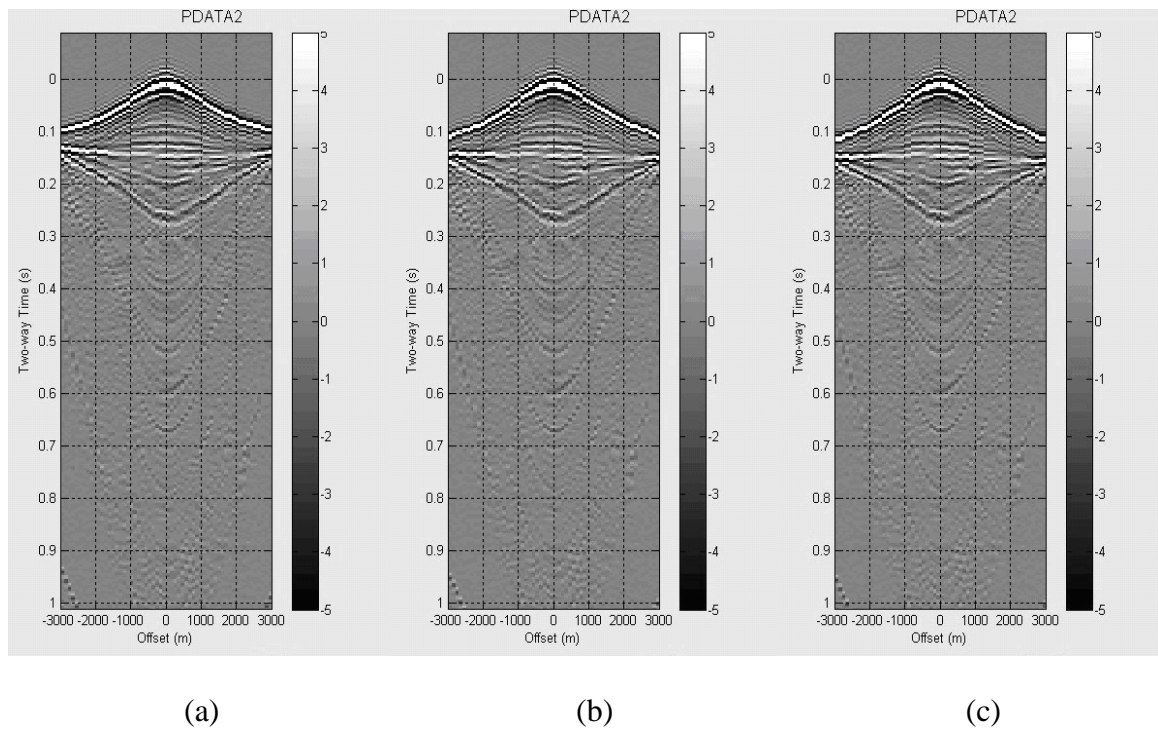


Figure 3.6: Velocity estimates of 1500m/s to 1600/s with increments of 10m/s were applied to flatten the gather. (a) is 1550m/s and (b) 1560m/s (middle panel) which best flattens the gathers was selected. (c) is flattened with 1570m/s.

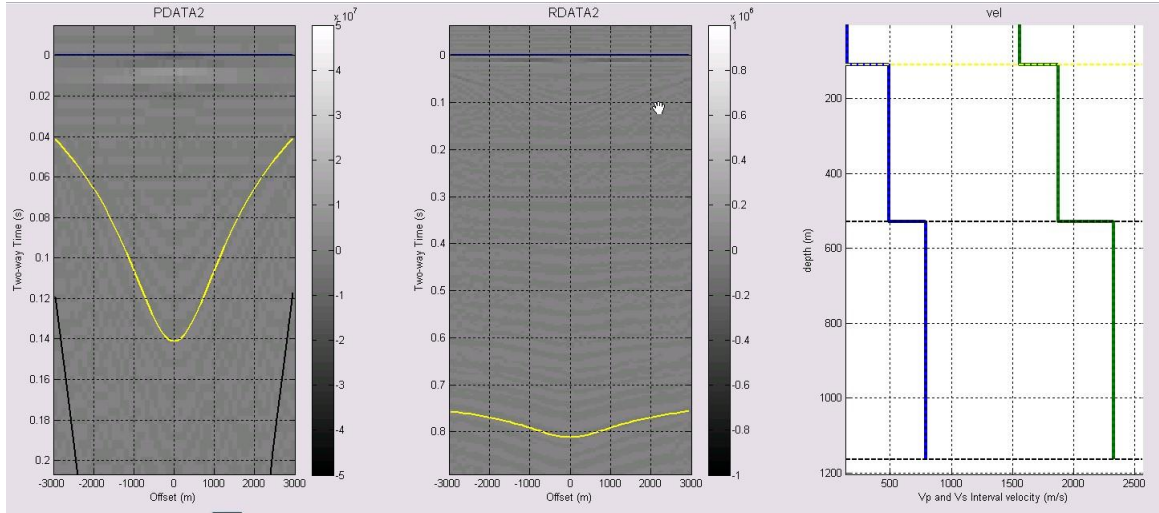


Figure 3.7: The reflection 2-way time on the PP gather and PS gather section is derived from the section above. The two-way time estimates have been used to calculate Vs value from Vp derived from dynamic correction from the section in the Figure3.2. 750ms used in the calculation above is the travel-time of the PS wave, calculated from the difference between the PS reflection time (820ms) shown by the yellow line of the middle panel and the travel-time of the down-going P-wave leg of the travel-time (0.5x140ms) of the first panel.

### 3.3.2 Estimating interval Vp and Vs from dynamic corrections

Then, we estimate interval Vp and Vs from dynamic corrections using the technique of ray tracing for flattening events in a flat-layered earth (Figure 3.8), and determine reflection points with depth. Using the approach described above shallow sea floor registration (Backus et al., 2005) to numerically estimate the arrival times of reflections on selected locations on the common-receiver gathers. The dynamic moveout analysis is carried out, to estimate the velocities that best flatten the events on each horizon on the selected locations shown (Figure 3.9). The dynamic moveout correction

was done horizon by horizon as shown in Figure 3.8 for both the PP and the PS common receiver gathers. At the far offset, it is believed that the effect of hyperbolic moveout is reduced and more emphasis is on finding the velocity that flattens the near traces to  $t_0$ . Once achieved and the events on that horizon are flat, this velocity is stored and the next horizon is selected. For each location and each horizon corrected, the  $V_p/V_s$  values are calculated and displayed on the far right panel in Figure 3.10 using the formulae below (Backus et al., 2005).

$$\frac{V_p}{V_s} = 2 \frac{\Delta T_{PS}}{\Delta T_{PP}} - 1$$

After velocity analysis has been carried out on the entire receiver line (Figure 3.9), the velocities checked (Figure 3.10), then the interval  $V_p$  and  $V_s$  estimated velocity models (Figure 3.11) are created. Linear interpolation is used to fill the velocity values between selected and picked locations. Figure 3.11 appears blocky because linear interpolation has not been applied at this time to the estimated velocity field.

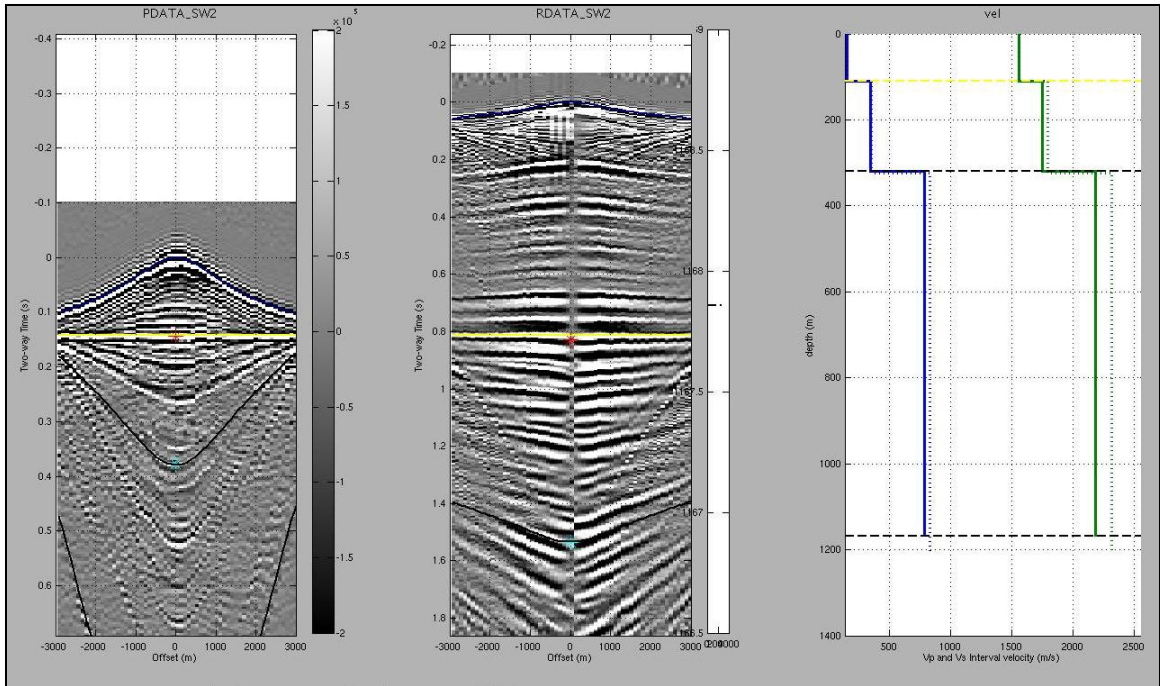


Figure 3.8: Dynamic velocity analysis was carried out one horizon at a time. The software allows velocity values to be overlain on the gather display and the yellow line is the interval velocity that flattens the first horizon. This analysis is carried out horizon by horizon as shown above. The velocity at the horizon highlighted in yellow is too fast for the horizon above it, the reason being, there is a bulge in the horizon above but too slow for horizons below, the reason for the bulge below the horizon highlighted in yellow.

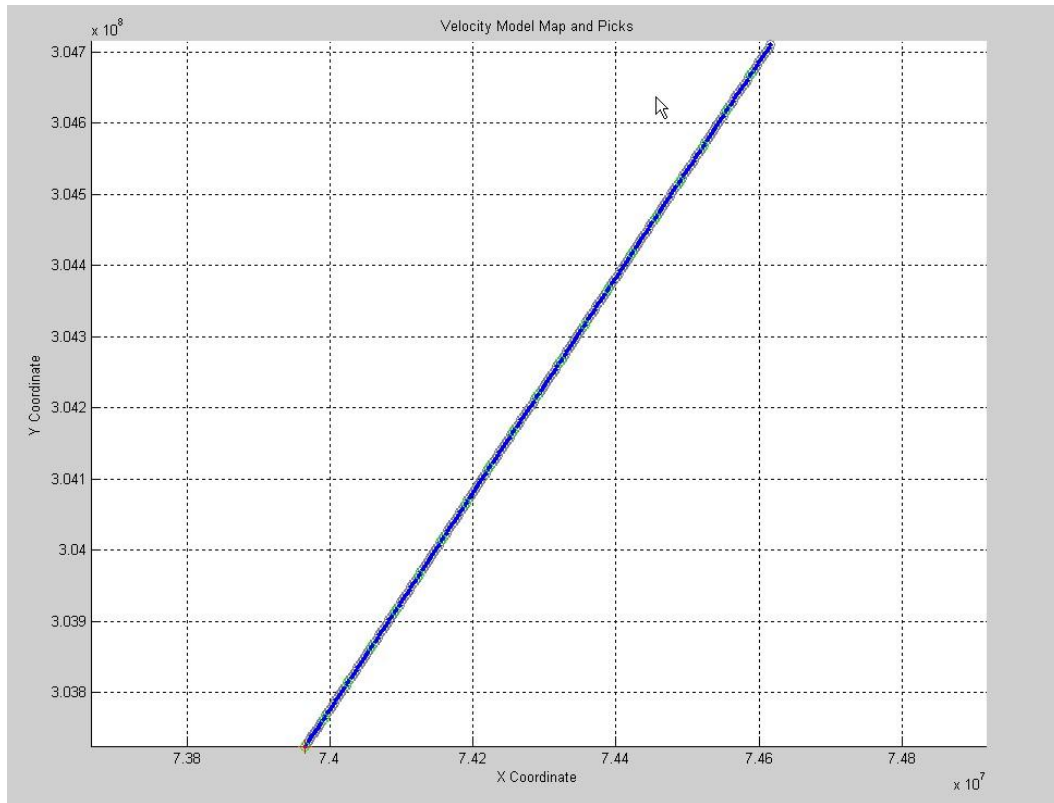


Figure 3.9: The receiver line used for the velocity analysis in this study.

### 3.4 Assumptions in the ray-based technique

In this study, the  $V_p$  and  $V_s$  interval velocity model is built from layered velocity compartments separated by picked horizons from a receiver stack section (Figure 3.4), and the purpose is to estimate shallow velocities ( $V_p$  and  $V_s$ ) by using a local 1.5d ray-tracing using common receiver gathers with water bottom reduced time in a joint mode PP and PS velocity analysis. The water bottom reduced time is used to account for the differences in source and receiver depths, and it's assumed that this removes the effect of the hyperbolic moveout when ray-tracing is carried out to flatten the common receiver gathers.

Another assumption is that if the depth equivalent of PP and PS reflection events on stacked images can be identified, then their reflection events can be identified on the gathers that produced the stacked sections. Although DeAngelo et al., (2008) point out that this might not always be true, stating the expectation is to be able to locate their casual reflection events on common-receiver gathers. With large differences in elevation of source and receivers, that normal moveout does not apply (DeAngelo et al, 2008). It is assumed that ray-tracing is not constrained by the above statement.

The EGL software developed at the University of Texas is not computationally intensive. This analysis could be done interactively and traveltimes curves could be overlain on the common-receiver gathers as shown on Figures 3.3, 3.8 and 3.10. Time shifts can be applied to flatten actual reflections, one horizon at a time (Figure 3.8). DeAngelo et al., (2008) suggest that the latter is more accurate and simpler because it eliminates the stretch artifacts and allows much longer offset constrain velocities. Stretch artifacts are not seen on the PS common receiver gathers (Figure 3.10) but are on the PP common receiver gathers, in some cases using the estimated PS traveltimes for an event and constraining the  $V_p/V_s$  values separately. Also using the intercept times at zero offset,  $V_p$  could be calculated. The stretch artifacts are only evident on the PP section because same shots cover more offset on the PP section than on the PS section for the same common receivers (Figure 3.1).

The top of the salt body clearly was a distinct geological structure used as the last horizon from PP and PS sections. The tops of the salt body were delineated more

accurately after the iteratively estimated shallow velocities were applied to the receiver gathers and stacked.

Spatial distribution of the velocity model of the velocity field could be viewed in the velocity model volume plot in figure 3.11. For this study, this has not been smoothed at this time and appears blockish. There would be a linear interpolation, applied to smooth out the volume. Although this process is labor intensive, it requires similar time and effort as conventional velocity analysis techniques and attempts are still ongoing to further constrain the data. Further iterations of the process described above would be carried out and a more robust velocity profile of the  $V_p$  and  $V_s$  shallow velocities produced.

### **3.5 Limitations and challenges in using the ray-tracing technique**

This approach applied in this study using the ray-based technique and the EGL tool seems good for shallow data only; more iterations and modification could still reveal more details below the salt.

There were QC challenges for depth registration of near sea floor equivalent seismic events in PP and PS modes. Identifying structural and stratigraphic interpretation constraints were some of the limitations in defining these depth equivalents of PP and PS reflection events. In this study, the identifiable structure is the top of the salt and is represented by horizon 3 on Figure 3.4. Other limitations were the amplitude, phase and frequency when correlating the PP and PS modes.

The process was carried out in a 2D sense, ignoring anisotropy and out-of-plane effects. The reason further study is being carried out using the anisotropy-based technique is to estimate a more robust velocity model field that is geologically representative and considers the effects of anisotropy in the area studied.

Good well ties for structural markers from well data are important to constrain the proper horizon layers. Unfortunately, for this study I have not been able to access any well data from this area.

### **3.6 Results from the ray-tracing technique**

The key implementations using the ray-based technique in this study are applying a ray-based processing flow to produce shallow PP and PS interval velocity model of the deepwater area of the Gulf of Mexico along a 2D profile. Using the Ray-tracing technique to constrain PP and PS image interpretations and creating an iterative process where combined with an interactive velocity analysis, velocity models that are more robust could be achieved.

The shallow velocity values estimated from the first horizon in the shallow for  $V_p$  is 1560m/s and 147m/s for  $V_s$ . Three horizons were chosen for this study; the  $V_p/V_s$  values range from above 10 in the shallow horizon layer to less than 4 in deep horizon layer using this technique.

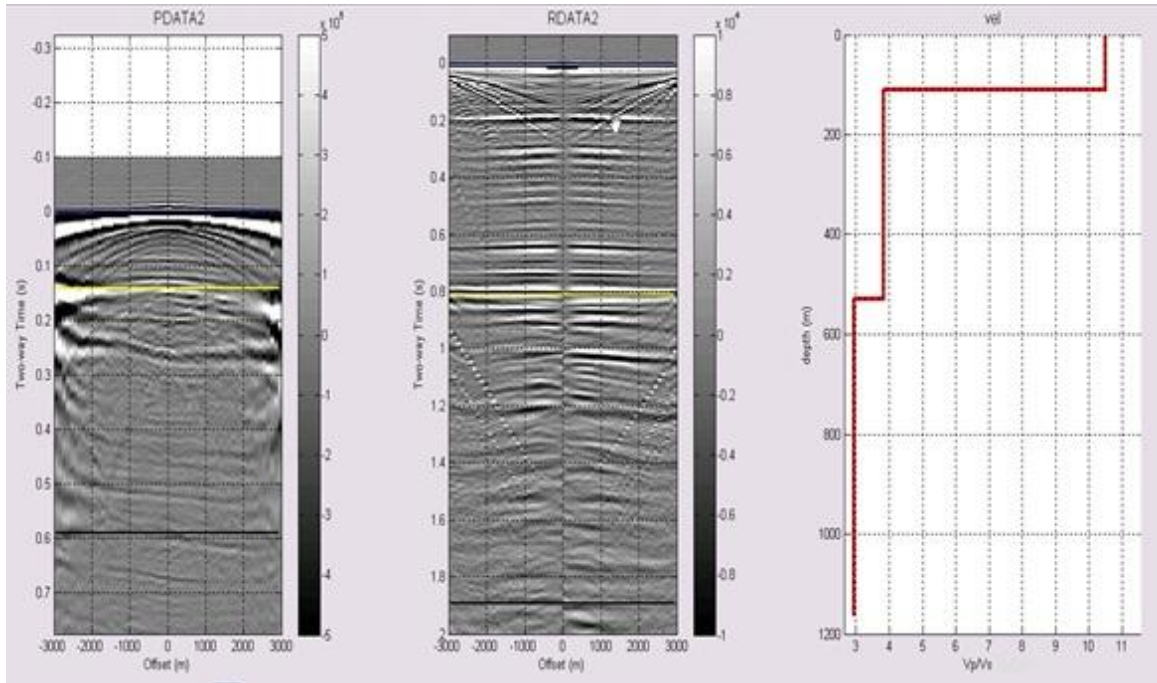


Figure 3.10: The PP and PS common receiver gathers show the applied interval velocities with the  $V_p/V_s$  values for the 3 horizons.

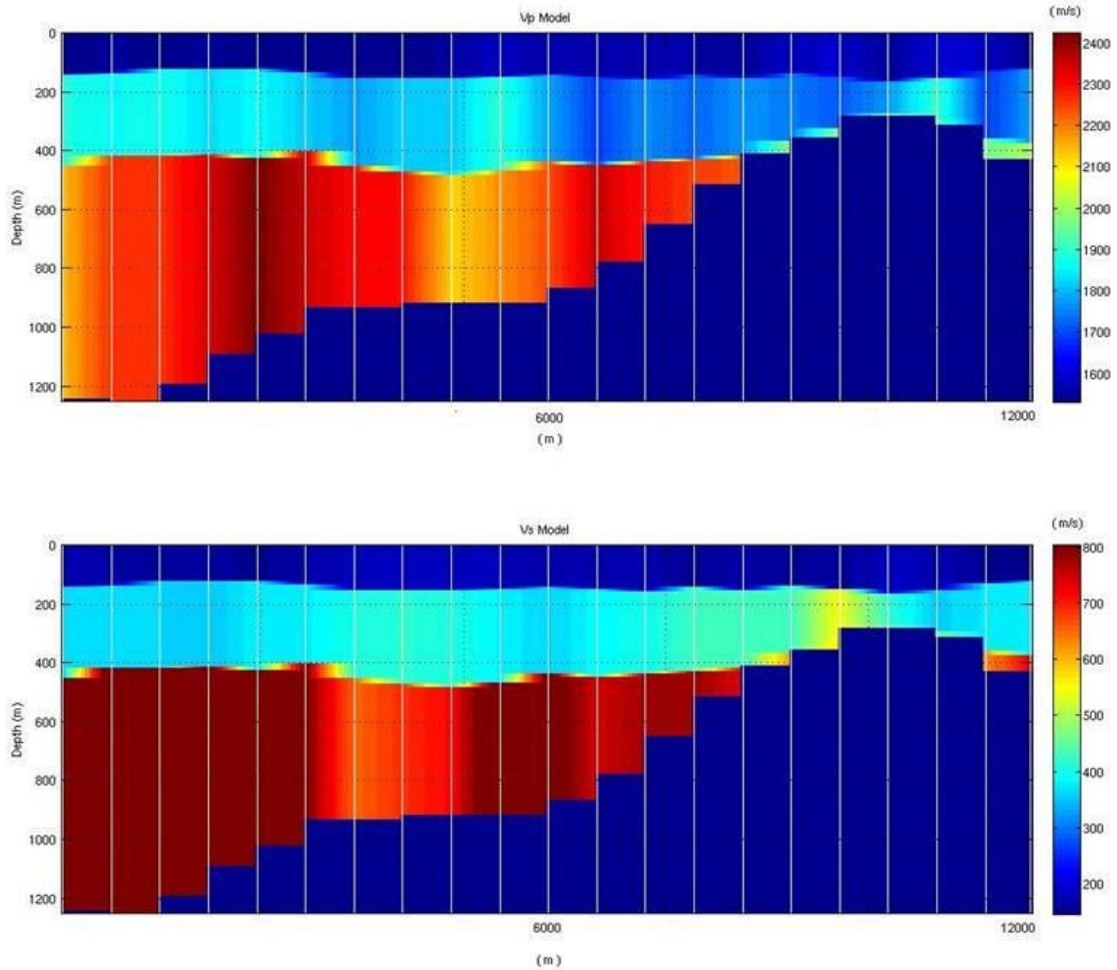


Figure 3.11: The generated  $V_p$ - and  $V_s$ -interval velocity models along the 2d receiver line profile.

### 3.7 Synthetic model generation

Also, this study seeks to demonstrate the use of ray-tracing in building a synthetic model the segy format of the radial 2D receiver line stack from the study area. This is done using the earlier estimated PS velocities from the ray-tracing technique and for quality control purpose. PS and PP data seismic acquisition designs are similar, and the PS stack used did reveal the horizons in the shallow (Figure 3.4).

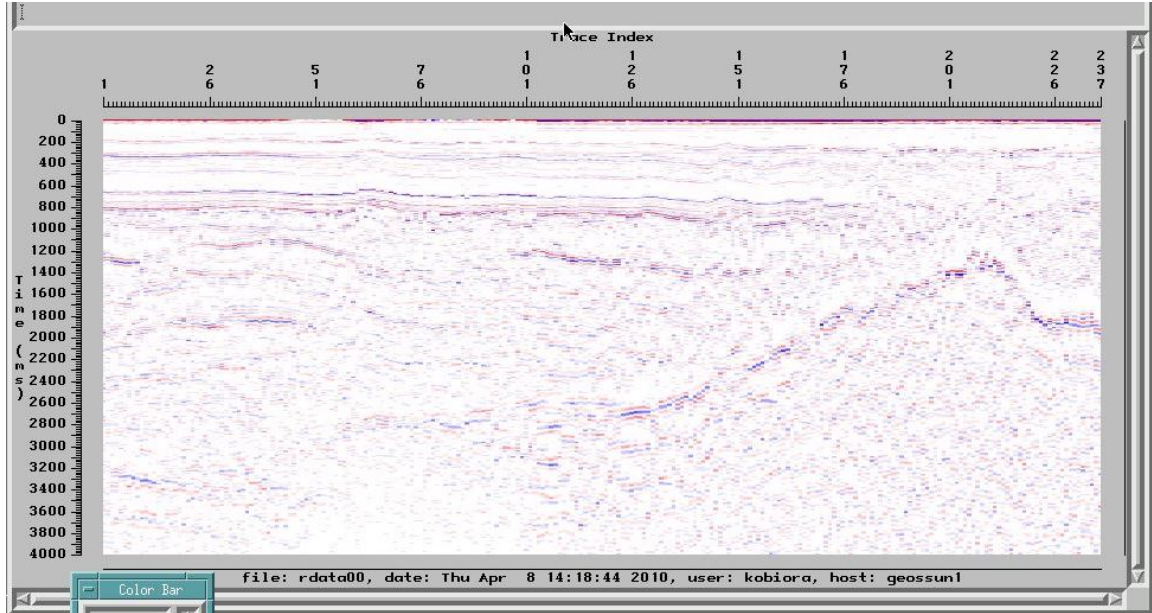


Figure 3.12: PS receiver line stack generated using the estimated velocity from ray tracing.

Three horizons that include the top of salt were selected and inserted (Figure 3.13). Also inserted were material properties like velocities, and densities to the layers selected for the purpose of ray-tracing as shown in Figure 3.14. Ray-tracing is the tool in the first analysis technique in this study. Initial  $V_p$  and  $V_{ps}$  estimates using the ray-tracing technique has been used for generating synthetic dataset that is described below.

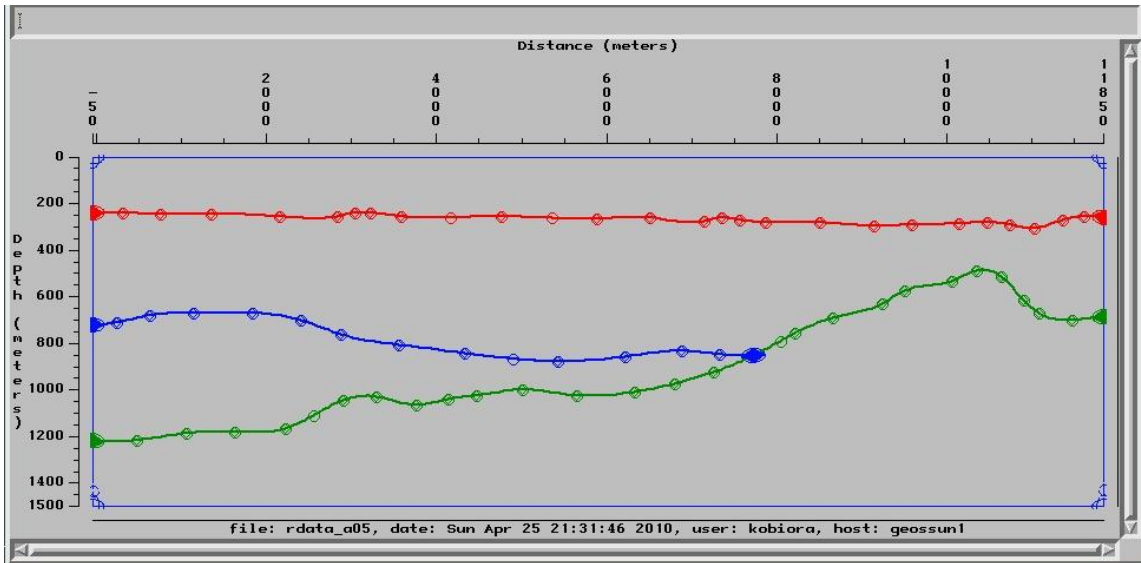


Figure 3.13: Three selected horizons, including the top of salt

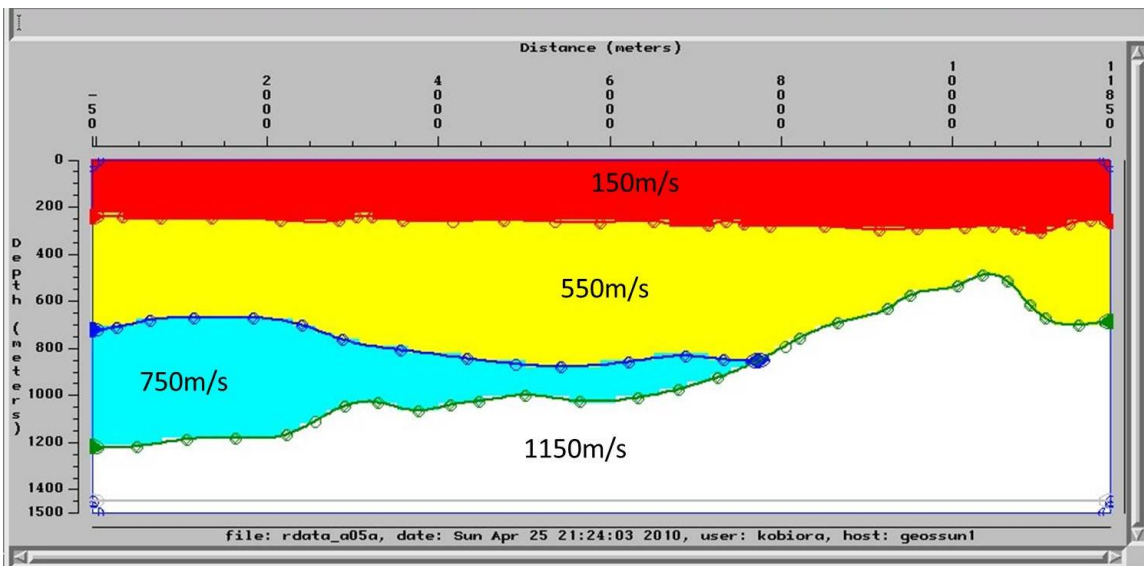


Figure 3.14: Velocities and other material properties assigned to three layers

The shot and receiver spacing,  $V_p$  and  $V_s$ , densities, and acoustic impedance, were used with ray-tracing to generate synthetic shot gathers. Then using the zero-offset

geometry, a time-migrated stack section to compare with my original stack section was generated.

After ray-tracing, the pressure rays (PP) travel times were captured using pressure phones and an omni-directional source from the three horizons that include the top of salt at this initial stage in the study as shown in Figure 3.13.

In the trace generation, the parameters depend on the material properties assigned to the various horizons (Figure 3.14). Using the ray-tracing technique, the initial shallow velocity values estimated from the first horizon in the shallow are 1560m/s for  $V_p$  and 147m/s for  $V_s$  as shown in Figure 3.15. Three horizons were chosen for this study; the  $V_p/V_s$  ratios range from above 10 in the shallow to less than 4 in deep from initial results. The software used to estimate these velocities uses the ray-tracing technique to estimate the travel times from the receiver gathers and uses these times to manually invert to get the velocities ( $V_p$  and  $V_s$ ) that flatten equivalent horizons from the gathers from the two modes. The density values for the various horizons with estimated  $V_p/V_s$  values, and the velocities in the horizons, are used to determine the travel times of the ray paths. The difference in the material properties between the various horizons results in the change in acoustic impedance and the reflections registered on a seismic trace. Changes in acoustic impedance also affect the reflection and transmission strength. There would be no reflection where there is no change in acoustic impedance.

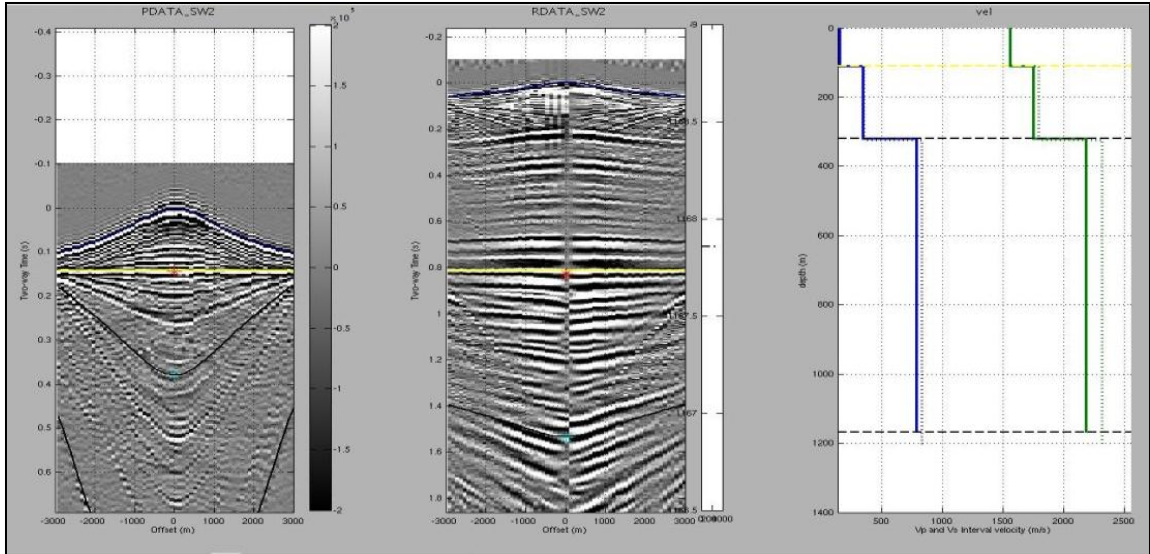


Figure 3.15:  $V_p$  (green) and  $V_s$  (blue) estimated for the various layers assuming equivalent horizons in the two modes.

The software calculates the reflection and transmission coefficient using Knott-Zoeppritz equations. There are options to include loss from spreading in amplitude calculation to make the data resemble real seismic data and also to make the synthetic data look more like spikes, as shown in Figure 3.16.

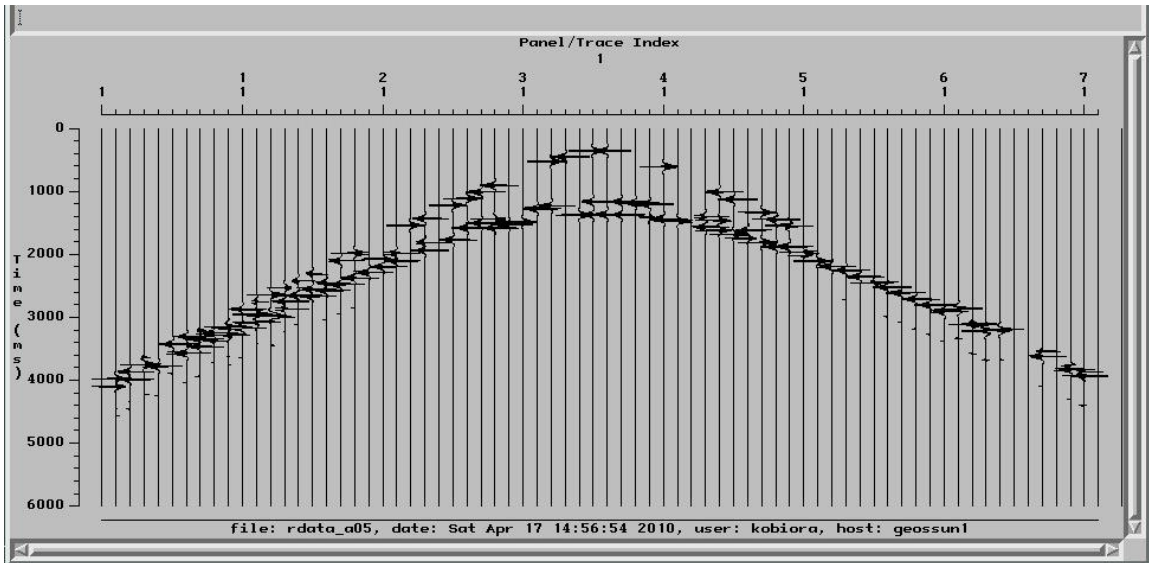


Figure 3.16: Generated synthetic shot gather from the estimated traveltimes.

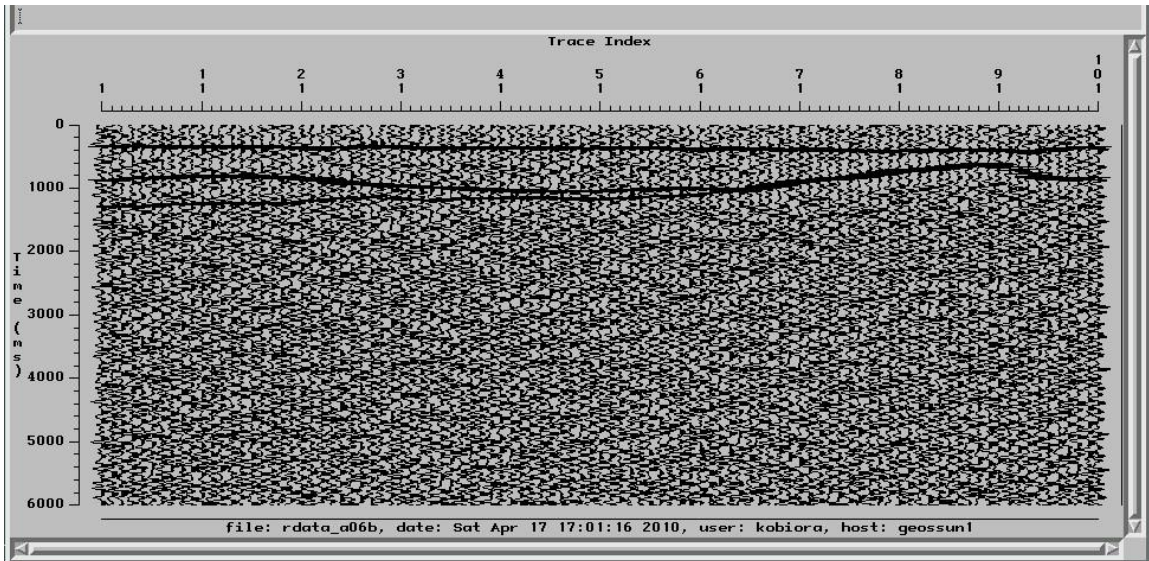


Figure 3.17: Synthetic stack with -20dB noise level.

Then the traces were convolved with a Ricker wavelet that has similar bandwidth and phase to the seismic data. The peak frequency of the wavelet was set to 25Hz and the phase also changed to minimum phase. As shown in Figure 3.17, a -20 dB level of noise was added to the data and then the generated synthetic traces were output to Segy to compare with the actual data (Figure 3.18).

Part of the initial process involves inverse modeling (the inversion of travel times to generate a depth section), and the final process is a forward modeling process to create synthetic seismic section to compare with the final interpreted data after estimating and applying the anisotropy parameters. The results are used to match the original interpretation, and more adjustments would be then made to the parameters and the entire process iterated.

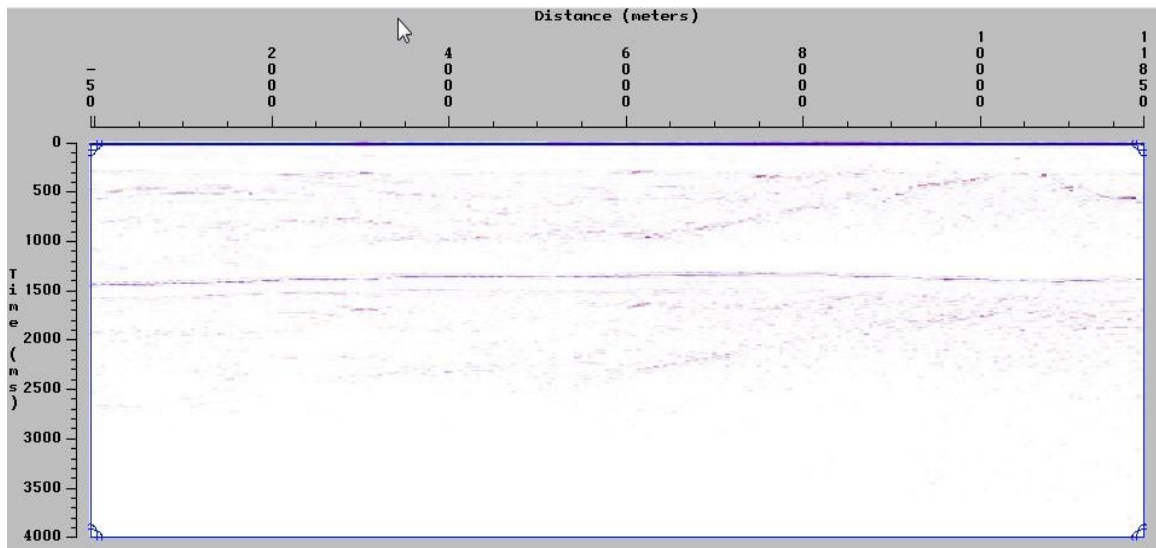


Figure 3.18: PP stack generated using 1500m/s constant velocity.

The synthetic trace generating process like the one described in the ray-tracing technique assumes there is no lateral velocity change or anisotropy, and this assumption affects the travel times and the synthetic traces generated. But this study tries to account for lateral velocity change or anisotropy as accurately as possible to represent the true synthetic traces from that area.

## **Chapter 4: The Anisotropic Velocity Model Building Technique**

### **4.1 Introduction**

The second velocity model building technique used in this study for building the PS-wave velocities is the anisotropic velocity model building technique. Part of this second technique involves the use of the four-parameter theory by Li and Yuan (2003) for vertical transverse isotropy (VTI). The four parameters include PS stacking velocity ( $V_{C2}$ ), the vertical velocity ratio ( $\gamma_0$ ), the effective velocity ratio ( $\gamma_{\text{eff}}$ ), and the anisotropy parameter ( $\chi$ ). These parameters could be derived from the different moveout information from different offsets that give the best aligned event for the stack. After estimating the stacking velocity from the near offsets of PP- and PS-wave gathers, the vertical velocity ratio from correlating the PP- and PS-wave stack sections, and the effective velocity from the mid offsets of the PS-wave gathers, these parameters are used in pre-stack time migration (PSTM) to generate common image point (CIP) gathers. The final steps include residual moveout analysis on the CIP gathers to estimate the anisotropy parameter from the far offsets. This entire process requires a normal moveout (NMO) run and several iterations of pre-stack time migration imaging (PSTM).

### **4.2 The anisotropic velocities and travel times**

The arrival time for PS-wave seismic data is non-hyperbolic, even for an isotropic layer as shown below (Figure 4. 1).

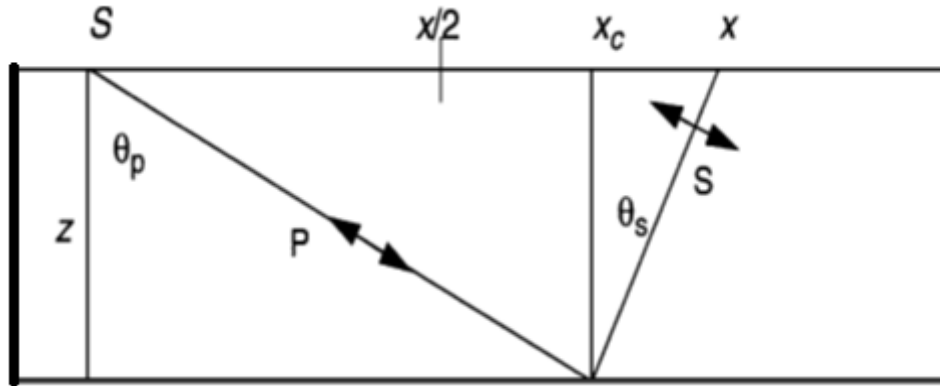


Figure 4.1: The single layer representation of the PS-wave arrival time (after Thomsen,1999)

The travel-times could be represented as shown from using trigonometry:

$$t_c = t_p(x) + t_s(x) = \frac{z}{V_p \cos \theta_p(x)} + \frac{z}{V_s \cos \theta_s(x)}, \quad (4.1)$$

where  $t_p$  is P-wave leg of the one way travel-time and  $t_s$  is the S-wave leg of the one-way travel times. The offset  $x$  is represented by;

$$x = V_p t_p \sin \theta_p + V_s t_s \sin \theta_s = p V_p^2 t_p + p V_s^2 t_s.$$

(4.2)

Thomsen (1999) indicates that the analysis would need more approximations for more complicated cases. Tsvankin and Thomsen (1994) expanded the equation above as a Taylor series ( $t^2$  versus  $x^2$ ).

$$t_c^2(x) = t_{c0}^2 + \frac{x^2}{V_c^2} + A_4 x^4 + \dots \quad (4.3)$$

Further considering the two-way PS-wave zero-offset time  $t_{c0}$ , which in this context is the vertical travel-time for the PS-wave used in the relationship for the one-way pure mode times as shown;

$$t_{c0} = t_{p0} + t_{s0} = t_{p0} \left( 1 + \frac{t_{s0}}{t_{p0}} \right) = t_{p0}(1 + \gamma), \quad (4.4)$$

since

$$\gamma = \frac{V_p}{V_s} = \frac{z/t_{p0}}{z/t_{s0}} = t_{s0}/t_{p0}.$$

Aki and Richards (1980) demonstrated that the PS amplitude energy in the vertical direction for horizontal media is zero, but  $t_{c0}$  could still be found by comparing the  $t_{p0}$  from PP-wave and the  $t_{c0}$  from PS-wave stacks. This is achieved by interpretation of the PP-wave and PS-wave arrival-times using the two stacks.

The PS-wave moveout signature for horizontal layered VTI media was further expanded by Tsvankin and Thomsen (1994),

$$t_c^2 = t_{c0}^2 + \frac{x^2}{V_{C2}^2} + \frac{A_4 x^4}{1 + A_5 x^2}. \quad (4.5)$$

Li and Yuan (2003) modified it to where:

$$A_4 = -\frac{(\gamma_0 \gamma_{eff} - 1) + 8(1 + \gamma_0) \chi_{eff}}{4t_{c0}^2 V_{C2}^4 \gamma_0 (1 + \gamma_{eff})^2}, \quad A_5 = \frac{A_4 V_{C2}^2 (1 + \gamma_0) \gamma_{eff} [(\gamma_0 - 1) \gamma_{eff}^2 + 2 \chi_{eff}]}{(\gamma_0 - 1) \gamma_{eff}^2 (1 - \gamma_0 \gamma_{eff}) - 2(1 + \gamma_0) \gamma_{eff} \chi_{eff}}, \quad (4.6)$$

and

$$\gamma_{eff} = \frac{\gamma_2^2}{\gamma_0}; \quad \gamma_2 = \frac{V_{p2}}{V_{s2}}.$$

From above and equation 4.4,

$$V_{P2}^2 = V_{C2}^2 \frac{\gamma_{eff}(1 + \gamma_0)}{1 + \gamma_{eff}}, \quad V_{S2}^2 = V_{C2}^2 \frac{(1 + \gamma_0)}{\gamma_0(1 + \gamma_{eff})}. \quad (4.7)$$

Equation (4.6) contains the four parameters that Li and Yuan (2003) refer to as the PS-wave stacking velocity model.  $V_{C2}$  is the PS-wave stacking velocity,  $\gamma_0$  and  $\gamma_{\text{eff}}$  are the vertical and effective velocity ratio, and  $\chi_{\text{eff}}$  is the PS-wave anisotropic coefficient. These parameters can be estimated at various offset-to-depth ratios from the binned gathers.  $V_{C2}$  could be estimated from hyperbolic moveout at the near offsets ( $x/z < 1.0$ ),  $\gamma_{\text{eff}}$  could be estimated from the intermediate offsets ( $x/z < 1.5$ ), and  $\chi_{\text{eff}}$  could be estimated from the far offsets ( $x/z < 2.0$ ). According to Li and Yuan (2003), equations (4.5) and (4.6) are accurate for offset-depth ratio up to 2.0 ( $x/z < 2.0$ ). My expectation is to compare the estimated velocities using the isotropic ray-based techniques to the ones that would be produced from using the equations described above and other equations from this second technique. Then estimate the migration velocity from the stacking velocity model, generate common imaging point (CIP) gathers using PSTM, and apply residual moveout to the CIP gathers.

### **4.3 Vertical transverse anisotropy**

There are thin beddings of sedimentary layers over the shallow salt body in the area of study which could cause vertical transverse anisotropy (VTI or polar anisotropy). VTI effects are assumed for this area which makes convectional isotropic methods not appropriate for this area and the need for other methods. Also this is due to non-symmetric ray-path of converted wave and the non-hyperbolic moveout that as a result

makes flattening using conventional isotropic methods not flatten the gathers. This means that the PS-wave seismic traces cannot be grouped into common mid-point (CMP) gathers and requires a new conversion point binning.

#### **4.4 Asymptotic conversion point (ACP)**

Tessmer and Behle (1988), Zhang (1992), and Harrison (1992) devoted effort trying to solve for conversion points. They earlier developed a technique that involves PS-wave NMO and common conversion point (CCP) binning which is not successful in the presence of anisotropy. Other attempts to achieve success in this area made using anisotropic CCP binning and PS-wave DMO by Tsvankin and Grechka, (2000) and others, who failed because it was strongly a velocity dependent process. Efforts have been made to replace the CCP binning and DMO approach by Dai (2003), Dai and Li (2001); among others, and the end result is the asymptotic conversion point discussed and used in this study.

##### **4.4.1 Single layer**

The simple case condition was described in the Figure 4.1 above. Using the principles of trigonometry, the source-receiver offset of the PS-wave conversion point could be expressed as

$$x_c = V_p t_p \sin \theta_p = p V_p^2 t_p. \quad (4.7)$$

Comparing the equation above to equation (4.2), the expression could be represented as a fraction of the total offset and exactly according to Thomsen (1999):

$$\frac{x_c}{x} = \frac{1}{1+V_s^2 t_s / (V_p^2 t_p)} = \frac{1}{1+t_s(x)/\gamma^2 t_p(x)}. \quad (4.8)$$

Also, the asymptotic limit of vertical travel is used instead of the one-way  $t_p$  and  $t_s$  travel-times as a function of the total offset ( $x$ ). The asymptotic limit uses the values of the offset divided by depth ( $x/z$ ) and represented with this expression:

$$t_s(x)/t_p(x) \rightarrow t_{s0}/t_{p0} = V_p/V_s = \gamma.$$

Tessmer and Behle, (1998) express the asymptotic conversion point (ACP) for a simple case condition as shown:.

$$x_{c0} = \frac{x\gamma}{1+\gamma} \quad (4.9)$$

Tessmer and Behle (1988) did estimate an exact value of  $\gamma = 2$  for the equation above for a special case and with schematic diagram that showed the relationship as it converts from PS-wave at various points ( $x_c, z$ ). The diagram in Figure 4.2 shows the PP-wave travel times line for the energy that did not convert to PS-wave. Also shown is the asymptotic conversion line (ACP  $x_{c0}$ ). The actual asymptotic conversion points at closer  $x/z$  to the receiver vary from this (Figure 4.2). This is significant because most targets in most surveys are assumed to be at  $x/z = 1$  according to Thomsen (1999). Also, in common practice one could regard the solution of the equation as a function of  $x/z$ , this time with  $z$  fixed, concentrating on a single event or location and offset ( $x$ ) varied from minimum to maximum.

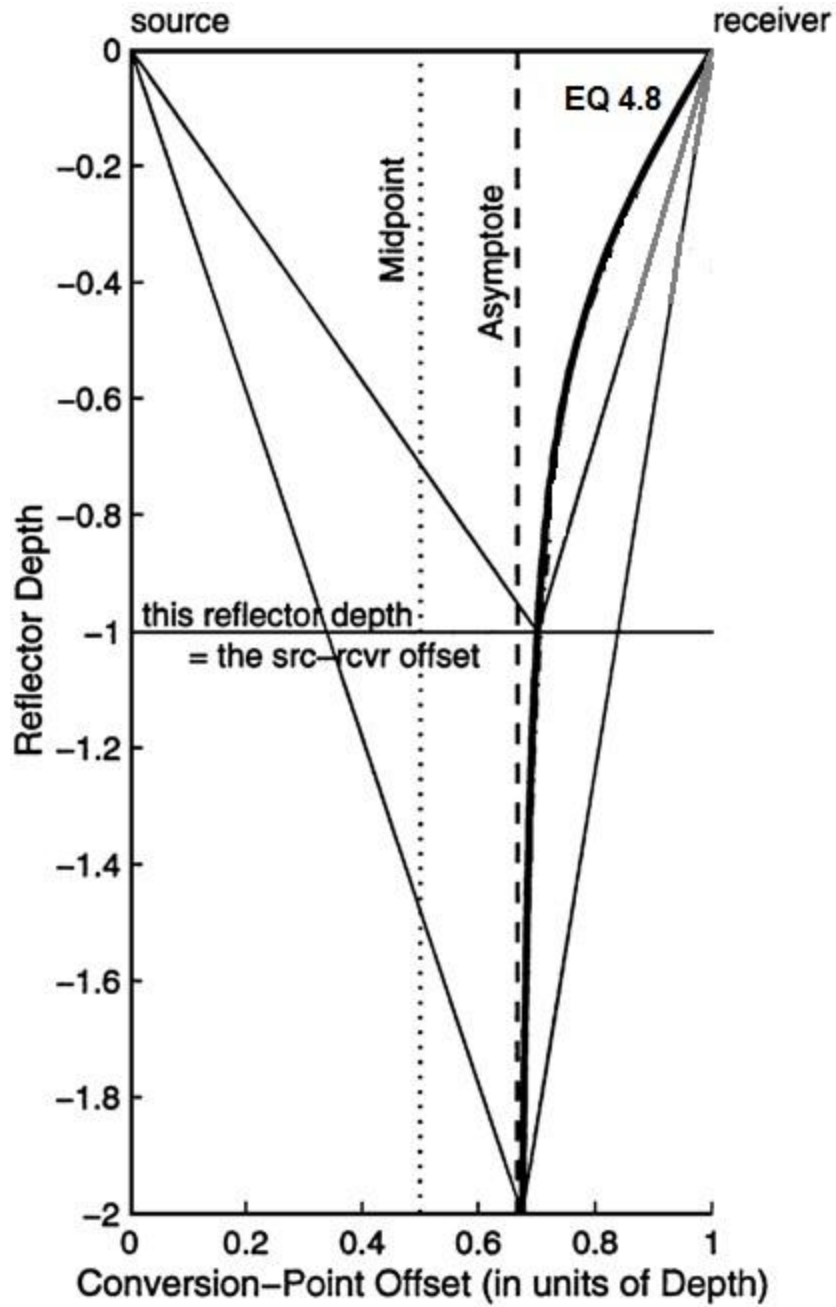


Figure 4.2: A source-receiver offset conversion point for a single trace with  $\gamma = 2$  with equation 4.8 in depth equivalent (after Tessmer and Behle, 1998).

#### 4.4.2 Multiple layers

In the case of multiple layer conditions, Thomsen (1999) distinguished between the vertical velocity ratios functions used in the expression for the ACP binning.

$$\gamma_0 \equiv \frac{V_p}{V_s} = \frac{t_{s0}}{t_{p0}}; \quad V_p(z) = z/t_{p0}(z) \quad \text{and} \quad V_s(z) = z/t_{s0}(z) \quad (4.10)$$

The velocity ratio for the moveout velocity function in the short-spread (RMS) is expressed by:

$$\gamma_2 \equiv \frac{V_{p2}}{V_{s2}}, \quad (4.11)$$

where the P-wave moveout from the near offset is represented by  $V_{p2}$  and assuming the S-wave moveout from the equivalent near offset is represented by  $V_{s2}$ . Using the moveout equation 4.5 earlier, the parameters referred to are  $V_{c2}$  and  $A_4$  as described by Tsvankin and Thomsen (1994) in the P-wave context i.e. by the flattening procedure. Thomsen (1999) generalized the PS-wave vertical travel-time to

$$t_{c0} = t_{p0} + t_{s0} = t_{p0}(1 + \gamma_0), \quad (4.12)$$

and at every  $t_{c0}$

$$V_{c2}^2(t_{c0}) = \frac{V_{p2}^2}{1+\gamma_0} + \frac{V_{s2}^2}{1+1/\gamma_0} = \frac{V_{p2}^2}{1+\gamma_0} \left( 1 + \frac{1}{\gamma_{eff}} \right), \quad (4.13)$$

where

$$\gamma_{eff} = \gamma_2^2/\gamma_0. \quad (4.14)$$

To demonstrate the validity of equations described above, described below is an example from Thomson (1997) where the vertical velocities were inferred for  $\gamma_0 = 2.9$

and  $\gamma_2 = 2.4$ , results which is used to estimate  $\gamma_{eff} = 2.0$ . The ACP  $x_{c0}$  was calculated using all three values to illustrate how significant the difference in estimate could be. The results using the  $\gamma_0 = 2.9$ ,  $\gamma_2 = 2.4$ , and  $\gamma_{eff} = 2.0$  respectively were 0.74, 0.70, and 0.66, which is quite significant and could amount to hundreds of offset in difference.

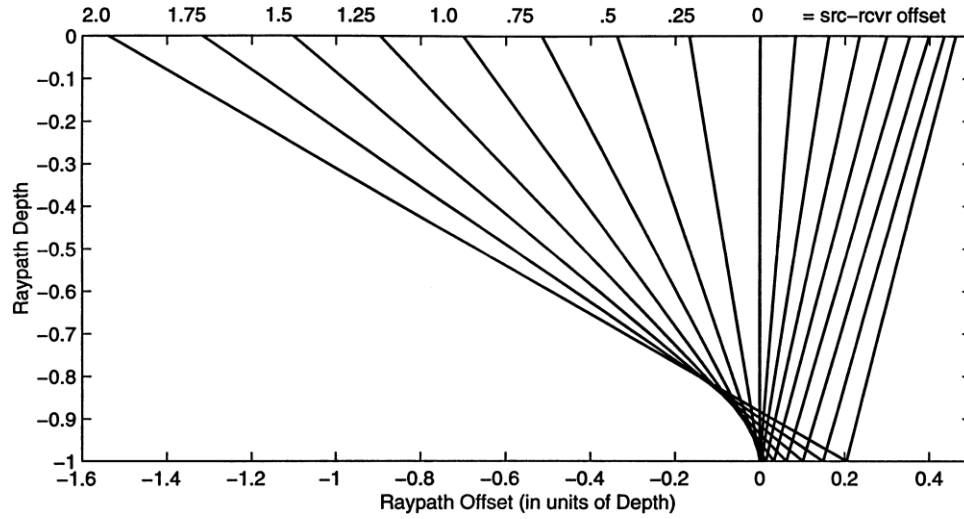


Figure 4.3: A display of a reflection event from an ACP binned gather (Thomsen, 1999)

#### 4.5 The PSTM velocity model theory

To construct the PSTM velocity model from the stacking velocity model estimated during seismic data processing, equation (4.15) below was used. The links between the anisotropic parameters as discussed by Dai and Li (2001) are based on a layer stripping process to obtain  $\eta$  and  $\zeta$  from  $\chi$ . But Alkhalifah and Tsavankin (1995), found that empirical relationships using a single-layer case may work better for time processing:

$$\eta_{eff} = \frac{x_{eff}}{(\gamma_0 - 1)\gamma_{eff}^2}; \zeta_{eff} = \frac{x_{eff}}{(\gamma_0 - 1)}, \quad (4.15)$$

since

$$x_{eff} = \eta_{eff} \gamma_{eff}^2 \gamma_0 - \zeta_{eff} ,$$

where  $\eta_{eff}$  the effective P-wave anisotropic coefficient was derived by Alkhalifah and Tsvankin, (1995) and  $\zeta_{eff}$  is the effective S-wave anisotropic coefficient (Li and Yuan, 2003).

Li and Yuan (2003) further used numerical analysis to evaluate the accuracy of the equation above using parameters in a five-layer model created by Thomsen (1986) in Table 1. They calculated the exact  $\eta_{eff}$  and  $\zeta_{eff}$ , calculated the exact  $\chi_{eff}$  using the equation described above, and recalculated the approximate  $\eta_{eff}$  and  $\zeta_{eff}$  using equation 4.15. The results were within the error margin of 2.0s, and this is attributed to the resolution of velocity analysis usually decreasing with time. Li and Yuan (2003) agree that the differences in  $\eta_{eff}$  and  $\zeta_{eff}$  are negligible on the calculation of travel-time. Therefore changing the value of  $\chi_{eff}$  could yield a value that fits the travel-time and the equation 4.15 is an appropriate empirical relationship for the purpose of estimating the anisotropic parameters.

The migration process involves the process of positioning and time-shifting. These two processes can be separated as the first process is less dependent on velocity and the moveout velocity applied could be reversed i.e. the time-shifting process could be reversed. This is the basis for the velocity update done in this study when the ACP binned gathers are converted to common image point gathers (CIP).

## 4.6 Processing flow

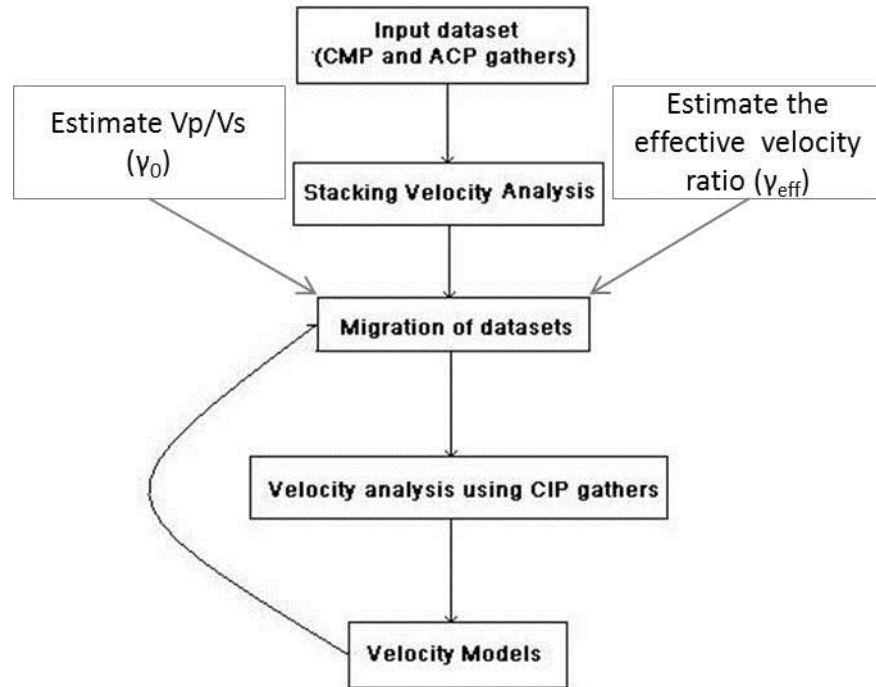


Figure 4.4: The processing flow for the anisotropic velocity model.

The processing flow (Figure 4.4) for this study requires two processes; a stacking process (NMO run) to estimate hyperbolic moveout in the short spread ( $V_{c2}$ ), the vertical velocity ratio ( $\gamma_0$ ) using the PP and PS stack sections, the non-hyperbolic moveout in the mid-

offset ( $\gamma_{eff}$ ), and iterations of pre-stack migration (PSTM) residual velocity update to estimate the anisotropy parameters.

#### **4.6.1 PP and PS stacks**

The stacking process involves summing the amplitude of the traces and dividing them by the number of traces. This is a data reduction process that relies on the signal being in phase and the noise being out of phase. It attenuates the random noise relative to the input record by up to the square root of the number of traces stacked and the coherent noise by a varying degree. This process for the PP and PS dataset are similar, requiring common mid-point (CMP) and asymptotic conversion point (ACP) gathers in the input. The ACP binning used in this process for sorting the PS seismic dataset was generated using the equation 4.9 discussed earlier. Also required is the application of moveout velocity from the short spread gathers of these datasets before stacking. The applied moveout velocity is the stacking (RMS) velocity estimated for PP- and the PS-wave short spread seismic data. Stacking the PS-wave seismic data sums the traces within the moveout corrected ACP binned gathers as in any conventional stacking process using CMP gathers from PP seismic dataset.

#### **4.6.2 Estimating the vertical velocity ratio ( $\gamma_0$ )**

The vertical velocity ratio is estimated from the PP- and PS-vertical times on stacks. The stacks were used in the absence of well information and were processed using

constant velocity estimates, and a couple of iterations are expected. The PP- and PS-wave stacks are generated by the process described above using promax software. Using a plugin to the promax software developed by Ion GX Technology required the stacks to be converted to sep format which interprets the seismic traces as binary for processing. Then correlating the travel-times from the two stacks generates a semblance for each trace location in the ACP binned gather (Figure 4.5). This semblance is generated using the equation 10 described above and trace by trace correlation to pick the semblance picks to estimate the correct time varying  $\gamma_0$  values that align the wave-fields in both the PP and PS stacks. This was done for all ACP binned locations along the 2D line in the area of study.

#### **4.6.3 Estimating the PP-wave normal moveout ( $V_{p2}$ ) at the near offset**

This is a conventional process of estimating the moveout velocity for the common mid-point (CMP) binned gathers using the promax software. The process generates a semblance analysis that estimates the best velocity that flattens the CMP binned gathers and would generate the best stack that lines the events in the PP-wave seismic section. The semblance is generated from super-gathers from the CMP binned gathers and the super-gathers are generated to minimize the effect of the acquisition design that leaves not enough traces in the near offsets.

#### **4.6.4 Estimating the PS-wave normal moveout ( $V_{c2}$ ) at the near offset**

$V_{c2}$  is the stacking (RMS) velocity which can be estimated from the near offset ( $x/z = 1$ ). This parameter is believed to control the moveout velocity at this offset according to Li and Yuan (2003). This moveout is believed to be hyperbolic and similar to the moveout in the short spread gathers of the PP seismic dataset (Thomsen 1999). To be able to apply the solution described in equation 4.5 above through semblance analysis, the data needed to be regularized offset to accurately represent the true stacking (RMS) velocity. Li and Yuan (2003) agree that the migration process can achieve this by spatially positioning the events correctly before further analysis to find the parameters that flatten the gather. So to achieve this, the data were first migrated using an assumed constant velocity of 1450m/s before converting to sep file format for  $V_{c2}$  parameter estimation through semblance analysis in the promax software plugin used. The plugin code was internally developed by Ion GX Technology and generates the semblance (Figure 4.6) from which the best picks that flatten the near offset gathers ( $x/z = 1$ ) were chosen in this process.

#### **4.6.5 Estimating the PS-wave normal moveout ( $\gamma_{eff}$ ) at the mid offset**

This parameter controls the moveout velocity at the intermediate offset and this moveout is non-hyperbolic due to the asymmetric ray-path which means that flipping the source and receiver positions would change the position of the seismic trace. Estimations from using equation 4.14 described above corrects and flattens the

events at the intermediate offset ( $x/z = 1.5$ ). The estimates of vertical velocity ratio ( $\gamma_0$ ), and the PS-wave stacking (RMS) velocity ( $V_{c2}$ ) are used in this iteration to generate the semblance for the analysis for  $\gamma_{eff}$  parameter estimation (Figure 4.7). This means that were used in the pre-stack time migration process to generate the gathers used in the semblance analysis for the  $\gamma_{eff}$  parameter estimation. The best picks that flatten the intermediate offsets ( $x/z = 1.5$ ) were chosen in this process.

#### **4.6.6 Estimating the PS-wave normal moveout ( $\chi_{eff}$ ) at the far offset**

At the far offset, the effects of anisotropy and asymmetry are accounted for by the  $\chi_{eff}$  parameter and correct the events at the far offsets ( $x/z = 2.0$ ). This parameter and the parameters estimated above were estimated using another plugin into promax software, written by Genmeng Chen for GX Technology. Also, the sep format was used with the equations described above to generate the semblance analysis which was picked to estimate the best values that flatten the gathers and the respective offsets targeted (Figure 4.8). The estimates of vertical velocity ratio ( $\gamma_0$ ), the PS wave stacking (RMS) velocity ( $V_{c2}$ ), and the  $\chi_{eff}$  are used in this iteration to generate the semblance for analysis and  $\chi_{eff}$  parameter estimation.

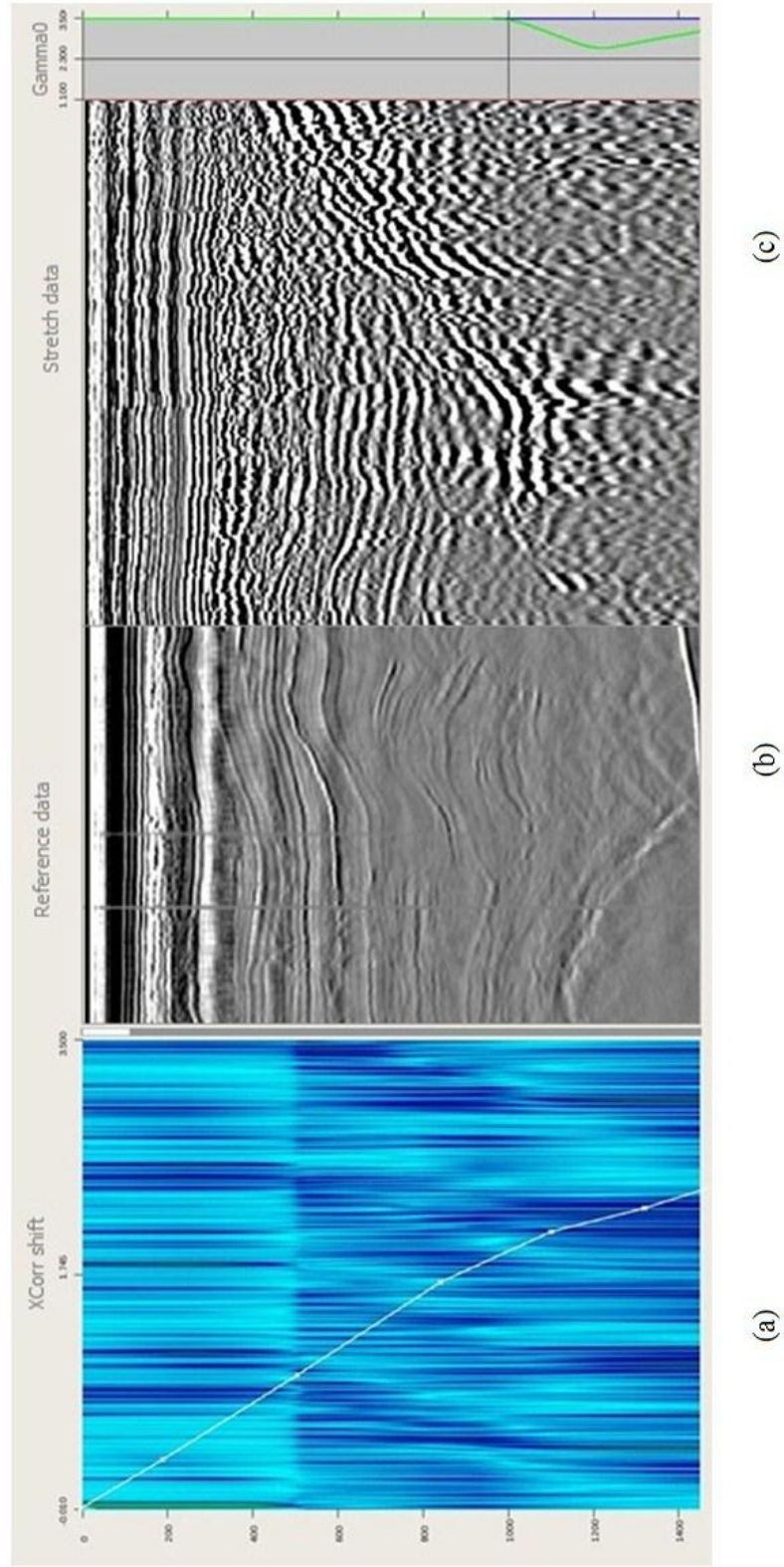


Figure 4.5: The semblance display for estimating the vertical velocity ratio ( $\gamma_0$ ) from the PP and PS stack sections. (a) The semblance display. (b) The PP stack section. (c) The PS stack section. The estimated  $V_p/V_s$  is 2.1 at the salt boundary.

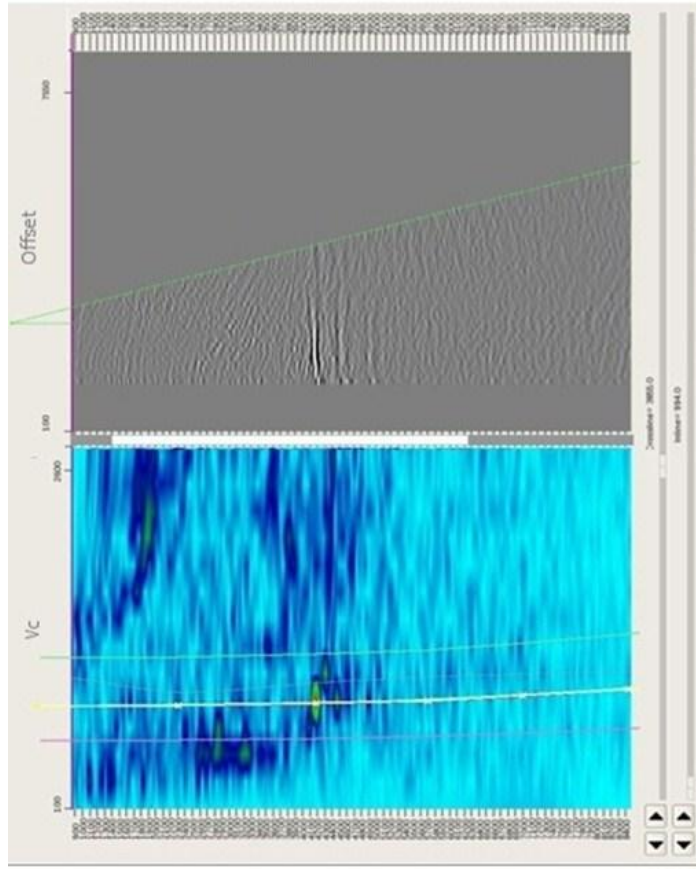


Figure 4.6: The semblance display (left side) for estimating the PS-wave normal moveout ( $V_{c2}$ ) from the near offset of the gather. The right side of display shows the effect on the gather.

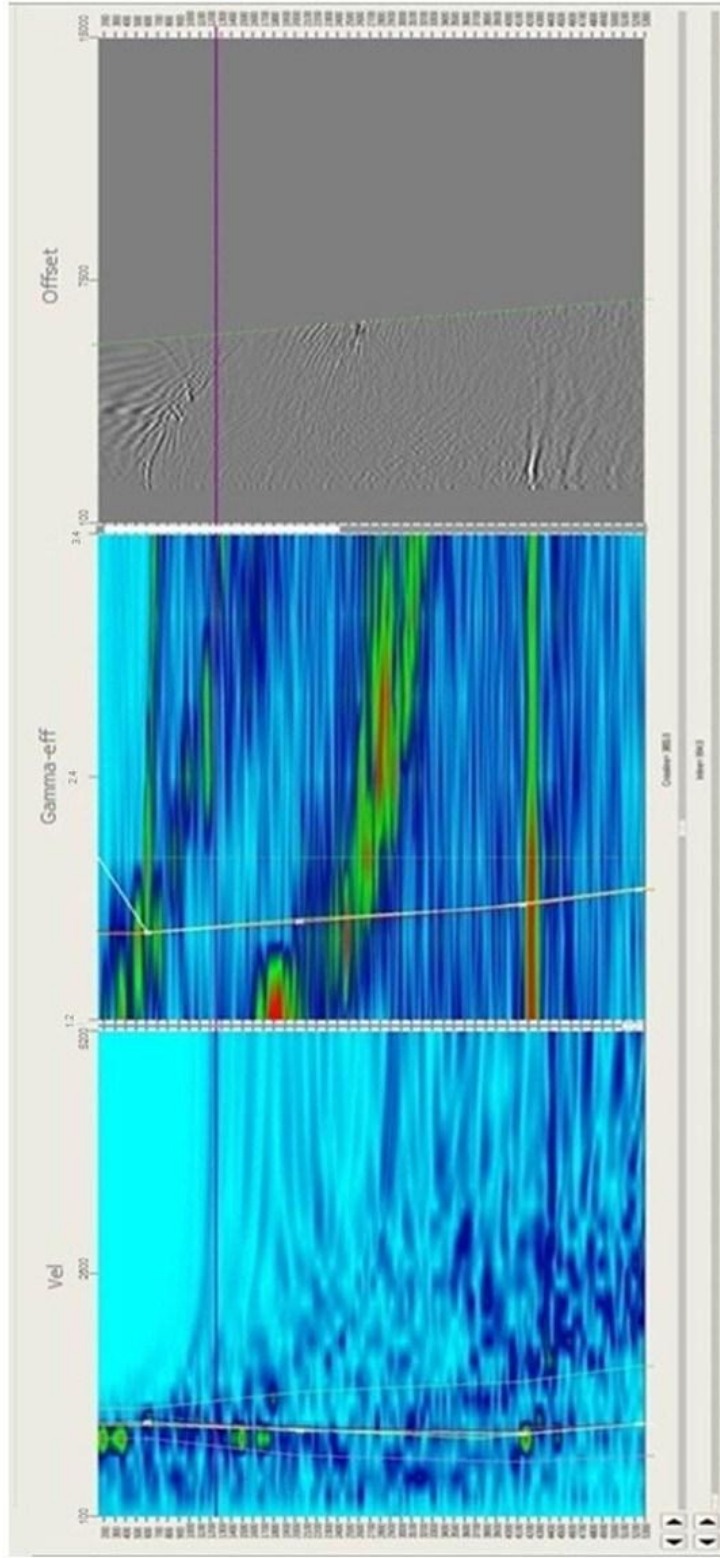


Figure 4.7: Estimating the PS-wave normal moveout ( $\gamma_{eff}$ ) at the mid offset gathers on the far right side of the display. The far left side of the 2 parameter displays is the semblance for the  $V_c$  parameter and in the middle is the semblance for the  $\gamma_{eff}$  parameter.

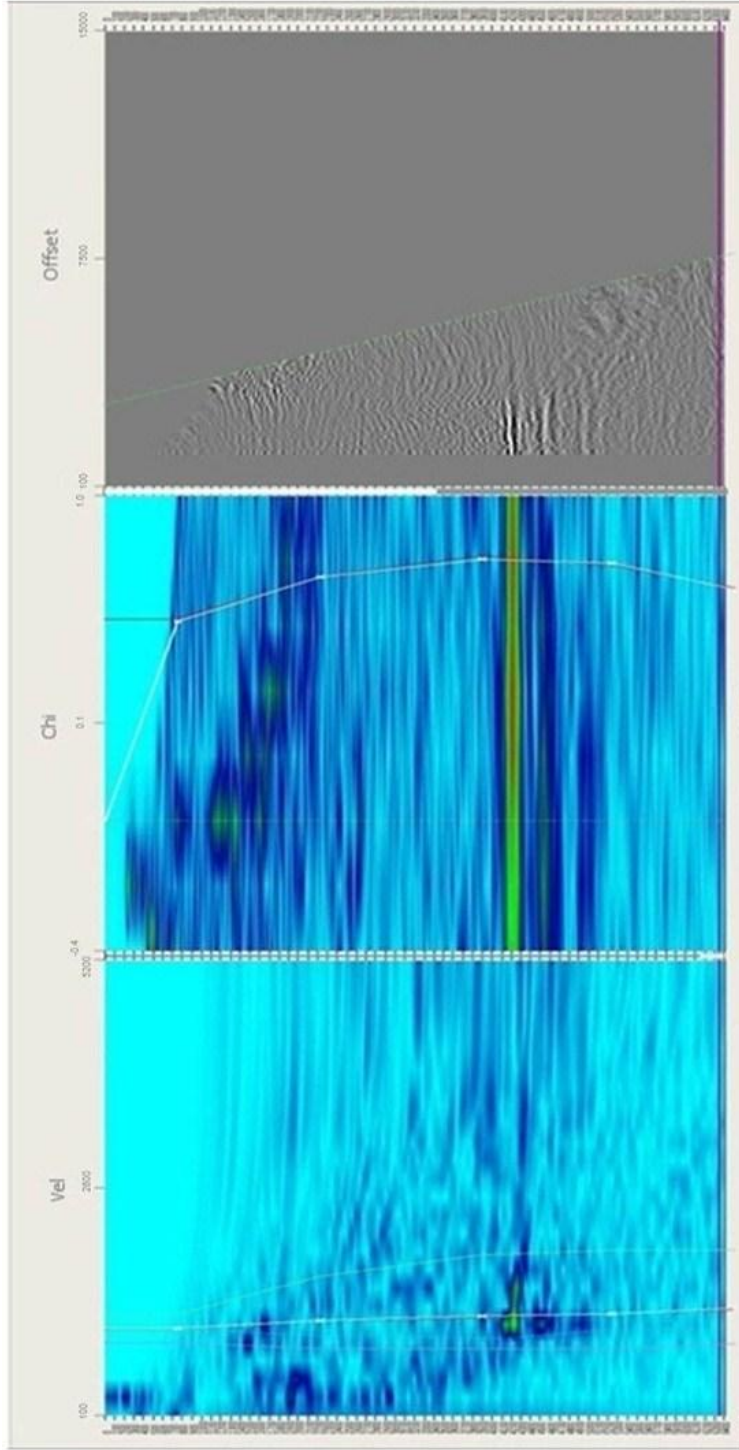


Figure 4.8: The far left side of the 2 parameter displays is the semblance for the  $V_c$  parameter and in the middle is the semblance for the  $\chi_{eff}$  parameter and the far right side is showing the effects of the parameter estimation of PS-wave normal moveout ( $\chi_{eff}$ ) at the far offset of the gather.

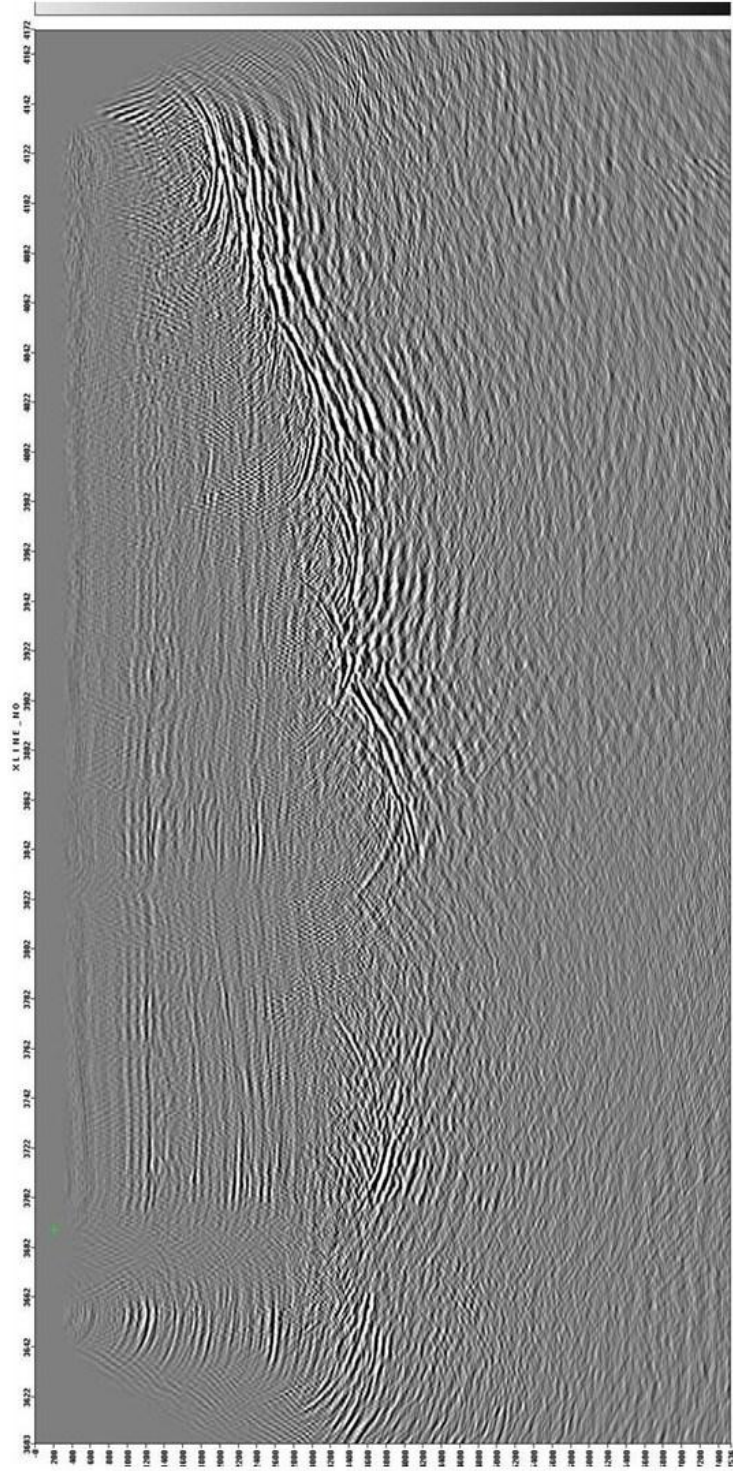


Figure 4.9: PS-wave stack generated after estimating  $V_c$  from the short spread gathers. The top of the salt body is fussy and not well illuminated as there is anisotropy in the layers.

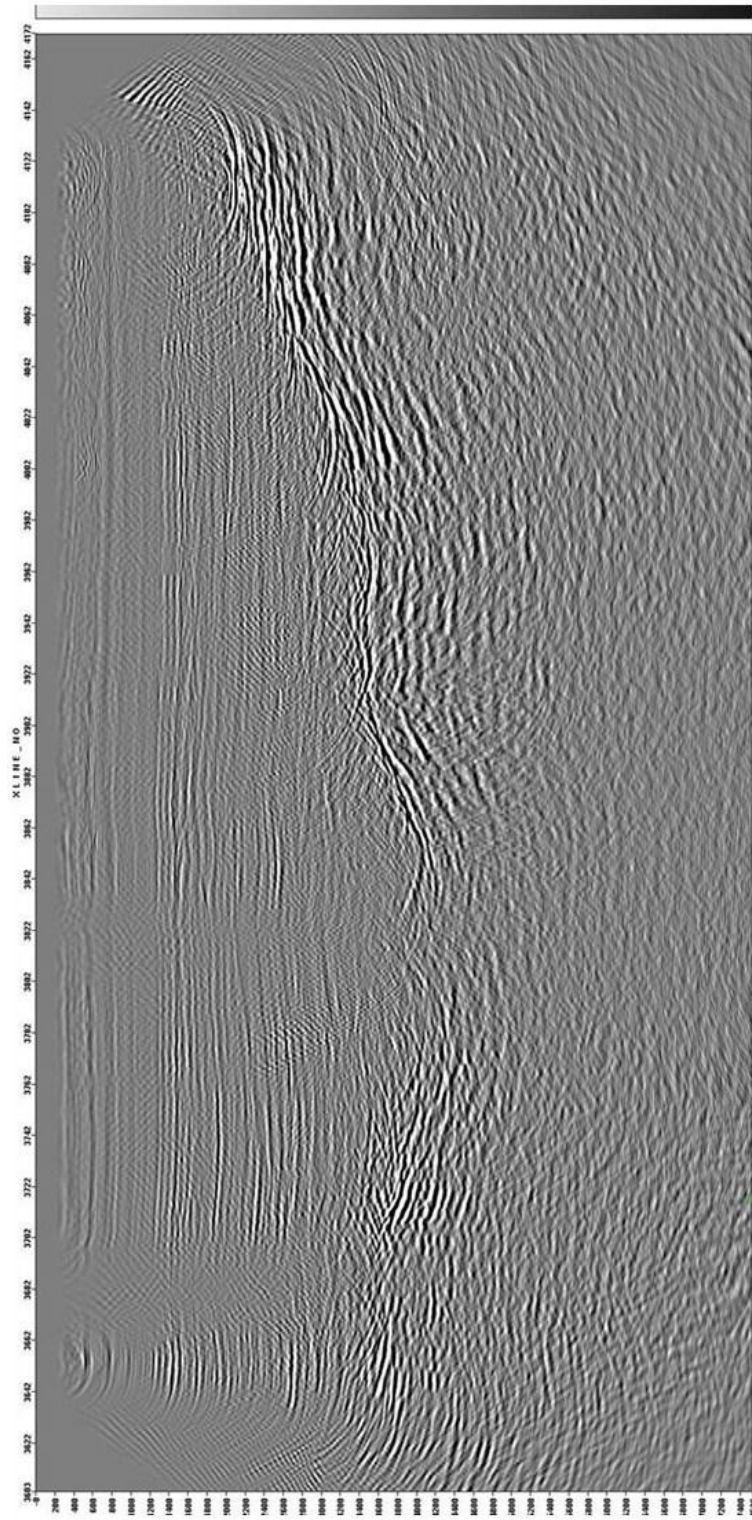


Figure 4.10: PS-wave stack after the estimation of  $V_c$ ,  $\gamma_0$  and  $\gamma_{eff}$  from the mid-offset gathers, applying the parameters and stacking.

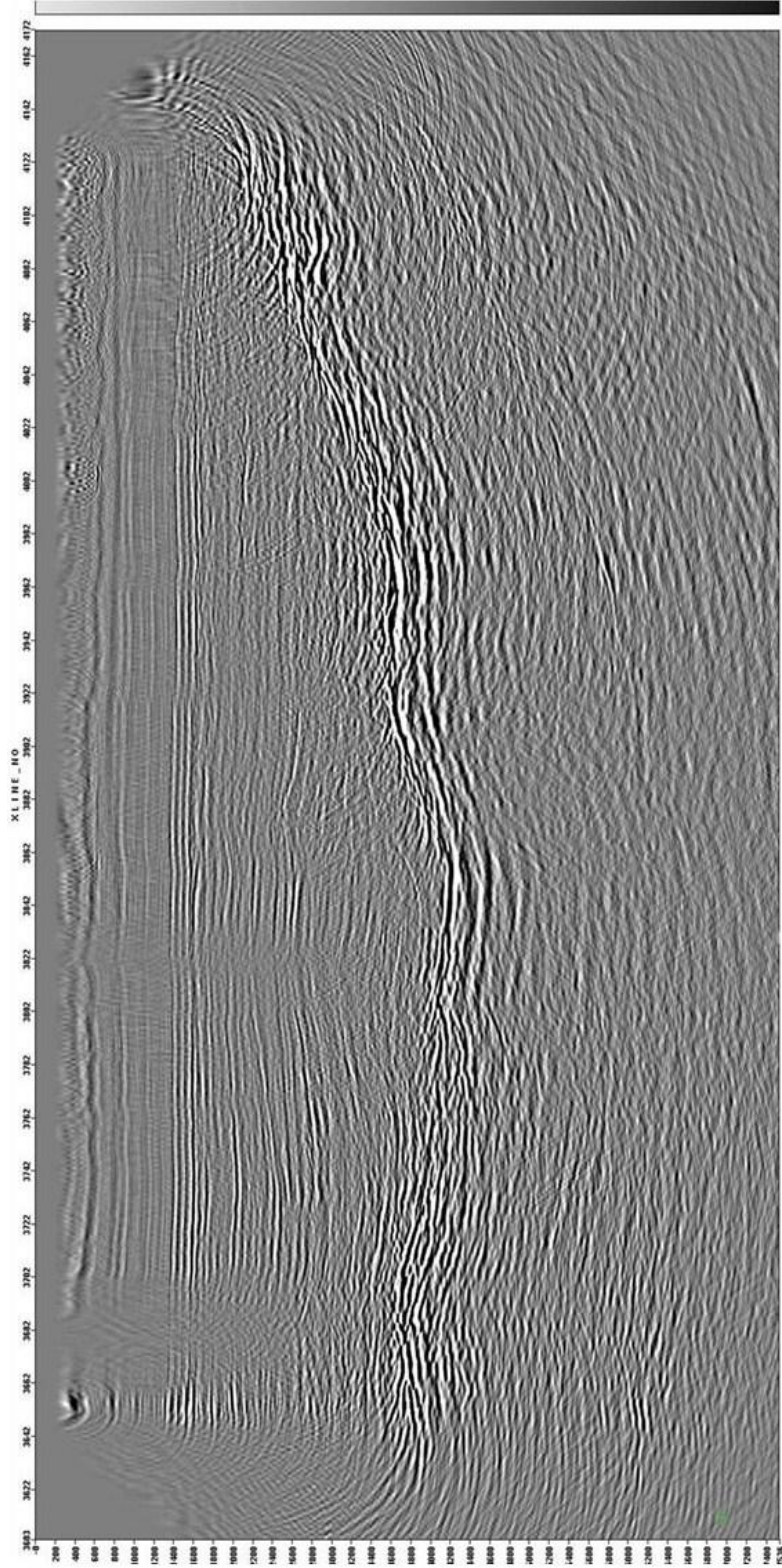
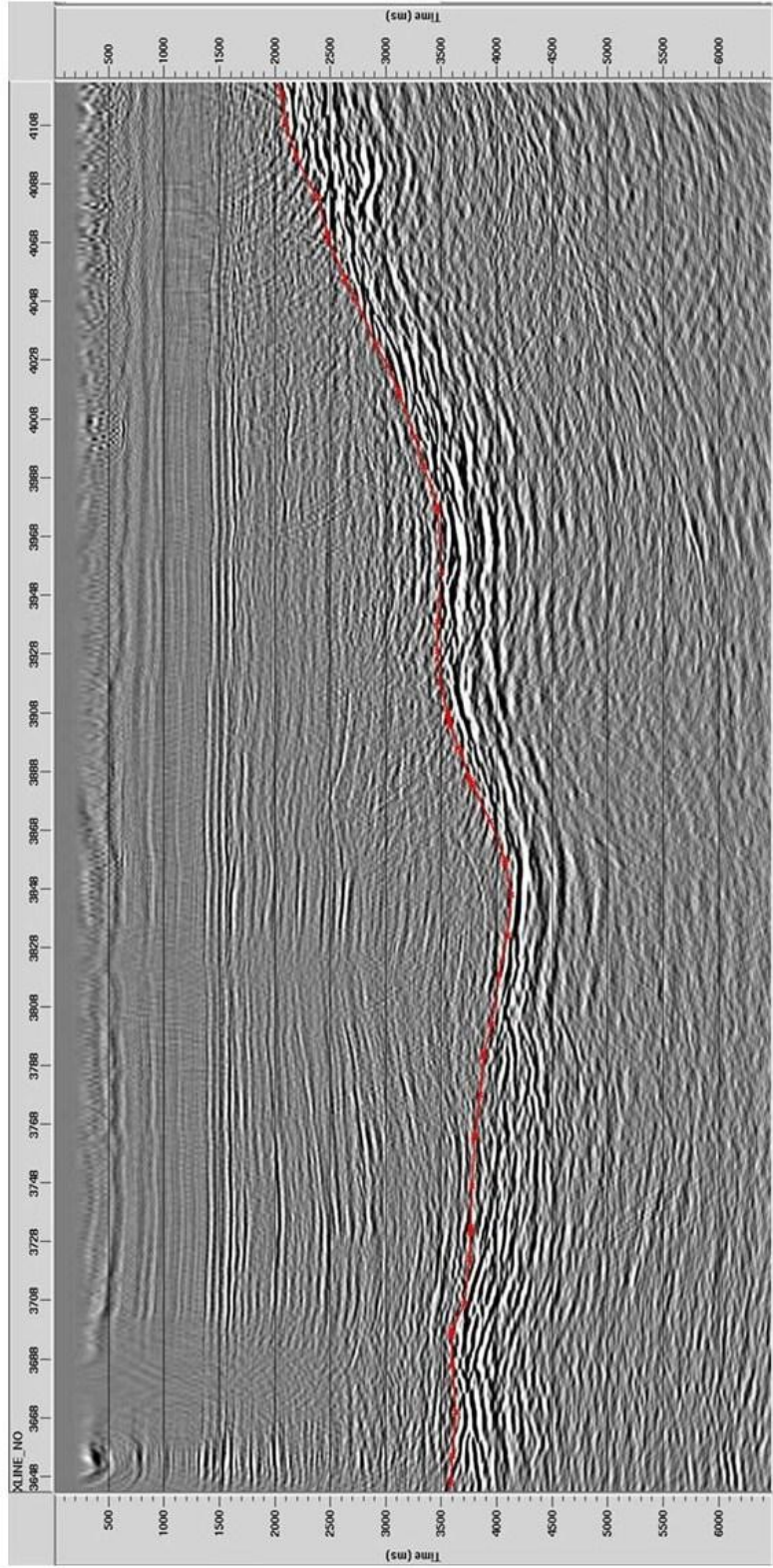


Figure 4.11: The PS-wave stack after estimating  $V_{c2}$ ,  $\gamma_0$ ,  $\gamma_{eff}$  and  $x_{eff}$  from the far offset and two iterations of PSTM residual velocity update. The top of the shallow salt is illuminated better with the anisotropic velocity applied to the data and stacked. The  $V_p/V_s$  from  $T_{ps}$  and  $T_p$  of the top of salt shown in stacks sections (PP and PS) is estimated to be 3.



(a)

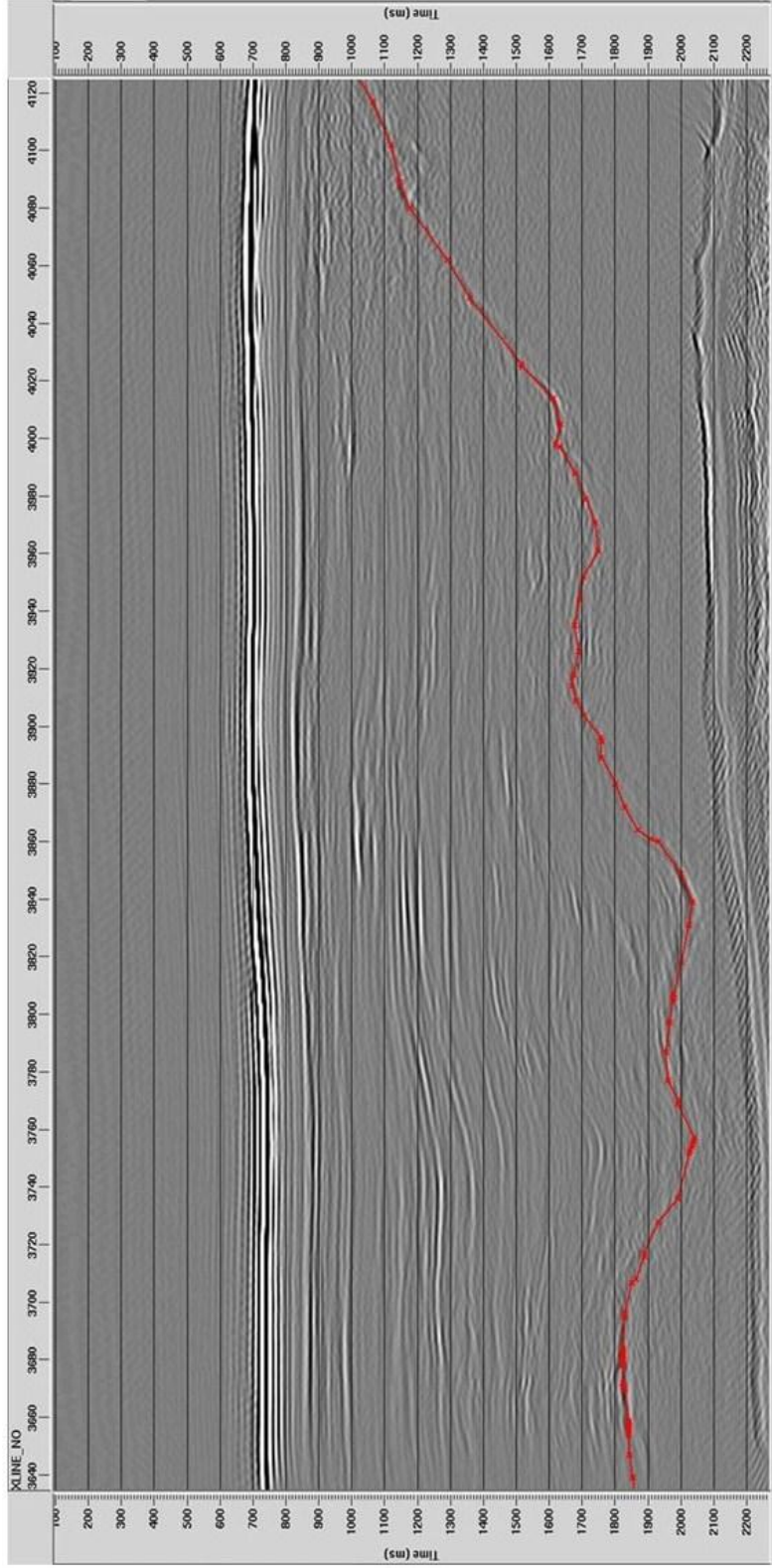


Figure 4.12: (a) PS-data stack section showing the top of salt (b) The PP-wave stack section with the equivalent top of salt shown. The  $V_p/V_s$  from  $T_{ps}$  and  $T_p$  of the top of salt shown in stacks sections (PP and PS) is estimated to be 3.

## Chapter 5: Discussion and Conclusion

### 5.1 Discussion

In PP- or PS-wave propagation through the earth, there could be a smooth or rapid velocity variation. In this study, using ocean bottom data from the Green Canyon area of the Gulf of Mexico, vertical transverse isotropy (VTI anisotropy) is assumed. Because the earth is an elastic material, how many of the elastic parameters could be accurately derived to properly account for the effects of anisotropy in the study area? What techniques would be appropriate to accurately and effectively estimate these parameters? Is it the ray-based technique or the anisotropic velocity model building technique? The parameters that were estimated in this data driven study were  $V_p$ ,  $V_s$ ,  $V_{c2}$ ,  $\gamma_0$ ,  $\gamma_{eff}$ ,  $\chi_{eff}$ ,  $\eta_{eff}$ , and  $\zeta_{eff}$ .

In anisotropic media, there could be slow and fast modes, but this study focuses on the vertical transversely isotropic (VTI) layers which means polarized PS in-line mode. In most cases, results from applying the equations for estimating the parameters for applying the PS-wave velocities in the presence of anisotropy are approximately applicable to data from azimuthal anisotropic media (Thomsen, 1999).

The various velocity ratios were estimated from PP-wave and PS-wave from corresponding events identified from interpretation. This might not be an issue when looking at major reflectors like the top of salt in my study area (Figure 3.4) but when addressed on a finer scale might be difficult. This is evident when horizons were picked above the top of salt in the study area (Figure 3.4) in the ray-based technique. For the

study area coarser event reflections are appropriate for the purpose of velocity model building. The processing and interpretation of PS-wave seismic data could effectively go on simultaneously. This has been demonstrated in this study in both the ray-based technique and the anisotropic velocity model building technique. Thomsen (1999) agrees that in the absence of borehole data,  $\gamma_0$  could be obtained from the PP and PS stack sections correlation. For this study, the PP and the PS stack sections were generated using the near offset data and in the anisotropic model building technique the asymptotic conversion point (ACP) binning was used for the PS-wave stack section. The assumption is that the hyperbolic move-out correction is sufficient for the near-offset data in both the PP and the PS stack sections (Tessmer and Behle 1988, Stewart et al., 2002).

The PP- and PS-wave stack sections in the ray-based technique were generated with the reduced water bottom reduced time from receiver gathers to account for the differences in source and receiver depths. And it's assumed that this removes the effect of the hyperbolic moveout when ray-tracing through the data to flatten the common receiver gathers using this technique (Backus et al., 2005). Another assumption is that the depth equivalent of PP and PS reflection events on stacked images can be identified and their reflection events can be identified on the gathers that produced the stacked sections. Although DeAngelo et al, (2008) points out that this might not always be true, stating the expectation is to be able to locate their casual reflection events on common-receiver gathers. The ray-based technique ignores the effects of anisotropy and the out plane effects.

Aki and Richards (1980) show that the normal-incidence conversion coefficient increases with increase in angle when using ACP binning to gather the data. This describes the smear shown to appear at the source-receiver far offset along the horizon (Figure 4.3). Despite the smear when using the ACP binning, the use of this approach is appropriate for the purpose of anisotropic  $V_s$  velocity model building in time domain (Thomsen 1999). The result depends on  $\gamma$  which in turn depends on anisotropy and the multiple layer effects. The ACP binning was used to gather the PS-wave gathers for generating the stack. Also, ACP binning is significant in the acquisition and planning of PS-wave seismic data (Thomsen 1999). In the areas of achieving full fold during acquisition and avoiding acquisition footprints. The demonstration using a 2D line carried earlier in this study was necessary to provide estimates of essential parameters for any future 3D survey planned for the study area.

Due to the acquisition design, there were not enough traces in the near offset ACP binned gathers and this became a challenge for PP and PS short spread velocity analysis needed for generating the stack. The velocity analysis for other parameter estimations led to first migrating (PSTM) the data. This was to position the traces correctly and achieve regularized offsets before estimating the parameters  $V_{c2}, \gamma_0$  and  $\gamma_{eff}$ . This is appropriate conventional practice since the migration process involves a positioning and time shifting process. The positioning process described above does not depend on velocity but the time shifting process to align the events on the gather is dependent on velocity. The latter is significant in the PSTM velocity update to estimate the parameters  $\chi_{eff}, \eta_{eff}$ , and  $\zeta_{eff}$

that align the gather in the presence of anisotropy. The estimated Vs from the 1.5D ray tracing compared to Vs estimated from Vc and surrounding well logs, using Vp with the mudrock line equation. Also, the estimated Vs values was compared to Vs estimated from Vp/Vs from correlating the PP and Ps stacks and show similar trends in Figure 5.1.

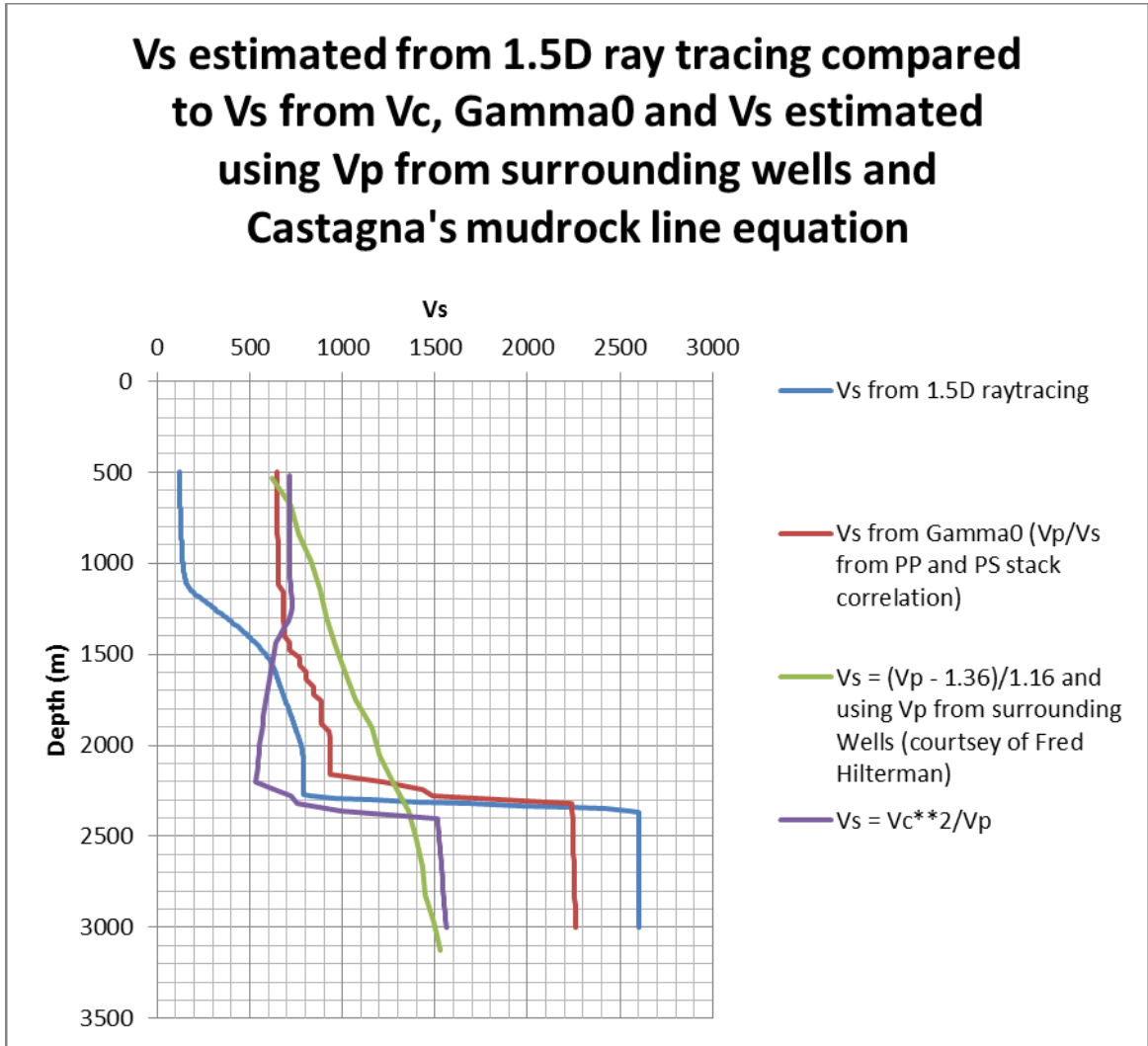


Figure 5.1: The graph shows the estimated Vs from surrounding well logs (courtesy of Fred Hilterman) using mudrock line equation (Castagna et al., 1985), compared to Vs estimated from the 1.5D ray tracing, gamma0 and Vc.

Cheret et al. (2000) and Dai and Li (2005) describe the possibility of using just one combined parameter to describe the non-hyperbolic moveout. This could be another option to pursue and discuss in future work. Another option for future work is to consider the fast and slow velocities with the aim of updating the azimuthal anisotropy. This could be achieved from analyzing azimuth sector stacks to identify the fast and slow velocities both in the radial and transverse directions. This process would require velocity update both in the radial and transverse directions to generate the best corrected gather and stack that corrects for the azimuthal or horizontal anisotropy. Meanwhile a lot of software and plugins were used in this study. Therefore, quality control plots were generated after every process in this study with the sole purpose of generating a final product that is high quality, and meets the targets and expectations of this study.

## **5.2 Conclusions**

- (1) This study has been able to use the geology, the  $V_p$ ,  $V_s$ , and rock material properties in the Green Canyon area of the gulf of Mexico to study the ability to build appropriate velocity model for the study area using a ray-tracing technique and consider the presence of anisotropy using anisotropy equations. The estimated velocities focus the data better and have been compared using the mudrock line (Castagna et al., 1985) and estimated velocities from surrounding wells in the Green Canyon area of the Gulf of Mexico.

- (2) The parameter estimation for building velocity model building for PS-wave is affected by anisotropy which is best tackled in the time domain before going into the depth domain or imaging. The significance of the calculating the vertical velocity ratios in the time domain are significant for the way PS-wave acquisition is planned in order to illuminate the target areas sufficiently. The processing and interpretation are carried out simultaneously for better result during parameter estimations and a better final seismic image. The  $V_p/V_s$  values estimated from the top of from the Stacked PP and PS-sections is 3.
- (3) Having used ocean bottom seismic data from the Gulf of Mexico, this process is data driven and was achieved by applying existing approximate formulas for a vertical transverse Isotropy (VTI) to generate the PS-wave image in Green Canyon area of the Gulf of Mexico and it clarifies that the anisotropic velocity analysis generates a better image than just the ray-tracing velocity model building technique in this study.
- (4) Careful quality control measures were taken to find the appropriate way of applying these formulas described in this study to estimate the PS-wave velocities in the presence of anisotropy and produce a better image that illuminates the top of the salt body better than previously possible in this study.

## References

Aki, K., and Richards, P., 1980, Quantitative Seismology: Theory and Methods: W. H.

Freeman & Co, 1st Edition: 557 p.

Alkhalifah T. and Tsvankin I. 1995. Velocity analysis for transversely isotropic media:

Geophysics 60, 1550-1566.

Amery, G.B. 1969. Structure of Sigsbee scarp, Gulf of Mexico. American Association of

Petroleum Geologists Bulletin 53(12):2480-2482.

Anderson, R.N. and Boulanger, A., 2009. Prospectivity of the Ultra-Deepwater Gulf of

Mexico, Lamont-Dougherty Earth Observatory, Columbia University. Palisades,

NY, USA. Available online: Last accessed on 1 August 2011,

<http://leanenergy.ldeo.columbia.edu/docs/UltraDeep%20Prosp%2010-22-02.pdf>.

Backus, M. M., P. E. Murray, B. A. Hardage, and R. J. Graebner, 2006, High-resolution

multicomponent seismic imaging of deepwater gas-hydrate systems: The Leading

Edge, 25, 578–598.

Barkved O., Bartman B., Compani B., Gaiser J., Von Dok R, Johns T, Kristiansen P.,

Probert T., and Thompson M., Summer 2004. The many facets of

multicomponent seismic data: Oilfield Review 16, no.2, 42.56.

- Bird, D. E., K. Burke, S. A. Hall, and J. F. Casey, 2005, Gulf of Mexico tectonic history: Hotspot tracks, crustal boundaries, and early salt distribution: AAPG Bulletin, 89, 311–328.
- Caldwell, J., 1999, Marine multicomponent seismology: The Leading Edge, Nov., 1274–1282.
- Castagna, J. P., Batzle, M. L., and Eastwood, R. L., 1985, Relationships between compressional-wave and shear-wave velocities in elastic silicate rocks: Geophysics, 50, 571-581.
- Chapman, C. H. (2004), Fundamentals of Seismic Wave Propagation: Cambridge University Press, Cambridge, 608 p.
- Cheret T., Bale R. and Leaney S. 2000. Parameterization of polar anisotropic moveout for converted waves. 70th SEG Meeting, Calgary, Canada, Expanded Abstracts, 1181-1184.
- Chernikoff, A. García, J., Stewart, R., and Xu, R., 2007, Interpretation of multicomponent Sihil 3D-4C seismic survey: What have we learned?: Presented at El Segundo Congreso y Exposición Internacional del Petróleo en México, efectuado del 28 al 30 de Junio del 2007 en Veracruz, Ver. , México.

- Chowdhury, A.H., and M.J. Turco, 2006. Geology of the Gulf Coast Aquifer, Texas.  
<http://www.twdb.state.tx.us/publications/reports/GroundWaterReports/GWReports/R365/ch02-Geology.pdf>. (accessed 10 May. 2011).
- Cleveland C., (Lead Author); Saundry P., (Topic Editor) "Mintrop, Ludger". In: Encyclopedia of Earth. Eds. Cutler J. Cleveland (Washington, D.C.: Environmental Information Coalition, National Council for Science and the Environment). [First published in the Encyclopedia of Earth August 18, 2006; Last revised Date August 18, 2006; Retrieved February 14, 2011 <[http://www.eoearth.org/article/Mintrop,\\_Ludger](http://www.eoearth.org/article/Mintrop,_Ludger)>
- Dai H. and Li X.-Y. 2001. Anisotropic migration and model building for 4-C seismic data: A case study from Alba. 71st SEG Meeting, San Antonio, USA, Expanded Abstracts, 795-798.
- Dai H. 2003. Integrative analysis of anisotropy parameter and velocities for PS converted waves. 73rd SEG meeting, Dallas, USA, Expanded Abstracts, 1577-1580.
- Davies, R.J., Cartwright, J.A., Stewart, S.A., Lappin, M. & Underhill., J.R. (eds) 2004. 3D Seismic Technology: Application to the Exploration of Sedimentary Basins. Geological Society, London, Memoirs, 29, 1-9.

- DeAngelo, M.V., P. E. Murray, B. A. Hardage, and R. L. Remington, 2008, Integrated 2D 4-C OBC velocity analysis of near-seafloor sediments, Green Canyon, Gulf of Mexico: *Geophysics* 73, Issue 6, B109-B115
- Dellinger J., Clarke R., and Gutowski P., 2001, Horizontal vector infidelity correction by general linear transform: *SEG*, 865-868.
- Diegel, F. A., J. F. Karlo, D. C. Schuster, R. C. Shoup, and P. R. Tauvers, 1995, Cenozoic structural evolution and tectono-stratigraphic framework of the northern Gulf Coast continental margin, in M. P. A. Jackson, D. G. Roberts, and S. Snelson, eds., *Salt tectonics: A global perspective: AAPG Memoir 65*, 109–151.
- Duey R., July 1, 2004. The future is now. Article for Exploration Edition: *Hart's E&P*; 77, 36- 39.
- Dziewonski, A.M. and Anderson, D.L., 1981. Preliminary reference Earth model. *Phys. Earth Planet. Inter.*, 25: 297-356.
- Elboth, T., H. Qaisrani, and T. Hertweck, 2008, De-noising seismic data in the time-frequency domain: *SEG Technical Program Expanded Abstracts*, 27.
- Feng, J., R. T. Buffler, and M. A. Kominz, 1994, Laramide orogenic influence on late Mesozoic–Cenozoic subsidence history, western deep Gulf of Mexico basin: *Geology*, 22, 359–362.

- Ferguson, R. J., and Stewart, R. R., 1998, Sand/shale differentiation using shear-wave velocity from P-S seismic data: *Journal of Seismic Exploration, Geophysical Press*, 7, 117-127.
- Hall, S.H., 2002. The role of autochthonous salt inflation and deflation in the northern Gulf of Mexico: *Marine and Petroleum Geology*, 19, 649-682.
- Harrison M.P. 1992. Processing of P-SV surface seismic data: anisotropy analysis, dip moveout and migration. Ph.D. thesis, The University of Calgary.
- Hudson J. A., 1992. Rock Characterization: ISRM Symposium, Eurock '92, Chester, UK, 14-17.
- Ivanhoe, L.F.,1997. Get Ready For Another Oil Shock!: can be accessed on <http://dieoff.org/page90.htm>. Last accessed 12/29/2010.
- Jackson, J.A., 1997. Glossary of Geology, 4th Edition, American Geological Institute, Alexandria, VA, 769 p.
- Lavergne M., 1989. *Seismic Methods*, London: Graham & Trotman, 192 p.
- Li, X.-Y. and Yuan, J., 2003. Converted-wave moveout and conversion-point equations in layered VTI media: Theory and application: *Journal of Applied Geophysics*, 54, 297-318.

- Liner, C. L. and Underwood, W. D., 1999, 3-D seismic survey design for linear  $v(z)$  media, *Geophysics*, 64, 486-493.
- Longhurst RS, 1973. *Geometrical and Physical Optics*, 3rd Edition, Longman, London, 369.
- MacLeod, M.K., Hanson, R.A., Bell, C.R., and McHugo, S., 1999, The Alba Field ocean bottom cable seismic survey: Impact on development; paper SPE56977 presented at the 1999 Offshore Europe Conference, Aberdeen, Scotland, 7-9.
- Madof, A.S., Christie-Blick, N., and Anders, M.H., 2009, Stratigraphic controls on a salt-withdrawal intraslope minibasin, north-central Green Canyon, Gulf of Mexico: Implications for misinterpreting sea level change: *AAPG Bulletin*, 93, 535-561.
- Nibbelink, K. and Martinez, J., 1998, 3-D seismic coherence, amplitude and bathymetry data definition of Pleistocene to recent sediments along the Sigsbee Escarpment, southeast Green Canyon, Gulf of Mexico, USA: *Gulf Coast Association of Geological Societies, Transactions*, 48, 289-299.
- Orange, D.L., Angell, M.M., Brand, J.R., Thomson, J, Williams, M., and Hart, W., and Berger, W.J., III, 2004. Geologic and shallow salt tectonic setting of the Mad Dog and Atlantis fields: relationship between salt, faults, and seafloor morphology: *The Leading Edge*, April, 354-365.

- Podolak, M.W., 2003, Koscian – Bronsko reef in the light of Cwaves, presented at the 65th EAGE Conference & Exhibition, Stavanger. Last accessed 18 July 2011 <[http://www.iongeo.com/content/released/VectorSeis\\_imaging\\_Bronsko\\_Koscian\\_reefs.pdf](http://www.iongeo.com/content/released/VectorSeis_imaging_Bronsko_Koscian_reefs.pdf)>
- Sah, S. L. 2008, Encyclopaedia of Petroleum Science and Engineering, Volume 1, Kalpaz publications, 321 p.
- Salvador, A., 1987, Late Triassic–Jurassic paleogeography and origin of Gulf of Mexico Basin: AAPG Bulletin, 71, 419–451.
- Salvador, A., ed., 1991, The Gulf of Mexico Basin: Boulder, Colorado, Geological Society of America, The Geology of North America, J, 568 p.
- Sassen, R., S. Losh, L. Cathles, H. Roberts, J. K. Whelan, A. V. Milkov, S. T. Sweet, and D. A. DeFreitas, 2001a, Massive vein-filling gas hydrate: relation to ongoing gas migration from the deep subsurface Gulf of Mexico: Marine and Petroleum Geology, 18, 551-560.
- Sassen, R., H.H. Roberts, A.V. Milkov, and D.A. DeFreitas, 2001b, Sea floor vents, seeps, gas hydrate: Relation to flux rate from the deep Gulf of Mexico petroleum system: GCSSEPM Foundation 21st Annual Research Conference, Petroleum Systems of Deep-Water Basins: Global and Gulf of Mexico Experience, p. 489-506.

- Sassen, R., J. S. Watkins, C. Decker, T. S. Sweet, A. D. DeFreitas, and S. Losh, 2001c, High maturity gas in the Main Pass area: comparison to the central Gulf of Mexico slope: Transactions of the Gulf Coast Association of Geological Societies, 51, 285-291.
- Shannon, C. E., 1949, Communication in the presence of noise, in Proc. IRE, 37, 10–21.
- Stewart R.R., Gaiser J.E., Brown R.,J. and Lawton D.C. 2002. Converted-wave seismic exploration: Methods: Geophysics 67, 1345-1363.
- Stewart, R.R., Gaiser, J., Brown, R.J., and Lawton, D.C. 2003. Converted-wave seismic exploration: Applications : Geophysics, 68, 40-57.
- Stewart, R.R., 2008. Methods of Multicomponent Seismic Data Interpretation. 70th EAGE Conference & Exhibition. Last accessed 18 July 2011  
<[http://www.crewes.org/ForOurSponsors/ConferenceAbstracts/2008/EAGE/Stewart\\_EAGE\\_2008.pdf](http://www.crewes.org/ForOurSponsors/ConferenceAbstracts/2008/EAGE/Stewart_EAGE_2008.pdf).>
- Sweirz, A.M., 1992. Seismic stratigraphy and salt tectonics along the Sigsbee Escarpment, southeastern Green Canyon region, CRC Handbook of Geophysical Exploration at Sea, 2nd Edition, R.A. Geyer, ed, CRC Press, Inc., Boca Raton, pp. 227-294.
- Tessmer G. and Behle A. 1988. Common-conversion point stacking technique for converted waves: Geophysical Prospecting 36, 671-688.
- Thomsen L. 1986. Weak elastic anisotropy: Geophysics 51, 1954-1966.

- Thomsen L. 1999. Converted-wave reflection seismology over inhomogeneous, anisotropic media: *Geophysics* 64, 678-690.
- Tree, E., 1999, The vector infidelity of the ocean-bottom multicomponent seismic acquisition system: EAGE expanded abstracts, 6-19.
- Tsvankin, I., and Thomsen, L., 1994, Nonhyperbolic reflection moveout in anisotropic media: *Geophysics*, 59, 1290–1304.
- Tsvankin I. and Grechka V. 2000. Dip moveout of converted waves and parameter estimation in transversely isotropic media: *Geophysical Prospecting* 48, 257-292.
- White, TE, 1999, Tunnel blasting - recent developments: IMM, Doncaster, England, 2, 17 p.
- Zhang Y. 1996. Non-hyperbolic converted wave velocity analysis and normal moveout. 66th SEG Meeting, Denver, USA, Expanded Abstracts, 1555-1558.

## Appendix A

Table 1: Thomsen (1986) parameters of the five-layer model for evaluating the accuracy of equation 4.15.

| Depth (m) | $V_{p0}$ (m/s) | $V_{s0}$ (m/s) | $\epsilon$ | $\delta$ |
|-----------|----------------|----------------|------------|----------|
| 400       | 1875           | 826            | 0.225      | 0.100    |
| 800       | 2202           | 969            | 0.150      | 0.006    |
| 1200      | 2500           | 1215           | 0.100      | -0.035   |
| 1600      | 3306           | 1819           | 0.134      | 0.000    |
| 2000      | 3368           | 1829           | 0.110      | -0.035   |

Table 2: The  $V_s$  estimated values from Gamma0, PP stacking velocity, PS stacking velocity, and ray tracing.

| Time | Gamma0 | PP Stacking Vel | $V_s = \text{Gamma0} / \text{PP stacking vel}$ | PS stacking Vel | $V_s(\text{Ray tracing})$ | $V_p(\text{Ray tracing})$ | $V_s = V_c^{**2} / V_p$ |
|------|--------|-----------------|--|-----------------|---------------------------|---------------------------|-------------------------|
| 100  | 2.9    | 1882.1          | 649  | 1036.9          | 122.16                    | 1504                      | 714                     |
| 1100 | 2.9    | 1903.4          | 656  | 1041.3          | 163.08                    | 1504                      | 720                     |
| 1200 | 2.8    | 1908.5          | 681  | 1045.3          | 245.22                    | 1504                      | 726                     |
| 1300 | 2.8    | 1916.2          | 684  | 1051.4          | 398.65                    | 1557.94                   | 709                     |
| 1400 | 2.8    | 1921.2          | 686  | 1055.4          | 490.73                    | 1691.75                   | 658                     |
| 1500 | 2.5    | 1928.7          | 771  | 1061.4          | 599.22                    | 1802.44                   | 625                     |
| 1600 | 2.4    | 1933.7          | 805  | 1065.5          | 637.78                    | 1861.77                   | 609                     |
| 1700 | 2.3    | 1941            | 843  | 1071.5          | 679.67                    | 1945.21                   | 590                     |
| 1800 | 2.2    | 1945.9          | 884  | 1075.5          | 709.37                    | 1997.1                    | 579                     |
| 1900 | 2.1    | 1953.1          | 930  | 1081.6          | 752.67                    | 2072.47                   | 564                     |
| 2000 | 2.1    | 1964.9          | 935  | 1085.6          | 777.28                    | 2124.01                   | 554                     |
| 2100 | 2.1    | 2569.6          | 1223   | 1091.7          | 792                       | 2201.53                   | 541                     |
| 2200 | 2      | 2871.9          | 1435   | 1095.7          | 791.57                    | 2249.33                   | 533                     |
| 2300 | 2      | 4476.5          | 2238   | 1603.6          | 1694.31                   | 3408.04                   | 754                     |
| 2400 | 2      | 4485.9          | 2242   | 2609.2          | 2600                      | 4500                      | 1512                    |
| 2500 | 2      | 4493.1          | 2246   | 2617.7          | 2600                      | 4500                      | 1522                    |
| 2600 | 2      | 4497.9          | 2248   | 2623.3          | 2600                      | 4500                      | 1529                    |
| 2700 | 2      | 4505.2          | 2252   | 2631.7          | 2600                      | 4500                      | 1539                    |
| 2800 | 2      | 4510            | 2255   | 2637.3          | 2600                      | 4500                      | 1545                    |
| 2900 | 2      | 4517.4          | 2258   | 2645.8          | 2600                      | 4500                      | 1555                    |
| 3000 | 2      | 4522.2          | 2261   | 2651.4          | 2600                      | 4500                      | 1562                    |

# Appendix B

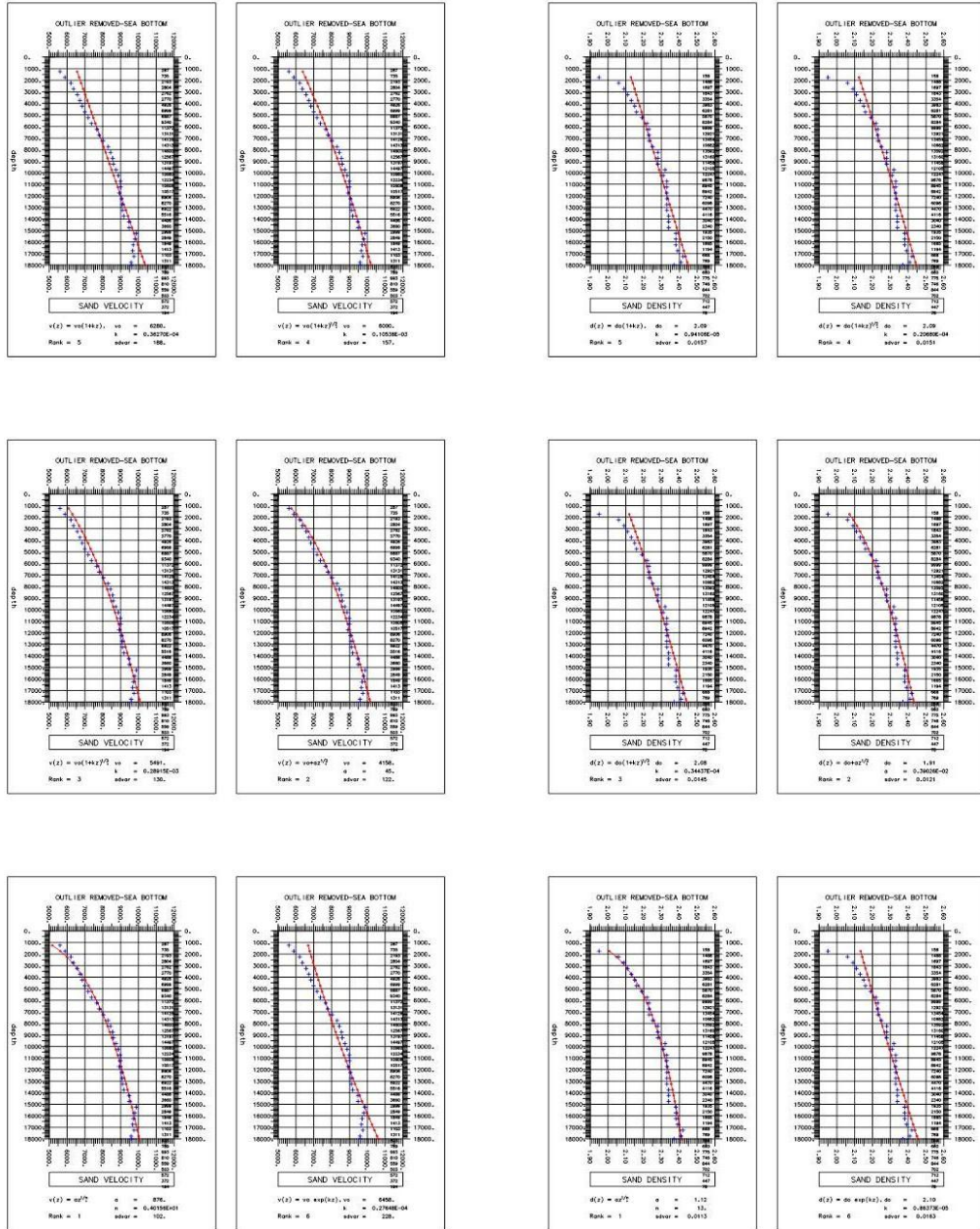


Figure B1: The calculated Vp for the Green Canyon area from nearby well logs (courtesy of Fred Hilterman).

## Appendix C

### Fundamentals of PP and PS wave

From the basics of reflection seismology, for a seismic trace to be recorded in any seismic survey, a source and receiver is required. The source generates the energy sent into the earth as required by the survey design and the receiver captures the details required from the subsurface of the earth. The recorded seismic trace is considered to be a result of source wavelet convolved with reflectivity of the earth as shown in Figure C1. Reflectivity of the earth depends on the materials in the layers of the earth and is the portion of the source energy that is reflected when horizons separating the layers of the earth are encountered when shooting a seismic survey. This reflected energy is recorded by the receiver (a pressure phone or a geophone recording device).

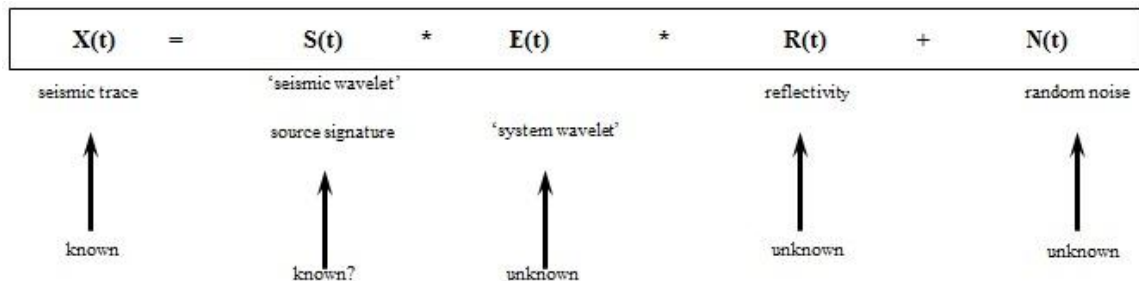


Figure C1: Seismic trace is a product of convolving reflectivity of the earth with the seismic signature, the source wavelet, and noise.

$$\text{Reflectivity} = \Delta I / 2I, \quad \text{where } I = \rho V$$

where “I” is the acoustic impedance, “ $\rho$ ” is the density of the rock material, and “V” is the velocity. Any medium that is capable of wave propagation is described as having

impedance and impedance is a function of velocity and density of the various horizons; therefore there would be reflection at any horizon with Impedance change. In an isotropic and homogenous medium the energy propagation is uniform, amplitudes change when there is impedance change at a horizon and some energy reflected while the rest is transmitted. The ratio of the reflected and transmitted amplitude to the initial amplitude is the reflection coefficient and transmission coefficient respectively (Lavergne, 1989).